UNIVERSITY OF ZULULAND

Aqueous Synthesis and Characterization of Hematite Nanorod-based Arrays for Water Splitting and Gas Sensing Applications

A Dissertation presented to the Department of Physics and Engineering of the Faculty of Science and Agriculture

By

C. L. Ndlangamandla

In Fulfillment of the Requirements for the Degree of Doctor of Philosophy in Physics at the University of Zululand

Supervisor: Prof. M. Maaza

Co-Supervisors: Prof. M. O. Ndwandwe

2013

DECLARATION

I, the undersigned, hereby declare that the work contained in this thesis is my own original work and that I have not previously in its entirety or in part submitted it at any university for a degree.

Signature: é

Date: é

ABSTRACT

Hematite, α-Fe_2O_3, is one of the most stable oxides, with a band gap that ranges between 1.9 and 2.2 eV, and hence a prominent candidate for water splitting applications in sea water conditions. For such an application, the α-Fe_2O_3 particles should exhibit several singular characteristics: (i) their size should be within the nano-scale regime, (ii) their shape has to present a significant anisotropy during their growth and can be easily oriented, (iii) should be doped effortlessly. Consequentially, spatially oriented and doped α-Fe_2O_3 nanorods would allow an effective light trapping/harvesting combined to an efficient and a longer mean free path of the photo-induced charge carriers and hence a faster charge diffusion with a minimized excitonic recombination. The so called Vayssieres' methodology i.e. the aqueous chemical growth (ACG) process has been used in this research work as it is the ideal path to design and engineer the desired Ruthenium doped and spatially oriented α-Fe_2O_3 nano-rods. The thesis reports on a comprehensive set of synthesis and characterizations in view of optimizing the water splitting properties of such Ru doped and undoped α-Fe_2O_3 photoanodes. In addition, gas sensing potentialities of these Ru doped and undoped α-Fe_2O_3 have been investigated.

Keywords: *Hematite, ACG, Nanorods, Growth mechanism, water splitting, optical and structural properties, effect of pH, Doping, Hydrogen sensing.*

Acknowledgements

There are numerous people I would like to thank for getting me to this point; not only to the end of my PhD thesis, but to where I am in life today. Hopefully I can express my gratitude to you all in person.

I am very grateful to my supervisors, Prof. M. Maaza and Prof. M. O. Ndwandwe for their unconditional support and guidance, daily advice, mentoring, motivation and support throughout the entire study.

Very special thanks goes to Dr. B. D. Ngom and Prof. O. Nemraoui for providing daily advice, mentorship and motivation, and for sharing their passion for science and giving guidance during my thesis writing also for proof reading my thesis.

Very special thanks go to Dr. Lionel Vayssieres for sharing his passion for science and giving guidance and for his ideas and scientific suggestion and motivation on this work.

I would like to express my gratitude to Professor K. Bharuth-Ram for sharing his passion for science and giving guidance and for taking his valuable time to do the Mössbauer measurements and helping me in doing the analysis in his laboratory.

I would like to express my gratitude to all scientist helped me in acquiring the results for my thesis. To name few: Dr. Remy Bucker and Mr. Z. M. Khumalo for X-Ray Diffraction measurements and The University of Cape Town electron microscope unit Technicians for Scanning Electron Microscope measurements.

Very special thanks to all my friends (Mr. T. P Jili, Dr. S.S. Ntshangase, Dr. C. B. Mtshali and Mr. A. P. Sefage) for motivating and supporting me throughout this life adventure.

Very special thanks to my Wife (Zanele), Sons (Lethukuthula Khayelihle and Thobelani Khethelo) and Cabangile (Nokwanda), I would like to thank you all for your unconditional love,

support, motivation, patience, perseverance, and understanding and for the comfort you always provide whenever needed all these years.

Special thanks to Mum (Mhlengasekho), Dad (Mdinwa) Ndlangamandla, Brothers especially (Bangani) and Sisters, and all of my wonderful family; most of whom have no idea of what I do all day, but are still my most ardent supporters.

I would like to thank all the iThemba LABS Staff and Students especially the Material Research Department (MRD) Staff and Students for their support and motivation and also for their contribution and life lesions they able to teach me while doing my research with them.

I am very grateful to the Accelerator department staff of iThemba LABS, especially (Dr. R Thomae) for his support and motivation and understanding and for allowing me to spend time at MRD to finalize this work.

I would like to thank South African Nuclear Human Asset Resource Program (SANHARP)– National Research Foundation (NRF) and the University of Zululand Research Foundation for the financial support.

This work is dedicated to Wife (Zanele) and Kids.

TABLE OF CONTENTS

LIST OF FIGURES

CHAPTER I

1. INTRODUCTION AND MOTIVATION

1.1. Introduction

The current global economy is highly dependent on the non-renewable energy sources, which are fossil fuels. They are playing the integral part to industry, agriculture, and transport in our everyday life. The access to high energy fossil fuel sources such as coal, oil and gas facilitated the industrial revolution and the economic growth of developed nations worldwide. Unfortunately, the extensive utilization of fossil fuels has had an unfavorable effect on the environmental well-being. During the fossil fuel extraction and combustion the high amount of gases like, for example carbon dioxide, carbon monoxide and methane, are released. These are greenhouse gases that contribute enormously to global warming and climate change.

Other environmental problems that arise due to the usage of fossil fuels are air and water pollution, which are compromising the health and the well-being of the society. Reliance on fossil fuels can also have negative political and social consequences as a result of the economic dependence of the world on oil-producing countries; therefore this jeopardizes the well-being of the developing countries.

More especially South Africaôs reliance on coal and oil can no longer be justified due to the increasing fuel price and long term shortage of those fossil fuels. It is South Africaôs interest to keep pace with the international emerging technology in the field of alternative fuel production.

Therefore increasing pollution in urban areas has made the search for the cleaner and environmental friendly fuel necessary. Recently, South Africa participated on the 2012 COP17 held in Durban KwaZulu Natal Province, which was planned to discuss ways of coming up with strategies to address climate change and global warming crisis. The challenge is to maintain and improve the standard of living of the world's population and support economic growth while utilizing energy sources that are renewable and environmental friendly.

1.2. Hydrogen as the future energy carrier

The move towards a hydrogen economy is being driven by its potential economic and environmental benefits. Many technical, political and economic challenges need to be overcome before a hydrogen economy can be realized. Some technical problems include producing hydrogen efficiently using renewable energy sources, storage of hydrogen (particularly for automotive uses), development of efficient, economically viable fuel cells, and the development of suitable infrastructure.

Hydrogen (H_2) releases energy when combine with oxygen; yet in practice, hydrogen production from water requires more energy than released when used as fuel. Free hydrogen does not occur in large amounts on earth; therefore water splitting is a well-known and economic alternative than other hydrogen production methods such as electrolysis. A reduction of carbon dioxide emission can be achieved only if the energy used to make hydrogen is obtained from carbon free-based sources. Hydrogen economy could greatly reduce the emission of greenhouse gases and emissions associated in climate change [1]. Hydrogen is an environmentally friendly energy source [2], mostly in transport applications, without release of pollutants [3].

Hydrogen has an energy density that is three times greater than that of an average hydrocarbon fuel. Approximately 90% of hydrogen as indicated in the Figure 1.1 below is produced by natural gas reforming, partial oxidation of light alcohols, and autothermal reforming [4]. In addition, a number of alternative technologies exist in which hydrogen can be generated from starting materials such as coal; biomass; and water, including electrolysis, fossil fuel processing, and coal gasification. However, most of these technologies produce a hydrogen product which is of a poor purity. Purification is achievable bearing in mind that the equipment costs are extremely high and the process is therefore mostly economically unachievable.

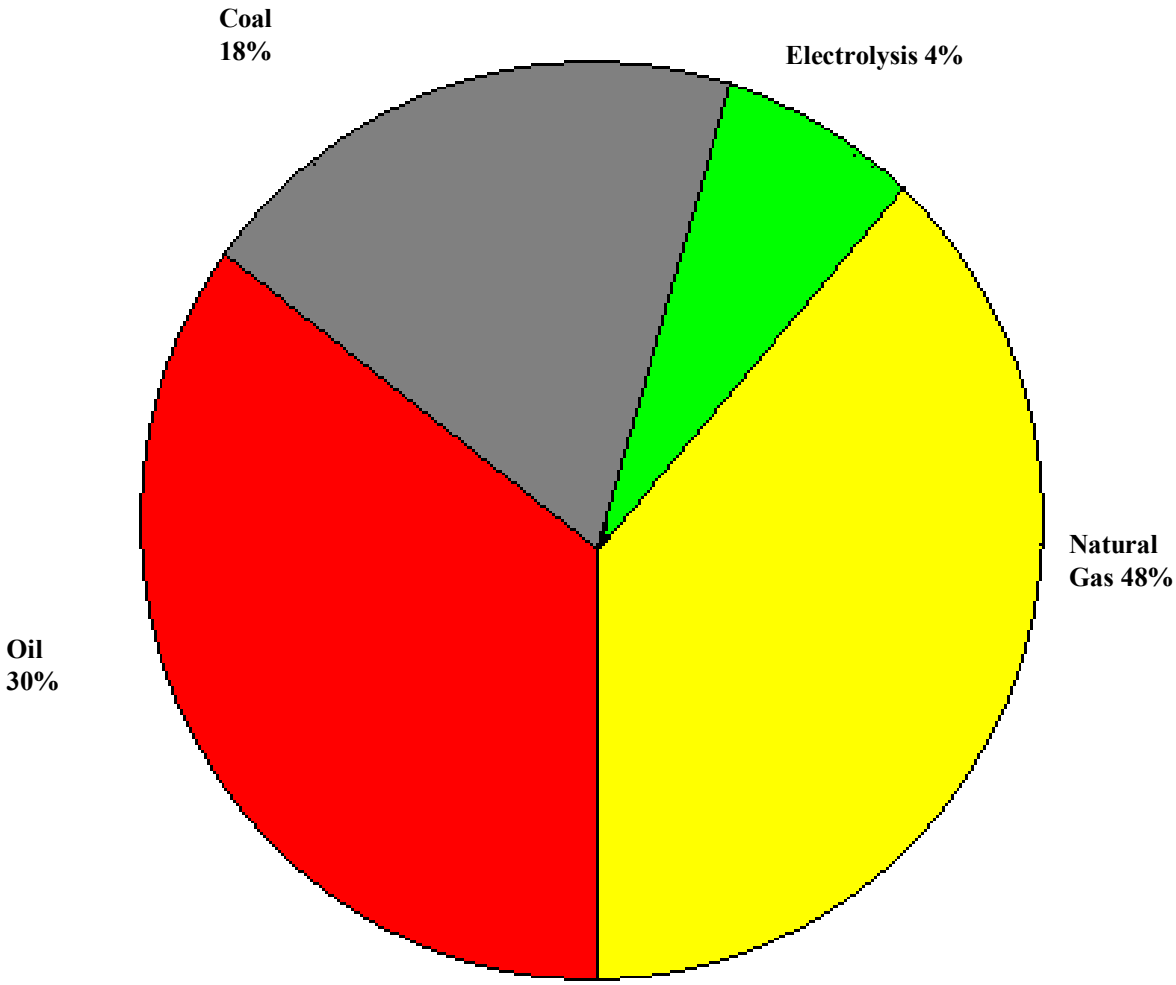

Figure 1.1 The statistical distribution diagram of different sources of current worldwide hydrogen production [3].

1.3. Semiconductors based water splitting

Semiconductors are characterized by a band gap, which is in the order of 1 ï 3.5 eV. Semiconductor materials to be used as a photoelectrode for water splitting under the solar illumination (when the hole-electron pair is created) require the semiconductorôs conduction band edge to be located just above the reduction potential of water for the electron transfer to participate in the production of hydrogen and itôs valence band should also be lower than the oxidation potential of water to create holes to participate in the oxidation of water (for oxygen evolution) as shown in Figure 1.2.

In many semiconductors, the spontaneous water splitting is impossible because of the electron transfer barrier that exist due to the fact that the semiconductorôs conduction band edge is located below the reduction potential of water therefore the external potential bias is applied to promote this phenomenon. The absorption of the solar spectrum by the semiconductor is determined by its band gap. Therefore the photons with energy greater or equal to the semiconductors band gap are able to excite and create the hole-electron pair. Therefore the Fermi energy level of the semiconductor is referred to as the energy level at which the probability of occupation by the electron is one-half, which is equal to the electrochemical potential of electron in the semiconductor [5].

There are two types of semiconductors i.e. intrinsic and extrinsic semiconductor. The intrinsic semiconductor is referred to a pure semiconductor (without any additives or impurity or dopant). In this semiconductor the electrons and the holes are equal in numbers or at equilibrium. Extrinsic semiconductor referred to the doped semiconductor, where a dopant can either be an electron donor or electron acceptor. The dopant changes the charge carrier there by improving the conductivity of the semiconductor material. The donor atom have more valence electrons than the pure semiconductor therefore it donate electrons to the intrinsic semiconductor thereby promoting n-type semiconducting, while the accepter atom have fewer valence electrons therefore it accept electrons from the intrinsic semiconductor thereby promoting p-type semiconductor material.

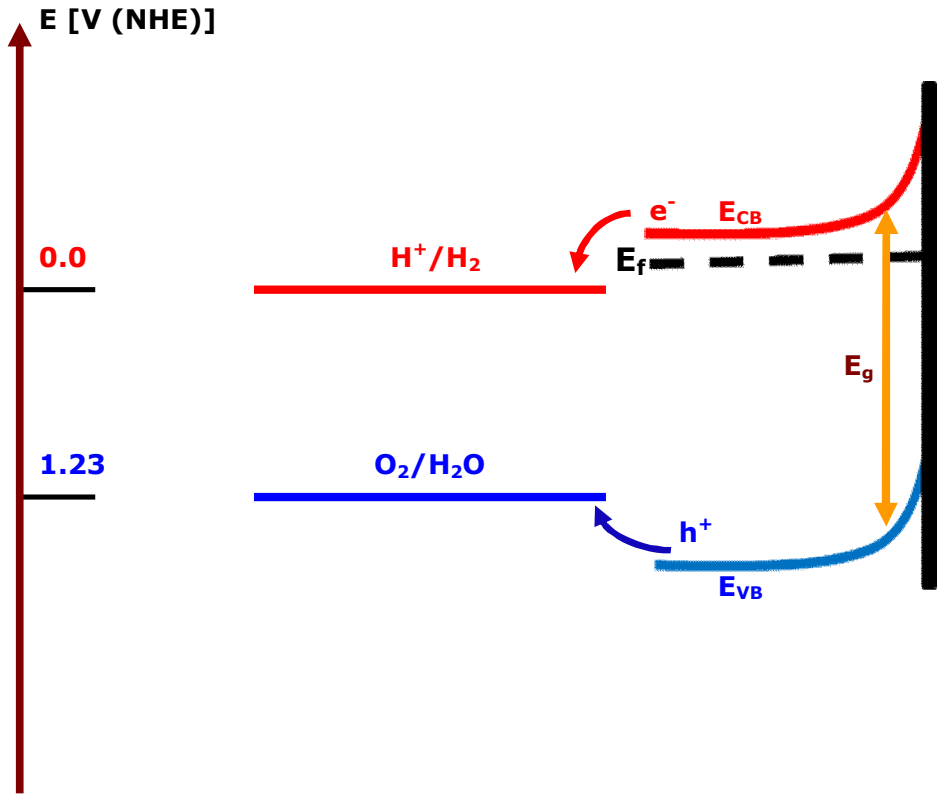

Figure 1.2 The schematic diagram of an n-type semiconductor band position in the electrolyte during the water splitting.

Furthermore, in order to successfully split water in to hydrogen and oxygen with solar irradiation suitable semiconductor electrodes are needed. These electrodes should be photocorrosion and chemically stable. During water splitting process on the photoelectrode, there would exist an anodic and cathodic photocorrosion due to the holes and electrons, which would be oxidizing and reducing the semiconductor, respectively. Photocorrosion decreases energy conversion efficiencies and shortens the lifetime of the photoelectrode. Therefore it is important to take into account the photocorrosion stability when designing the photoelectrode for photoelectrochemical process of water.

Following the discovery of the photocatalytic splitting of water on rutile (TiO_2) electrode by Honda and Fujishima in 1972, a lot of effort has devoted to the development of the low cost electrodes from transition metal oxide materials [6]. These materials have to fulfill several requirements such as:

- The band gap has to be larger than 1.23 eV. In practice ~1.9 eV is required to split water, since an additional 0.4 eV is needed to cover thermodynamic losses and ~0.3-0.4 eV for the over-potential [7, 8]. At the same time the band gap should be small enough to absorb an appreciable part of the solar spectrum.
- The conduction band edge has to be higher in energy than the water reduction potential so that the reduction of water will be energetically possible.
- The valence band edge has to be lower in energy than the water oxidation potential so that the oxidation of water will be energetically possible.
- A good stability in aqueous environments and resistant to photocorrosion.
- Efficient charge separation and transport. Fast charge transfer to avoid recombination.
- Non-toxic and environmental friendly.
- Low cost.

1.4. Motivation

Introducing hydrogen as a universal environmental friendly energy carrier demands efficient technologies facilitating separation of high purity hydrogen (i.e. 99.99% H_2) from industrial streams (e.g. products of coal gasification, process gases of refineries), purification, storage in a compact and safe way, and delivery of hydrogen to a consumer at high pressure. Availability of

high purity hydrogen is directly connected to the development of efficient methods for hydrogen separation, purification and storage. Separation and storage of high purity hydrogen from gaseous mixtures plays a vital role in the realization of the hydrogen economy. For this reason, there is an extensive ongoing research in many research institutions on separation development and storage of hydrogen for industrial and automotive applications. Such research is building the expertise and technology required to achieve a hydrogen economy.

Hydrogen of high quality produced may be used in energy generating devices such as the polymer electrolyte fuel cell. Due to the presence of platinum group metals at the polymer electrolyte fuel cell electrodes, and the resultant ease at which these electrodes are poisoned by trace quantities of gaseous species such as carbon monoxide, it is imperative that the hydrogen fuel be of the highest purity. It is acknowledged that the energy generating capacity of the polymer electrolyte fuel cell is significantly limited by the purity of the hydrogen fuel, and for this reason notable developments should be made into improving the separation media which produce high purity hydrogen from impure feed streams.

Solar hydrogen is a multipurpose energy carrier that can be used as a liquid fuel or converted to electricity. Solar hydrogen can be produced anywhere where water and sunlight are readily available, enabling distributed energy generation and reducing the dependence on countries rich in fossil fuels for energy supplies. Other renewable technologies, such as solar, wind, and hydrothermal have irregular supply, so storage of the produced electricity is required. The energy is often produced in remote areas, far from urban centers where the energy demand is the highest.

South Africa is surrounded by the ocean and receives a lot of solar radiation, which makes it suitable to produce solar hydrogen and has the potential to be a world leading country in hydrogen economy. However the vast majority of hydrogen present on earth is locked up in the form of water. The electrolysis of water to produce hydrogen is easily achieved using an electrochemical cell. The byproduct of hydrogen combustion, or the reaction between hydrogen and oxygen in a fuel cell, is theoretically only water. The solar spectrum shown in Figure 1.3 [9]

contains enough energy to split water, but this reaction does not occur spontaneously due to the optical absorption of water.

The absorption coefficient of water is very low (~ 10^{-2} m^{-1}) [10] in the UV-visible region of the electromagnetic spectrum, where single photons have sufficient energy to split water; hence an enormous path length would be required for significant absorption. However, sunlight can be used to excite a semiconductor photoelectrode, which acts as a catalyst for the water splitting reaction in an electrochemical cell. Therefore in this work we focus on the study of the physical properties of hematite semiconducting based photoelectrode materials that may be used in a photoelectrochemical cell to efficiently split water in to hydrogen and oxygen gas through solar irradiation. Direct water splitting is currently far less efficient than electrolyzing water using electricity produced using photovoltaics. Hematite (α-Fe_2O_3) is a mineral from iron (III) oxide and its properties are described in details in Chapter 2.

Hematite is found in banded iron formation and in places where there was water standing and hot spring and at the bottom of the lake because of mineral precipitation. It is abundant, non-toxic and low cost [11]. This material is chosen because of its photo corrosive resistant, photo catalyst and its band gap over other oxides for water splitting based application [12]. It has a band gap of 1.9-2.2 eV [13], which make it an ideal candidate for water splitting based application over other oxides.

Figure 1.4 shows other oxides with promising band gap but poor in water splitting application due to their lack of stability in the electrolytes. Desai et al (2005) [14] have reported that hematite has a strong chemical stability over a wide range of pH. The valence band position of hematite is well appropriate for the oxygen production. Like other oxide n-type semiconductors it also exhibit some short coming due to the position of the conduction band edge which is too low for the production of hydrogen without an external bias. The reported optimum band gap for the water splitting without an external bias is 2.46 eV [15].

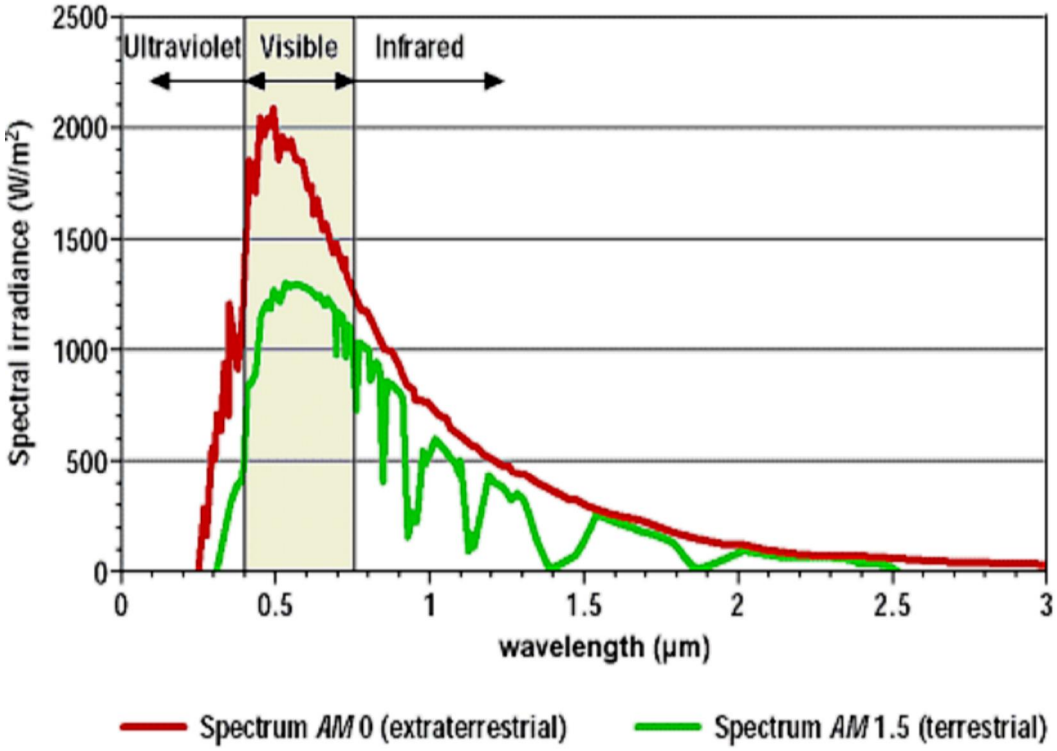

Figure 1.3 The solar spectrum useful to photoanodes for water splitting applications [9].

Therefore as described by Vayssieres et al (2005) [16], the blue shift due to the quantum confinement on the band gap of hematite; can be shifted the band gap by 0.3 to 0.6 eV upward to the conduction band edge, which makes it an ideal candidate for hydrogen production by water splitting. The other short coming of this material in a bulk form is the high resistivity (10^6 Ω cm), low electron mobility (0.01 to 0.1 cm^2/V.s) and very short diffusion length [17] (2 - 4 nm) which give very high rate of charge carrier recombination. At nanoscale level these disadvantages are substantially minimized.

The advantage of photoelectrochemical water splitting is its potential cost effective material processing compared to photovoltaic technologies. There is a tremendous research on water splitting going on to improve the efficiency of the splitting process to allow production of hydrogen on a commercial scale.

The well oriented nanorods arrays of hematite are purposely synthesized for the reason to improve the performance by increasing the active volume of material for photon absorption while reducing the distance that the holes and the electrons need to travel to reach the electrolyte or the underlying conducting substrate as shown in Figure 1.7 [18].

Figure 1.5, Figure 1.6, Figure 1.7 and Figure 1.8 are the typical example of a typical PEC cell, where a light-absorbing semiconductor electrode and a metallic counter electrode are immersed in an aqueous electrolyte solution [19]. When the photo-electrode is irradiated with photons from the sun that have an energy grater or equal to the band gap of the semiconductor, electrons get photo-excited from the valence band of the semiconductor into its conduction band. Therefore the photoelectrons travel to the back contact and are transported via the electrical circuit to the counter electrode, where they reduce water to form hydrogen gas. The photo-generated holes in the valence band diffuse/ migrate to the semiconductor-electrolyte interface, where they oxidize water to form oxygen gas. A target hydrogen production efficiency of 10 % has been quoted for water splitting technology to be commercially feasible [20-21]. This goal is based on current fuel and infrastructure costs and is likely to change depending on future economic and political conditions. This has led to a growing demand of renewable and alternative energy sources.

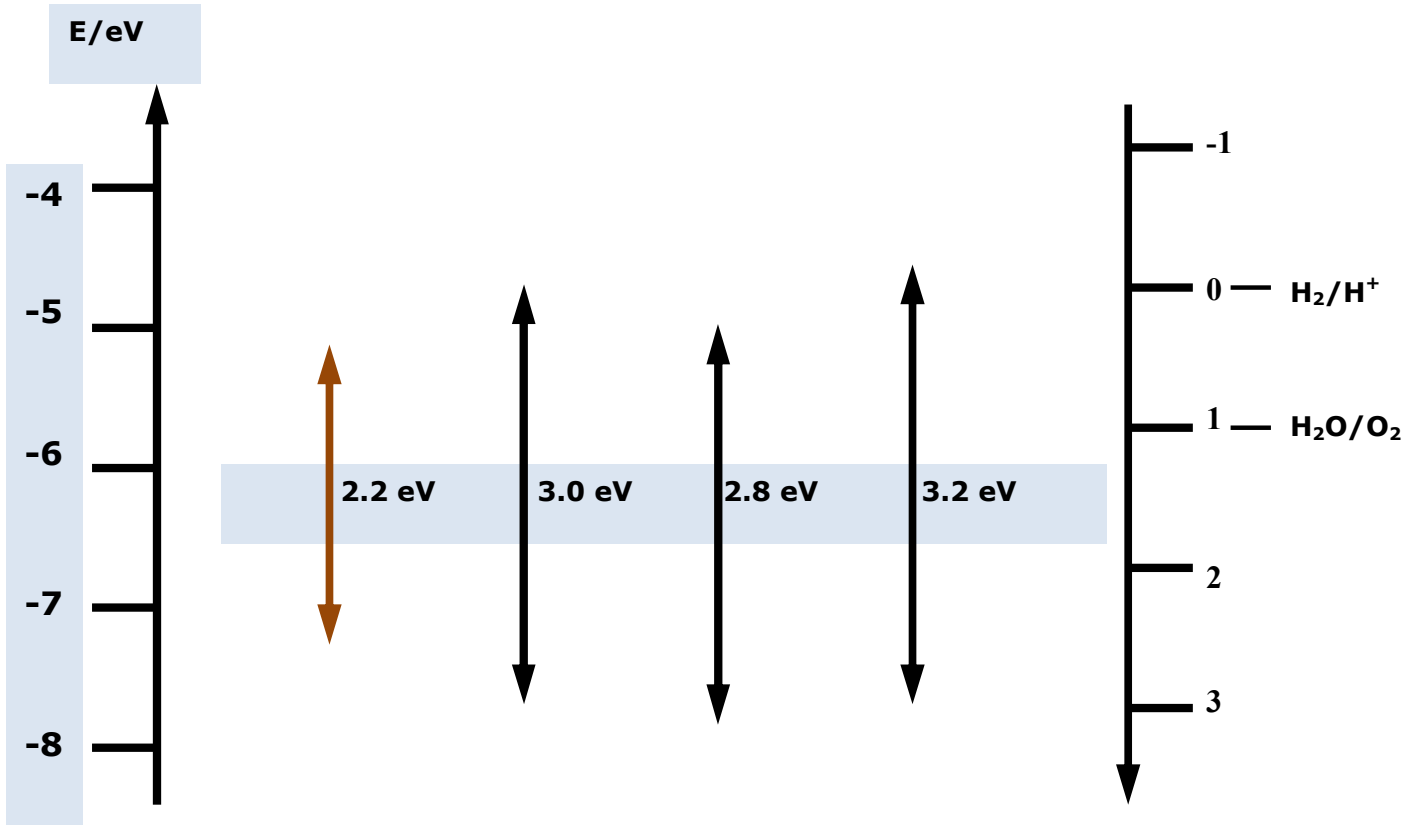

Figure 1.4 The overview of the band edge potentials of the common n-type semiconductor photoelectrode materials.

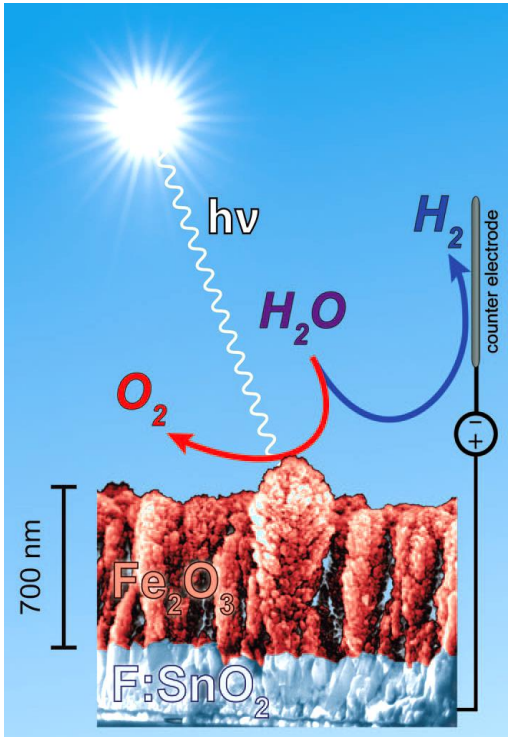

Figure 1.5 The schematic demonstration of water splitting using hematite a photoanode and solar radiation [12].

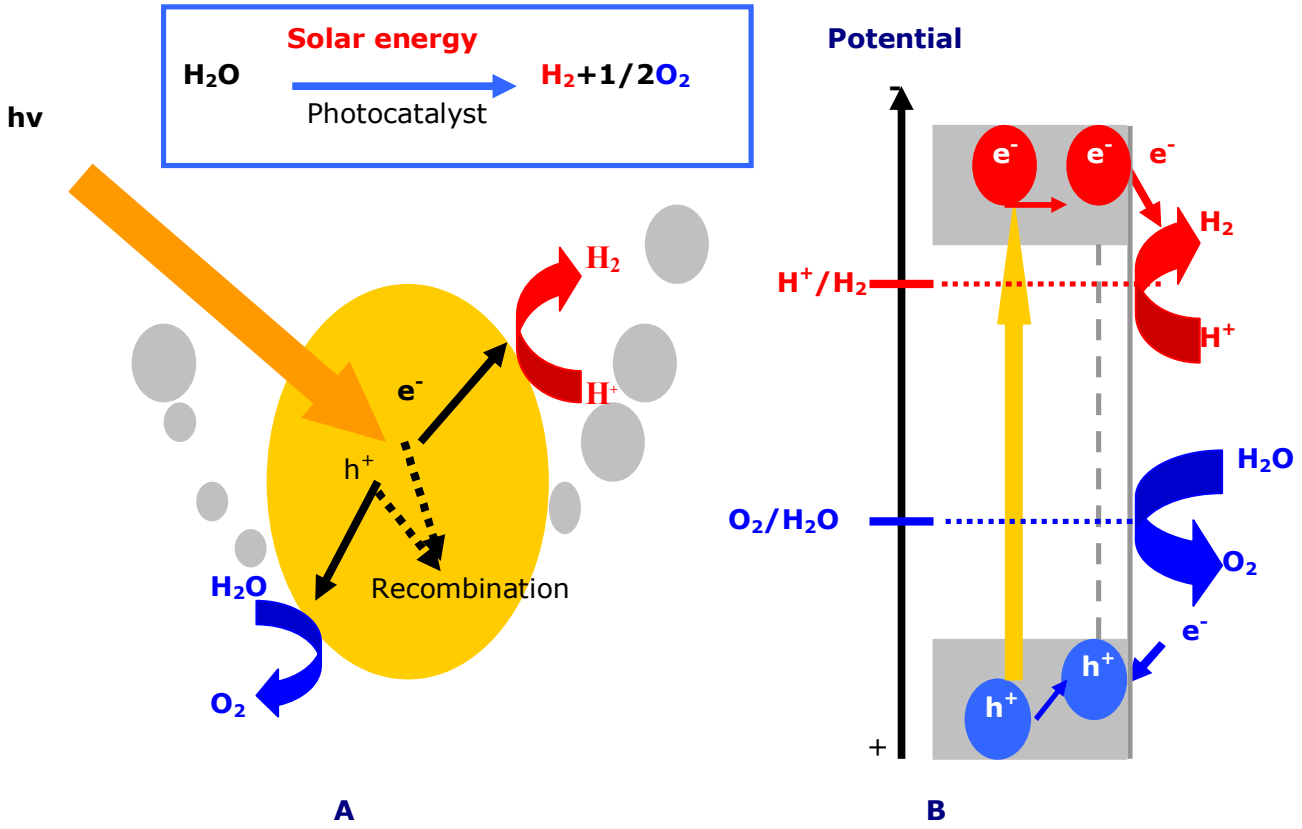

Figure 1.6 The schematic diagram representing the solar water splitting, (a) shows solar radiate and the separation of hole and electron without recombination and (b) shows the band gap and the movement of the holes and electrons to participate in the production of hydrogen and oxygen on the interface.

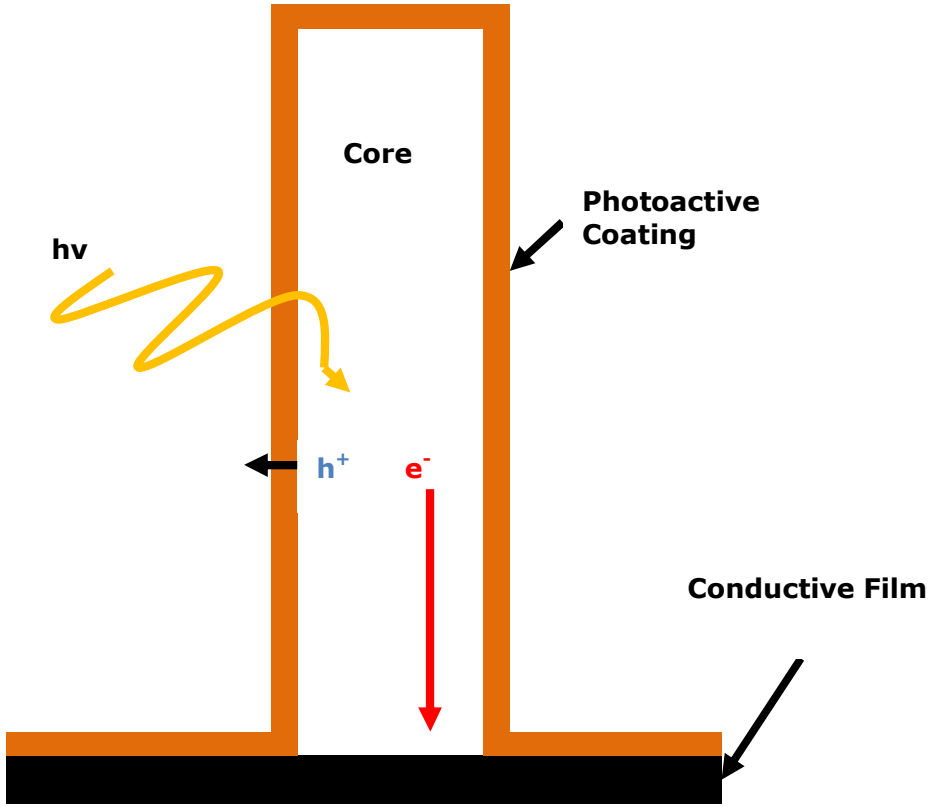

Figure 1.7 The schematic drawing showing the absorption of the photons (hɜ) by the photoactive layer and creation of the electron (e) and hole (h) pairs and arrows indicate the direction of holes and electrons respectively adapted from ref [18].

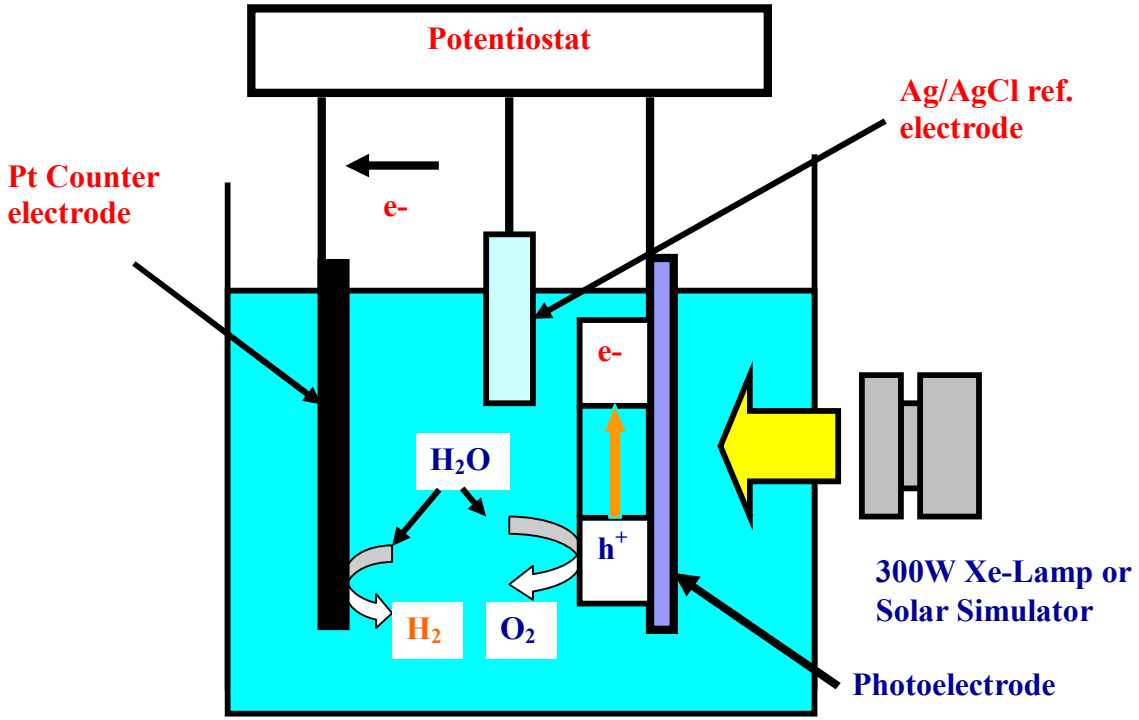

Figure 1.8 Schematic diagram of water splitting using the photoelectrode and a solar simulator in the electrolyte and the platinum electrode and the silver/silver chloride reference electrodes are used. The hydrogen and the oxygen evolution takes place in on the interface of the platinum and photoelectrode, respectively, adapted from ref [19]

1.5. Objectives

In this research work we aim to synthesize rod like structures in the nanoscale region of iron oxide (α-Fe_2O_3) and study their physical and chemical properties for the improvement of the water splitting efficiency by increasing the active volume of material for photon absorption while minimizing the electron-hole recombination rate by reducing the distance that the holes and the electrons need to travel to reach the electrolyte before recombination. More specifically the well oriented nanorods arrays of hematite are purposely synthesized.

1.6. Thesis Outline

- The introduction and motivation is presented in Chapter 1: this is directed to the basic introduction of the energy crisis and demands for an alternative energy source and the semiconductor material requirement based water splitting.
- The literature survey, on the physical and chemical properties of the hematite is presented in Chapter 2, where the recent progresses on water splitting and on hematite photo-anode are also described.
- Chapter 3 is devoted to the synthesis methods of hematite nanostructures.
- Chapter 4 is devoted to the brief description of the physical principles of all characterization techniques used in this work.
- Chapter 5 presents the experimental results and discussions.
- Finally, chapter 6 presents the conclusions.

CHAPTER II

2. LITERATURE REVIEW

2.1. Introduction

This chapter provides the context for the themes explored within this work. The underlying aspects are iron oxides, their structures, functional properties and applications on water splitting. Emphasis is placed upon the physical properties of hematite, providing a benchmark from which the water splitting is based.

2.2. Hematite (α-Fe_2O_3) material

Iron is abundant in the earthôs crust and an important element in our environment [22]. It is present in soils as oxides [23] and easily mobilized in natural waters in the form of molecular complexes and colloids. There are number of iron oxides, hydroxides and oxy-hydroxides, with different crystal structures as summarized in Table 2.1. For simplicity, this group of iron oxi ((oxy) hydroxi) des is often referred to as iron oxide.

The structural chemistry of these compounds is diverse, reflecting the large number of atomic structures, as summarized in Figure 2.1[23-24] and Figure 2.2. Almost all these phases can be formed from chemical solution, alluding to a complicated chemistry of their formation [23,25,26]. In particular, the diversity of physicochemical conditions present in the environment (*e.g.* acidity, redox conditions, temperature, salinity, presence of organic or inorganic ligands, *etc.*) suggests, practically, all the iron oxide phases can be found naturally. The high versatility of iron chemistry in an aqueous medium originates from two factors: the occurrence of two oxidation states, Fe^{2+} and Fe^{3+}, which are stable over a large range of acidity, and the high reactivity of iron complexes towards acid-base and condensation phenomena [24]. α-Fe_2O_3 is the most thermodynamically stable iron oxide phase and is of particular interest because of its high resistance to photocorrosion, low processing cost and non-toxicity [23]. This multifunctional material has therefore been investigated extensively for a variety of applications including photo-catalysis [27], gas

sensing, magnetic recording [28-29], drug delivery [30], tissue repair engineering [31] and magnetic resonance imaging [32], along with its use in lithium-ion batteries [29], spin electronic devices [33] and pigments [34]. In particular, the magnetic properties of α-Fe_2O_3 have attracted much interest over the past decades. In the 1950s it was found to be canted antiferromagnetic (weakly ferromagnetic) at room temperature, antiferromagnetic below the Morin transition temperature of 250 K and paramagnetic above its Néel temperature of 948 K.

2.3. Crystal structure of hematite

Hematite crystallizes in the trigonal system with the space group of R-3c and the oxygen atoms are arranged similar to the corundum structure [18]. The unit cell is rhombohedral with the lattice parameters a=0.50356 nm, c=1.37489 nm. The packing of the anions, O^{2-}, in the hematite structure are arranged in a hexagonal closed-packed lattice along the [001] direction. The cations (Fe^{3+}) occupy the two-thirds of the octahedral interstices (regularly, with two filled followed by one vacant) in the (001) basal planes, and the tetrahedral sites remain unoccupied. The cations arrangement lead to the production of pairs of FeO_6 octahedra that share edges with three neighboring octahedra in the same plane and one face with an octahedron in an adjacent plane in the [001] direction, see Figure 2.2 [35] and Figure 2.3 [36].

The face-sharing is responsible for a trigonal distortion of the octahedra as the proximal iron atoms are repelled to optimize the crystalôs Madelung energy. Consequently, hematite exhibits C_{3v} symmetry and there are two different Fe-O bond lengths, as illustrated in Figure 2.3. However, the electronic structures of the distorted FeO_6 octahedra are said to be similar to undistorted clusters [23].

Oxides	**Oxy-Hydroxides and Hydroxides**
Fe_2O_3, iron (III) oxide has a rhombohedral (hexagonal)structure with lattice parameters: a =0.5427 nm, c = 1.37524 nm, *Z* = 6	Goethite (α-FeOOH) has an Orthorhombic structure with lattice parameters: a = 0.9956 nm, b = 0.30215 nm and c = 0.4608 nm
Fe_3O_4, iron (II, III) Oxide (Magnetite) has a Cubic structure with lattice parameters: a = 0.83941nm, a = 90.00, Z = 8	Akaganeite (β-FeOOH) has a Monoclinic structure with lattice parameters: a = 1.056 nm, b = 0.3031 nm and c = 1.0483 nm
FeO, Iron (II) oxide, (wüstite) has a structure ($Fe_{1ï x}O$): cubic, space group O_h^5ï Fm3m, *Z* = 4	Lepidocrocite (γ-FeOOH) has an Orthorhombic structure with lattice parameters: a = 0.3071 nm, b = 1.2520 nm and c = 0.3873 nm
Hematite (α-Fe_2O_3), has a rhombohedral structure with lattice parameter: a=0.50356 nm, c=1.37489 nm and z=6	Feroxyhyte (δ-FeOOH) has a Hexagonal structure with lattice parameters: a = 0.293 nm and c = 0.456 nm
β-Fe_2O_3 has a body-centered cubic ñbixbyiteò structure with a = 0.94039 nm	Ferrihydrite: (Fe_5HO_8. $4H_2O$ approx.) has a Trigonal - Hexagonal Scalenohedral structure with lattice parameters: a = 0.296 nm, c = 0.94 nm, Z = 1
γ-Fe_2O_3, maghemite has Cubic and tetragonal structure with lattice parameters: a = 0.83474 nm and , c =2.5042 nm	Iron (II) hydroxide (Fe(HO)2)
ε-Fe_2O_3 has an orthorhombic structure, with lattice parameters: a = 0.5095 nm, b = 0.8789 nm and c = 0.9437 nm	Iron (II) hydroxide (Fe(OH)3), (bernalite)

Table 2.1 The phases and polymorphs of iron oxides in nature.

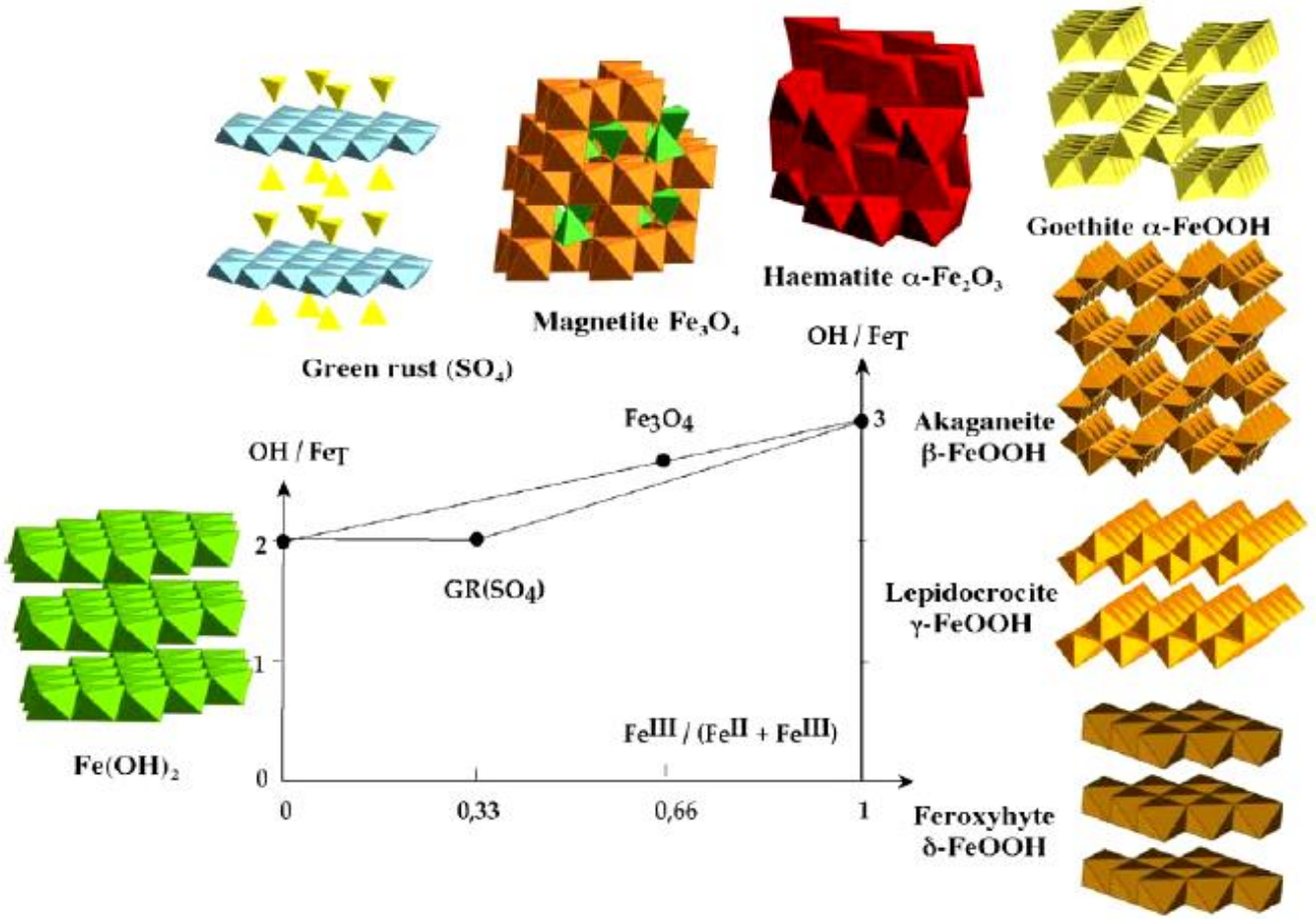

Figure 2.1 The diagram that shows the different phases of iron oxi ((oxy) hydroxi) des formed as a function of hydroxylation ratio and composition in the ferrousï ferric system [24].

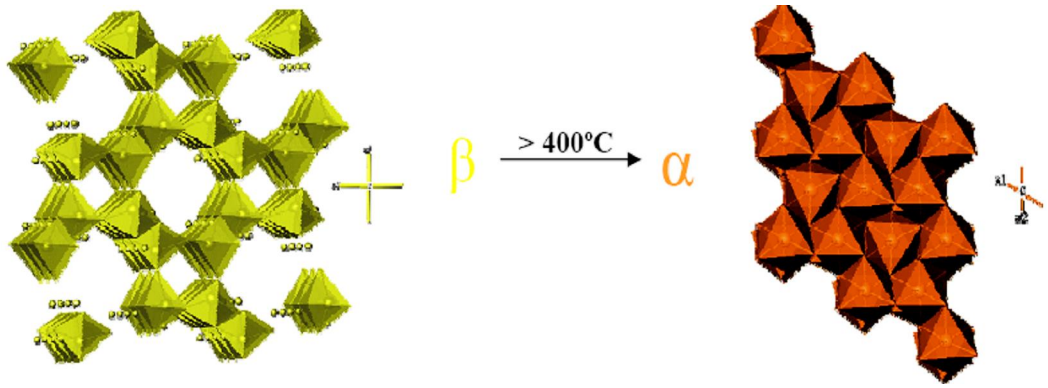

Figure 2.2 The crystal structural phase transition from akaganeite (ϐ-FeOOH) on the left to hematite (Ŭ-Fe_2O_3) on the right that occurs above 400°C [35].

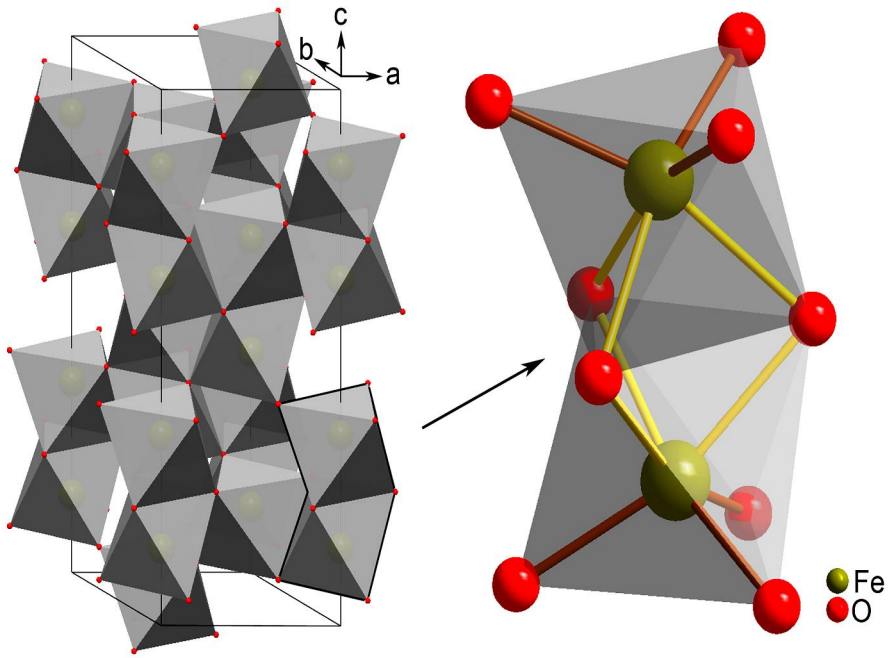

Figure 2.3 The unit cell (left) of hematite that shows the octahedral face-sharing Fe_2O_9 dimers forming chains in the c direction. A detailed view (right) of one Fe_2O_9 dimer shows the electrostatic repulsion of the Fe^{3+} cations produce long (yellow) and short (brown) Fe-O bonds [13].

2.4. Magnetic properties of hematite

The arrangement of the oxygen anions and the high-spin (d^5) cations naturally affect the orientation of the iron atomsô spin magnetic moment and thus the observed bulk magnetic properties. The diverse magnetic properties of all the iron (III) oxides have been recently reviewed [37].

Hematite is antiferromagnetic at temperatures below 260 K and a weak (parasitic) ferromagnetic at room temperature, this is due to the ferromagnetic coupling of the spins within the (001) basal planes and antiferromagnetic coupling between iron layers along the [001] direction [38]. Here the trigonal distortion of the FeO_6 octahedra produces a slightly canted (about 58) spin arrangement, causing the destabilization of their perfectly antiparallel arrangement (parasitic ferromagnetism).

While the magnetic properties of hematite are not particularly relevant to its photoelectrochemical performance, the iron spin configuration does influence the optoelectronic and carrier transport properties of hematite. These attributes should be properly understood for its application as a semiconductor for solar water splitting [12].

2.5. Optoelectronic properties of hematite

Hematite has a band gap of 1.9 eV to 2.2 eV depending on the preparation and it absorb near infrared due to the d-d transition state between electron energy level of the Fe^{3+} ions [12]. The photo-excitation increases it conductivity but its photocurrent in the photoelectrochemical systems under irradiation does not occur below the band gap [12]. The absorption coefficient of a pure hematite starts to increase at the band gap.

Hematite has a characteristic reddish colour, which is due to the fact that it strongly absorbs from yellow to ultraviolet photons and transmits from orange to infrared photons. Hematite have an indirect band gap transition which is due to the parabolic energy band with respect to the crystal momentum which indicate an indirect band gap transition [12],

while the direct band gap is due to the quantum size effect [39]. The initial orbital assignment of the band gap has been suggested that is due to the indirect transition of the Fe *d-d* origin and the direct transition of charge transfer form O2p orbital to the Fe *3d* does not occur until 3.2 eV. The lowest unoccupied energy band is attributed to Fe *3d* and the highest occupied energy band is due to Op [36].

2.6. Charge transport of hematite

It is very important to study the charge carrier transport as itôs the most important parameter for water splitting when using hematite as a photoelectrode. Hematite has a diffusion length of holes of only of 2-4 nm [40-41,42], which is about 100 times lower than many other (III-V) oxides. Hematite has a high rate of recombination of electrons and holes, trapping of electrons by oxygen deficiency sites and a low mobility of the holes, cause a low conductivity and accordingly a low photo-response [43]. It has been reported that the electron mobility is in the range of 0.01 [44] to 0.1cm^2/V.s [45]. The electron mobility in hematite was found to be independent of the donor concentration.

The electron mobility of about 0.1cm^2/V.s has been reported on a doped single crystal hematite which is independent of a donor concentration [46]. Polycrystalline hematite have a low conduction of ($10^{-14}q^{-1}cm^{-1}$) with the conduction electron concentration of $10^{18}cm^{-3}$ at 1000K, and the electron mobility of an order of $10^{-2}m^{-2}V^{-1}cm^{-1}$ and 10^{-6} $q^{-1}cm^{-1}$. The low electrical conduction can be explained by the Fe^{3+}/Fe^{2+} localized in the 3d orbitals [12].

The ferromagnetic coupling of the spin in the (001) basal plane and the antiferromagnetic coupling of the spin in the [001] direction create the environment where (in case on an n-type conductivity) electron can move within the iron bilayers (an environment of parallel spin) but are forbidden to hop across the oxygen planes to the iron bilayers with an opposite spins.

The conduction in the [001] direction could only involve the movement of holes in the form of Fe^{3+} to Fe^{4+}, which is very slow in hematite. This has been suggested that it arise from the slowness of both holes and electrons transport across the basal oxygen planes. The explanation does not consider electron transport to be forbidden in the [001] direction, but instead identifies the most important factor that influences the carrier mobility to be the electron coupling ï a quantity found to depend on both the super-exchange interaction between the bridging oxygen atoms and the d ï shell electron spin coupling [40, 47].

2.7. Hematite based photo-electrode

Since the realization of water splitting using TiO_2 photoanode [48, 49] there has been an extensive search for an ideal semiconducting material for hydrogen production. Metal oxides like ZnO [50, 51], TiO2, [52] and WO_3 [53] semiconductors and non-metal oxides semiconductors like GaAs and CdS [54] have been studied.

Hematite (α-Fe_2O_3) [55, 56,57] has been realized as the most promising photoelectrode, which demonstrate a set of close ideal properties for photo-assisted water splitting. Several phases of iron oxide have been realized as presented in Table 2.1, which includes goethite (α-FeOOH), Lepidocrocite (γ-FeOOH), akaganeite (β-FeOOH), Feroxyhite (δ-FeOOH), magnetite (Fe_3O_4), wüstite (FeO) and hematite (α-Fe_2O_3). A thermodynamic stable crystallographic phase of iron oxide, which is derived straight from a natural occurring phase akaganeite (β-FeOOH) by heat treatment at the temperature above 390 ^oC, is hematite (α-Fe_2O_3) [14]. It has attracted much attention because of its great advantages, such as thermally stable, chemically stable over a wide range of pH>3 [58], environmentally friendly, photocorrosive resistance and photocatalytic properties [59-60].

Since this material has a band gap of 1.9 eV - 2.2 eV [43] it is capable of absorbing 40% [61] of the terrestrial solar radiation at AM 1.5 [62] and has a donor concentration of $2.5x10^{17}$ cm^{-3} [63]. The current photoconversion efficiency is much lower than the targeted maximum efficiency of 10% [64]. Recently, it is reported that hematite has a high

theoretical solar-to-hydrogen conversion efficiency of 14% to 17% (based on the lower heating value of hydrogen), which corresponds to a photocurrent of 11-14 mA cm^{-2} [65]. The challenge in this material is due to the fact that its valence band and conduction band alignments permits water oxidation to produce oxygen [22], but it cannot form hydrogen without an external applied voltage. Some of the limitations reported on hematite have to be overcomed to improve its photo-water splitting application. Therefore, there are several approaches that have been employed to improve the semiconductor based water splitting application that is including the thin film growth, nanostructured particles and doping.

Since the resistivity of the semiconductor and the light absorption reaches an optimum values at an optimal thin film thickness, therefore, hematite thin films with each thickness (ca. 60 nm) below that of the space charge region, were successively stacked and in contact with the solution with light passed through each electrode using 0.5 Na_2SO_4 and NaOH (pH 13) under the solar irradiation. Under the similar conditions, the photocurrent of the stacked hematite electrodes of (1.6 mA. cm^{-2}) increased by over three times relative to that of thick hematite electrode (ca. 1um, 0.5 mA. cm^{-2}) [66].

Therefore it was demonstrated that the charge carrier recombination could be minimized for hematite photoelectrodes by film of thickness below the width of the space charge layer synthesis. The nanostructuring technique can also be employed to address hematite limitations. In principle nanostructured material have an improved performance compare to the bulk one. Therefore nanocomposite electrode, in principle is able to improve its performance by increasing the active layer volume of the material for photon absorption while reducing the distance that the hole and electron have to travel in a high resistive semiconductor material to participate in the oxidation and reduction of water, respectively [67].

A nanocomposite hematite photoelectrode composed of a thin layer of hematite deposited on the nanostructured substrate with a very high surface area, where the conduction band edge of the hematite thin layer must be always lie above that of the substrate to

minimized the potential barrier for the easy transport across of electron from hematite to substrate at the interface has been reported in literature. To avoid competition of light between the film and the substrate, therefore substrates with a high band gap than hematite are employed. Glasscock et al (2006) [67] demonstrated how to fabricate this type of nanocomposite and reported that the quantum efficiencies of the nanocomposite photoelectrodes were lower than the equivalent thin films through the improved absorption of long wavelength photons. Hematite thin films with a structure of nanorods have been reported to be avoiding recombination losses that can occur on the grain boundaries between nanoparticles compared to the nanostructured thin films consisted of interconnected spherical particles [39] as shown in Figure 2.4 and Figure 2.5.

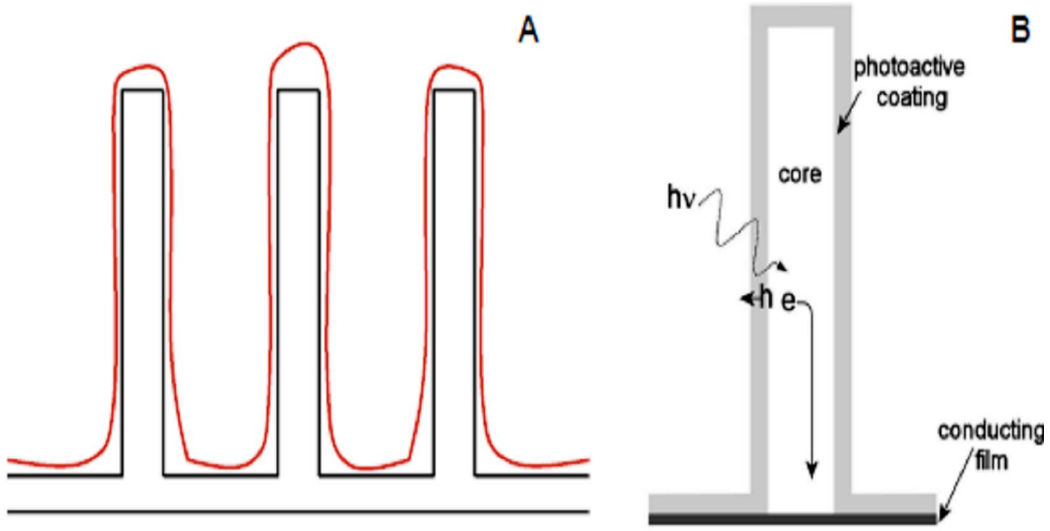

Figure 2.4 Schematic illustrations of the nanostructured photoelectrode design: (A) cross section of an array of coated nanowires, (B) cross section of a single coated nanowire showing charge transfer mechanism. A narrow band-gap photoactive semiconductor is coated onto a nanostructured substrate to optimize the absorption and charge transfer properties from ref [67].

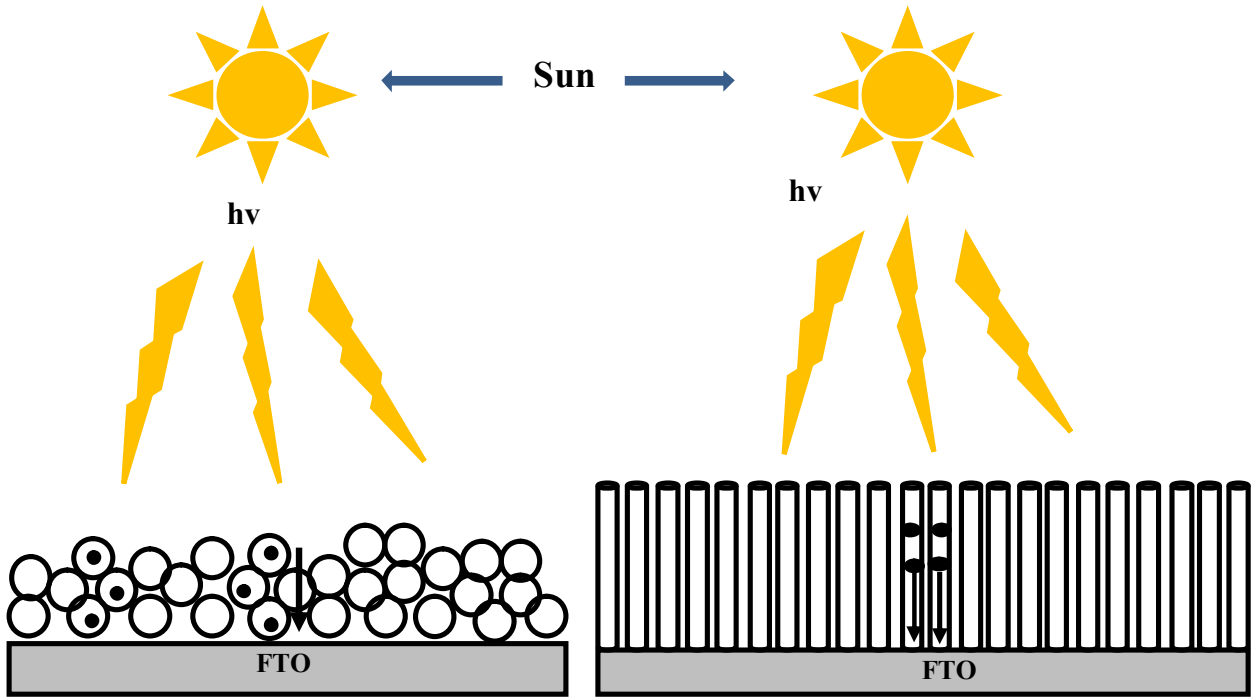

Figure 2.5 The schematic diagram of the spherical particles (on the left) and the rods like particles (on the right) showing the movement of electrons to the back contact. The **dots** in the diagram are electron and the arrows indicate the direction electron after hole- electron pair has been created. In the spherical particles electron has to overcome grain boundaries and in the rods structure has no grain boundaries so the electrons move fast to the back contact adapted from ref [67].

CHAPTER III

3. The Synthesis Methods of α-Fe_2O_3 nanostructures.

There is an enormous effort that has been made over the years to develop a very good photoactive nanostructured hematite (α-Fe_2O_3) photoanodes/ electrodes. A brief overview of several synthetic methods for the fabrication of the nanostructured hematite materials is discussed. This section is meant to provide a good reason for the selection of our synthetic methodology for our hematite nanostructures.

In nanotechnology, large scale manufacturing of nanostructures still remains a challenge. The synthesis methods differ in the degree of complexity, cost, manufacturability, and environmental hazard [68]. Wet chemistry or solution-based method is a scalable method that is used to synthesize nanostructures of α-Fe_2O_3 with different morphologies, sizes and shapes. The α-Fe_2O_3 nanoparticles [69], nanowires [70], nanotubes [71,72,73] hollow spheres [74, 75], colloidal [76] and nanoflowers [77], has been synthesized using solution-based methods [78]. The solution based methods refer to growth methods such as hydrothermal [79] solvothermal [80,81] and solï gel [82]. For example, a solvothermal method have been utilized to synthesize 3D flower-like hematite nanostructures by Zhong et al (2006) [83] while a hydrothermal method was used to fabricate a porous α-Fe_2O_3 nanorod arrays on fluorine doped tin oxide (FTO) conducting glass by Vayssieres et al (2001) [84]. These methods demonstrated that morphological control of α-Fe_2O_3 can be achieved. The solï gel method is the simple and economical method to synthesize hematite nanostructures [85]. For an example this growth method (solï gel) was utilized by Woo et al (2003) [86] to synthesize α-Fe_2O_3 nanorods with a very small size of about 7ï 24 nm.

Another extensively applied methods to synthesize various nanostructured and thin film of hematite with different morphologies such as nanowires, nanorod arrays, nano-dendritic structures and thin films [87, 88, 89, 90] is the gas deposition methods, which includes physical vapor evaporation, chemical vapor deposition, atomic layer deposition, and reactive sputtering [91, 92, 93]. For example, the vertically aligned single crystalline nanorod arrays of α-Fe_2O_3 synthesized on a

silicon substrate using metal organic chemical vapor deposition (MOCVD) was reported by Wu et al (2006) [94]. The atmospheric pressure chemical vapor deposition (APCVD) was utilized by Cesar et al (2006) [95] to synthesize the perpendicularly oriented dendritic silicon-doped α-Fe_2O_3 nanostructures that exhibited large surface area, and good contact between the α-Fe_2O_3 and the growth substrate, which is critical for charge carrier transfer.

Atomic layer deposition (ALD) is a unique method to fabricate tunable ultra-thin films with high crystal quality. Lin et al (2011) [88] used atomic layer deposition (ALD) to deposit a high-quality, ultra-thin α-Fe_2O_3 film on $TiSi_2$ nanonets. The film thickness is comparable to the diffusion length of minority carriers. $TiSi_2$ nanonets were used as templates for the deposition of α-Fe_2O_3 film and served as a conducting network to facilitate the charge transport. Reactive sputtering is another commonly used method for thin film materials. Hahn et al (2010) [96] used a reactive ballistic deposition method to fabricate α-Fe_2O_3 thin films. The film morphology can be tuned by deposition angles by taking advantage of ballistic shadowing.

Gas-based methods can also be used to fabricate nanostructures in combination with templates. For example, hematite nanotube arrays were prepared by deposition of hematite onto ZnO nanowire arrays [97]. Thermal oxidation and pyrolysis are important approaches for the synthesis of nanostructured α-Fe_2O_3. Thermal oxidation of iron metal is the most direct approach to obtain α-Fe_2O_3 [98, 99, 100, 101]. By controlling the oxidation parameters, different morphologies of α-Fe_2O_3 have been synthesized, including nanoparticles, nanowires, and nanoflakes [98, 102]. For example, Rao and Zheng used a flame synthesis technique to synthesize densely aligned α-Fe_2O_3 nanoflake arrays [98]. The morphologies of α-Fe_2O_3 can be manipulated with the end result being differences in nanoflake widths and lengths by changing various synthetic parameters, such as annealing temperature and atmosphere. Moreover, hematite thin films can be prepared by thermal pyrolysis.

Spray pyrolysis is one of the most common methods to deposit thin films [103, 104]. By spraying an iron precursor solution such as $FeCl_3$ or iron organic precursors such as iron acetylacetonate on a heated substrate, [105] the iron precursor decomposes during thermal treatment in air to form hematite. Duret and Grätzel further extended this approach to fabricate mesoscopic α-Fe_2O_3

leaflet films by using ultrasonic spray pyrolysis resulting in films with higher photo-activity relative to conventional spray pyrolysis techniques [106]. Wang et al (2011) [107] used a deposition-annealing process to deposit α-Fe_2O_3 film onto FTO glass. Particle sizes and thicknesses of the thin films can be tuned by controlling deposition parameters such as cycle numbers and precursor concentrations.

Although high quality nanostructured hematite films have been prepared by vapor phase deposition methods, each technique has its own drawbacks. For example, the iron precursors used in MOCVD and APCVD methods are typically flammable and highly toxic. While ALD is able to grow ultrathin single-crystal hematite films, it comes with a higher fabrication cost compared to solution-based methods. While the preparations of α-Fe_2O_3 nanostructures with different morphologies such as nanowires and nanorod arrays have been demonstrated by using vapor phase and solution-based methods, thermal pyrolysis methods have mainly been used for the growth of nanoparticle thin films.

The method of synthesis in this work is solution based chemical techniques because of its most economical and simplest technique for the fabrication of 1-3 D nanostructures arrays on a large scale. This technique contributes significantly on the manufacturing of raw nanostructures and plays a big role in the fabrication of practical nanodevices. This synthesis method is the aqueous chemical growth (ACG) [108, 109].

Aqueous chemical growth (ACG) is a well-known technique and the theory behind it was well described by Vayssieres et al (2004) [110]. It is a template free, surfactant free, environmental friendly, low temperature, cost effective and less hazardous synthesis method to synthesize hematite nanostructures. This synthesis method allows the opportunity to synthesize and controlled particles size, morphology, orientation, and crystal structure of nanostructures, in the purpose-built nanomaterials [111], to analysis, tune, and optimize their physical and chemical properties. Full coverage and strong adhesion of the nanostructures on the substrate is easily achieved with this method.

Experimentally, the setup of the aqueous chemical growth simply consists of laboratory oven for the heating of an aqueous solution of metal precursors (salts or complexes) at a given ionic pH and ionic strength, in the presence of substrates at mild temperatures (below 100°C) in a closed bottle as illustrated in Figure 3.1. Nanostructures with different shapes, morphologies and patterns on various substrates are achieved as shown in Figure 3.2.

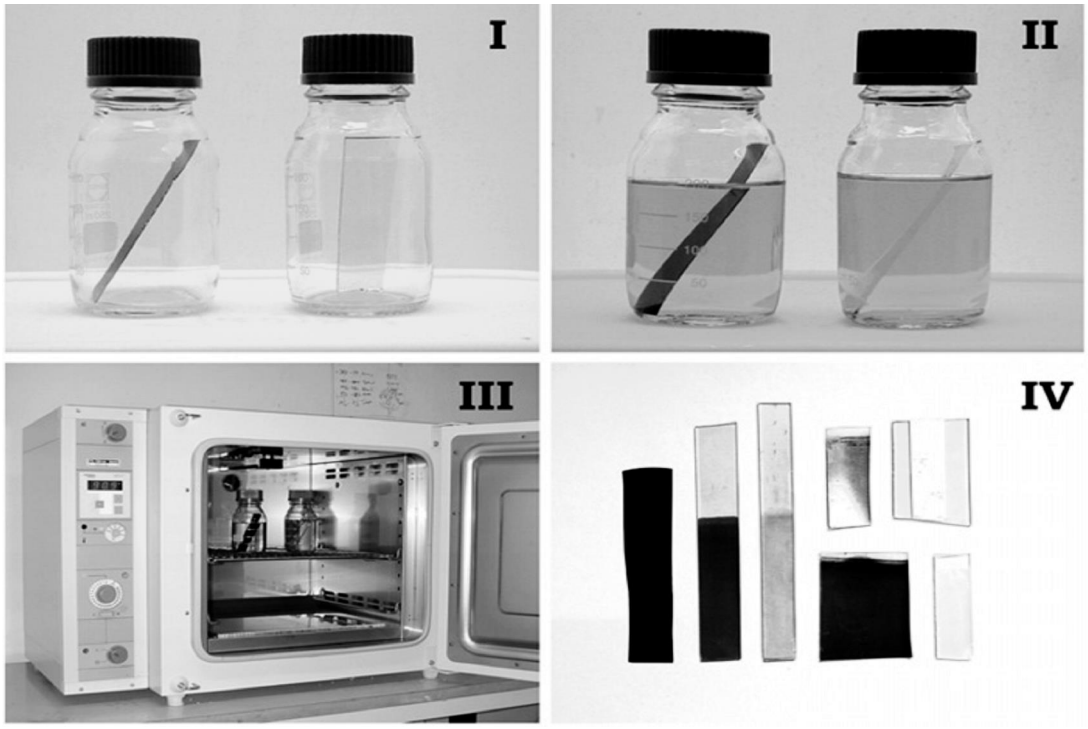

Figure 3.1. The aqueous chemical growth (ACG) technique, where: **I.** The bare substrates is introduced into the autoclave bottle; **II.** The room temperature immersions of the substrate into aqueous solutions of metal salt precursors in the bottle. **III.** Heating of the aqueous solution with substrate at constant temperature in a laboratory oven below 100°C. **IV.** Substrate covered with nano-, meso-, and micro-particulate thin films [110].

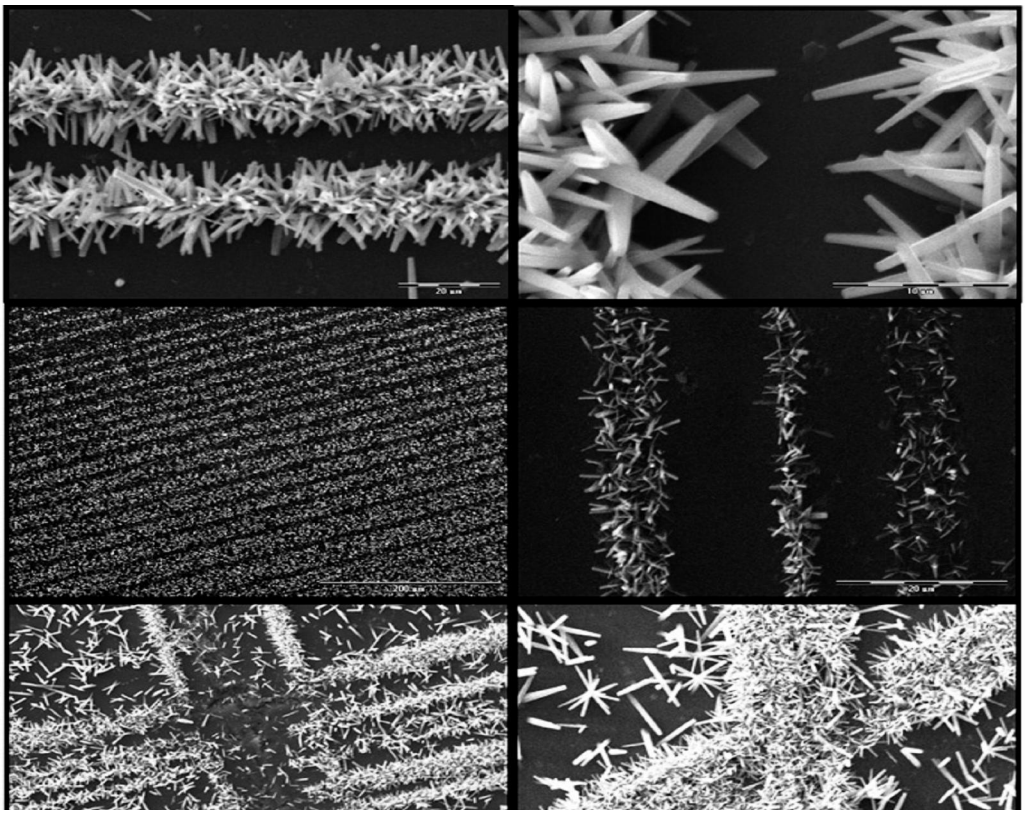

Figure 3.2 SEM images for various 3-D patterned arrays of metal oxide (ZnO) grown by ACG onto commercial Si wafers [110].

CHAPTER IV

4. CHARACTERIZATION TECHNIQUES

4.1. Characterization of α-Fe_2O_3

The deposited samples have been subjected to different characterization techniques for further investigate for various properties. The following sections give a brief description of the used characterization techniques.

4.1.1. Uv-Vis near Infrared spectroscopy

The direct optical absorption (A) and Transmission (T) measurements were made over a wavelength ranging from 200 to 1100nm conducted at room temperature on a Cecil 2000 spectrophotometer unit at iThemba LABS. It uses two different non cooled detectors. The principle of the UV-Vis is that, the photons with energies equal or greater than the band gap of the material get absorbed and excite electrons from the high occupied molecular orbital (HOMO) to the low unoccupied molecular orbital (LUMO). Photons with lower energies get transmitted therefore they do not excite electrons in the material. Therefore to calculate the band gap, the following equations were used.

$$(\alpha h\upsilon)^2 = A(h\upsilon - Eg) \quad [112,113] \qquad 4.1$$

$$\alpha = -\ln(x)/d \qquad 4.2$$

, x is the absorbance values,

$$h\upsilon = E = h\frac{c}{\lambda} \qquad 4.3$$

where λ and c are wavelength and speed of light, respectively.

4.1.2. FTIR analysis

Fourier Transform Infra-Red (FT-IR) spectroscopy provides information about the chemical bonding and molecular structure for both organic and inorganic materials. It also provides the information about the vibration bands of the particles in a specimen. Infrared measurements were undertaken using FT-IR spectrometer over a wavenumber range from 200 to 4000 cm^{-1}. IR bands can provide information about the particle crystal structure.

4.1.3. Electron Microscopy (EM)

The scanning electron microscope reveals information about the morphology, chemical composition, of the samples by scanning the surface with a high energy beam of electrons. SEM is equipped with Energy Dispersed Spectroscopy (EDS) [114], which is used to identify and quantify elements present on a specimen. It can also give the information about the thickness of the sample. Figure 4.1 shows the photograph image and the principle of the SEM unit used during this thesis work. The morphology was studied using a Leo-Stereo Scan 440 Scanning Electron Microscope (SEM) at different magnification and tilting angle. The transmission electron microscope (TEM), in Figure 4.2, provides the information about the structure shape and size of the samples.

4.1.4. X-ray diffraction

The photograph of the X-Ray Diffraction (XRD) unit presented in Figure 4.3 is a non-destructive analytical technique which can give the information about the crystallographic structure and chemical composition of materials and thin films. This technique is based on monitoring the scattered intensity of an x-ray beam hitting a sample as a function of incident and scattered angle, polarization, and wavelength or energy [115, 116, 117]. In crystalline structures the atoms are arranged in a periodic lattice with planar (d-spacing). Constructive interference of x-rays of wavelength occurs when the Bragg [118] condition is satisfied by,

$$n\lambda = 2d\sin\theta \qquad 4.4$$

Where n is an integer and θ is the angle of incidence. Therefore, by scanning a range of angle of incidence, the characteristic d-spacing of the crystal can be identified [119]. The x-ray diffraction pattern of the synthesized material is qualitatively compared with a reference database to identify the crystallographic phase. Reference patterns are generated from powder samples, where all possible crystallographic orientations are present. Further analysis of XRD patterns gives much information about the structure of the sample, including the crystal size, amorphous component and degree of stress in the lattice. X-Ray Diffraction was carried out on the XRD unit at iThemba LABS using a Bruker AXS D8 Advance X-ray diffractometer with primary monochromatic high-intensity Cu KŬ(∂=1.541 Å) radiation with a PSD (position sensitive detector) detector at the scan step of 0.007^0 and scan speed of 1 step/s.

Further analysis of XRD patterns can yield much information about the structure of the sample, including the crystal size, amorphous component and degree of stress in the lattice. The Scherer equation shown below can be used to calculate the crystal size D along a given plane

$$D = \frac{K\lambda}{B\cos\theta_B} \qquad 4.5$$

, where λ is the x-ray wavelength (in nm), K is a constant (usually assumed to be 1), B is the full-width-half-maximum (FWHM) value of the diffraction signal (in radians), and θ_B is the angle at which the peak of the signal occurs.

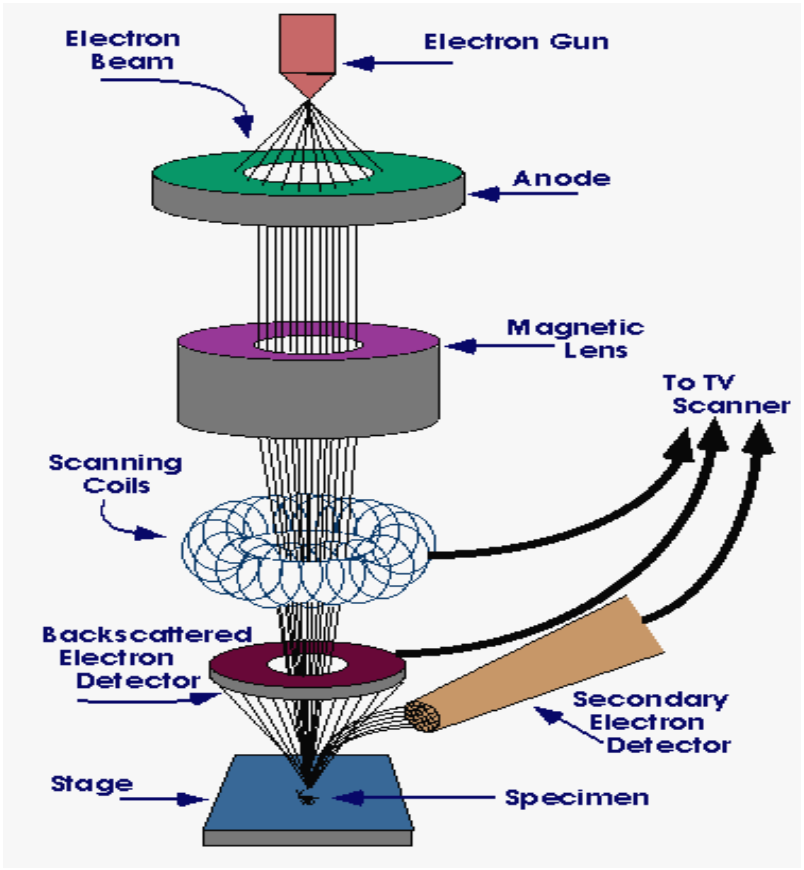

Figure 4.1 The schematic diagram and the photo of scanning electron microscopy

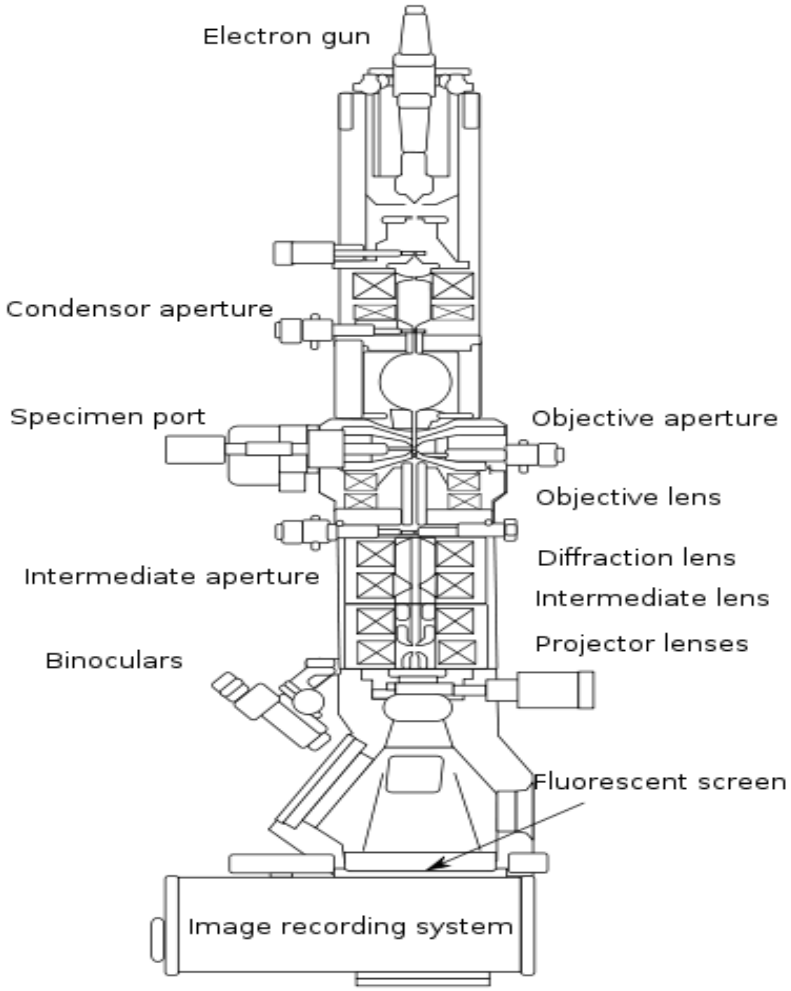

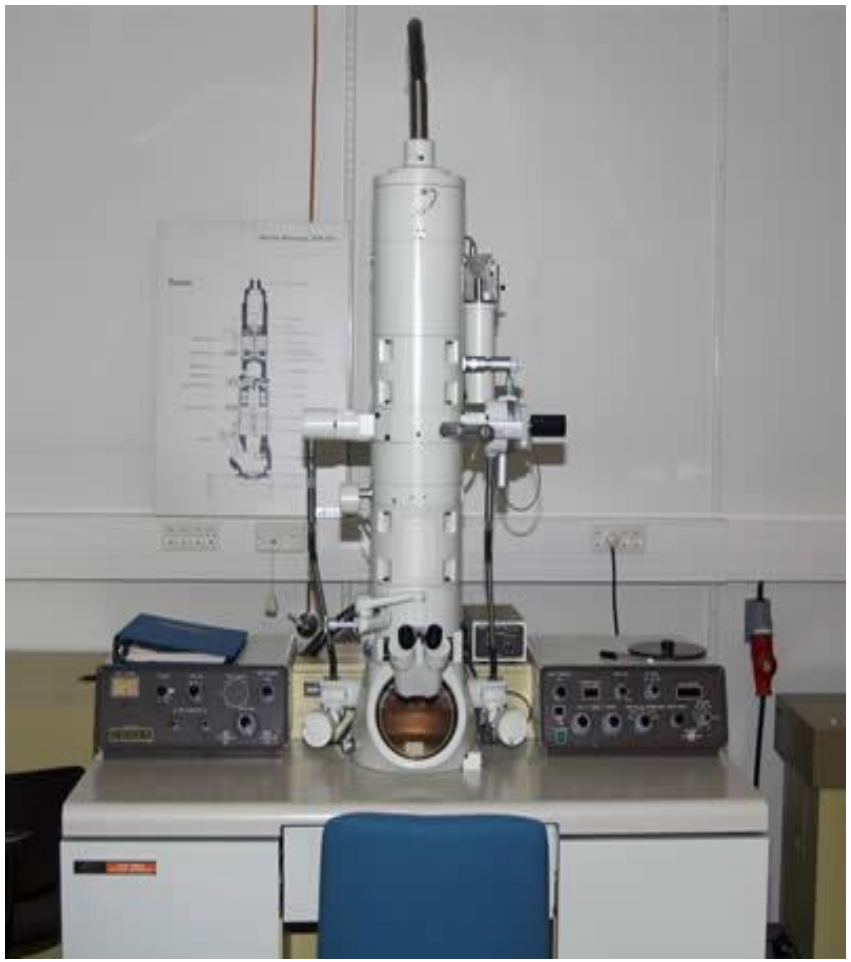

Figure 4.2 The layout of the optical components and a photo of a basic transmission electron microscope

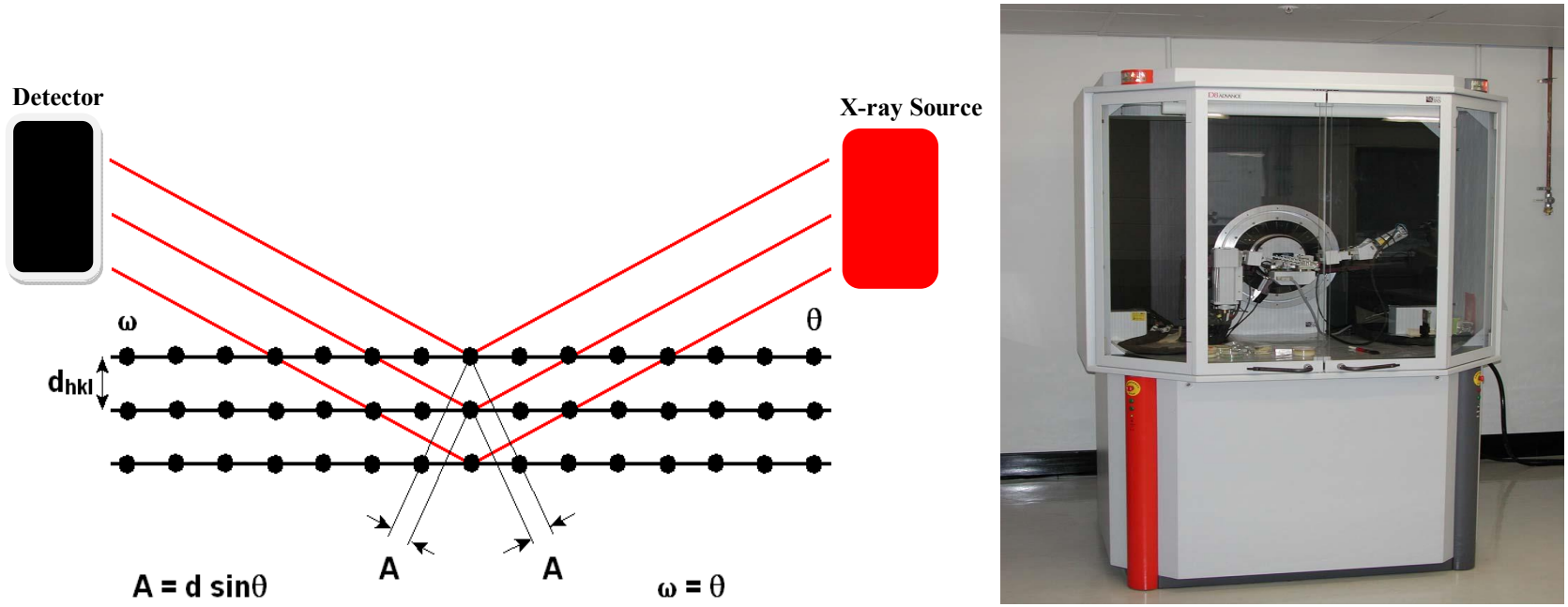

Figure 4.3 The schematic representation and the photo of x-ray diffractometer. The x-ray source produces x-ray radiation and interacts with the sample and detected on the detector.

4.1.5. Raman spectroscopy

Raman spectroscopy is used to study vibration modes in a material, via inelastic (Raman) scattering of a laser beam which interacts with phonons in the material. A Raman shift in the energy of the laser photons as a result of this interaction reduces a characteristic spectrum for a particular material. Raman and Infrared (IR) spectroscopy both measure the vibration energies of molecules but these methods rely on different selection rules. For a vibration motion to be IR active, the dipole moment of the molecule must change. Raman scattering is a powerful light scattering technique used to diagnose the internal structure of molecules and crystals by utilization of an intense and monochromatic light source (laser beam) in the visible, near infrared or near ultraviolet range. It is a complementary technique to FTIR because IR absorption only maps out the non-Raman active excitation.

Unlike the case for FTIR measurements, water does not interfere with the signal and Raman spectroscopy can measure species present in a volume less than 1 εm in diameter. Since mechanical properties, elastic properties and thermal properties also are strongly influenced by phonons, Raman spectra provide general information about the structure and properties of any material in our case is hematite. Raman scattering is the inelastic scattering of light. During a scattering event, an electron is excited from the valence energy band to the conduction energy band by absorbing a photon. The excited electron relaxes to the valence band by emitting a photon. Generally the Raman spectrum of the scattered photons (light), having energy less than that of the incident photon, is observed. By measuring the intensity of the scattered light as a function of frequency downshift (lost energy) of the scattered light, (which is plotted in Raman spectra), we obtain an accurate measure of the phonon frequencies of the material. By combining this information with the original geometrical structure of a crystal (or molecule), we can deduce the phonon dispersion relations (or normal mode frequencies). Raman scattering can be measured for phonon emission (as described above) or for phonon absorption and these two processes are called the Stokes process and anti-Stokes process, respectively.

Since Raman scattering refers to the inelastic scattering of light, not only phonons, but any elementary excitation (such as a magnon, plasmon etc.) can be involved in a scattering process in which the elementary excitation satisfies energyï momentum conservation in the scattering process [120, 121]. Therefore, Raman spectroscopy can be used to identify compounds [122]. If in the spectra, broad peaks and shift to the high wave numbers compared to the reference spectrum it would be suggesting that the sample contains very small crystal or has a high amorphous content.

Raman spectroscopy is often used to identify iron oxide phases, and the α-Fe_2O_3 spectrum is distinctly different from that of common impurity phases such as Fe_3O_4 and γ-Fe_2O_3 [123]. Raman spectrometry results presented within this research work was conducted at the Chemistry department of the Tshwane University of Technology-Pretoria, South Africa. The measurements were conducted at room temperature using Nd: YAG laser of the excitation wavelength emitting at the fundamental 1064 nm, with the germanium detector cooled with liquid nitrogen at a power of about 200 mW. The spectral resolution was about 4 cm^{-1}, with a zero filling factor of 2. To ensure a better statistical measurement, 512 averaged scans at 180 degree back scattering geometry on each sample have been conducted.

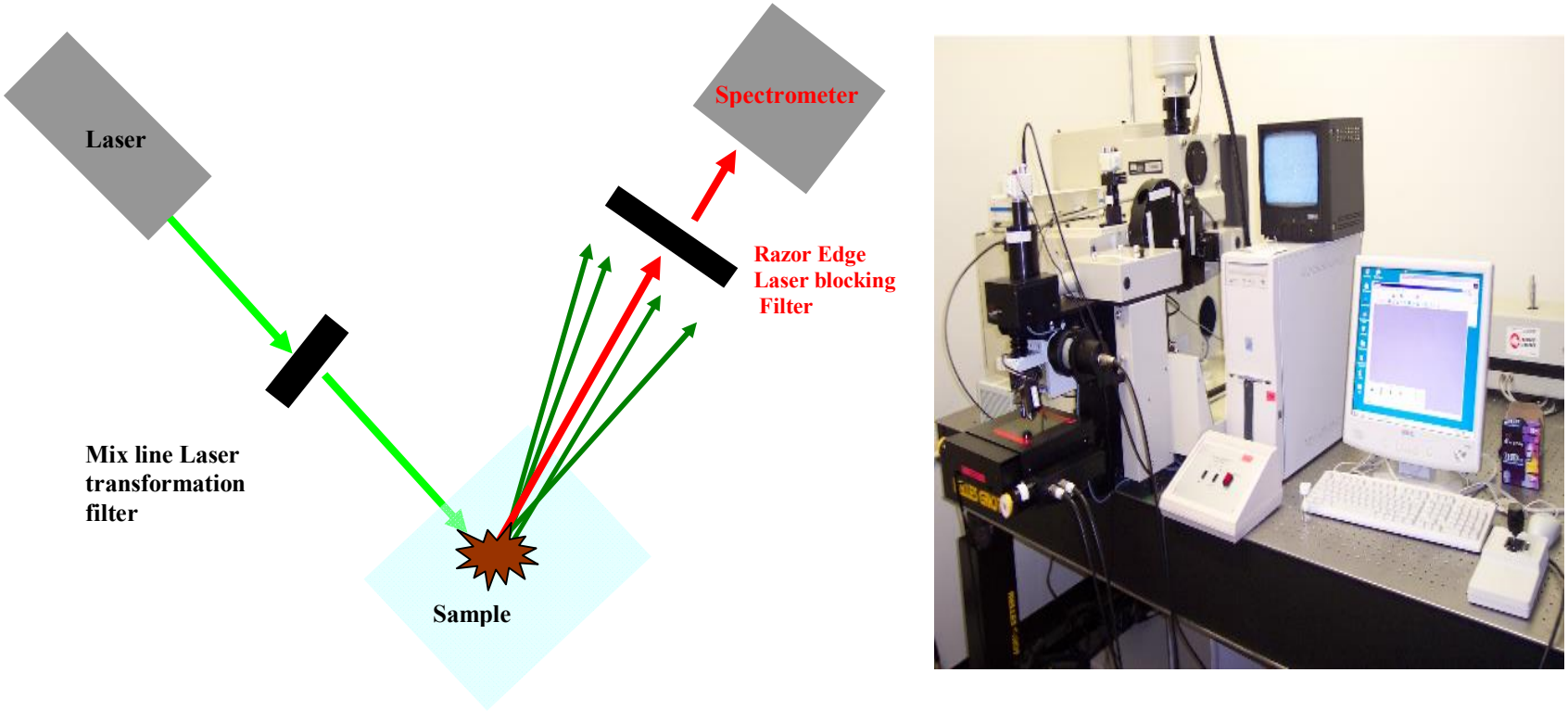

Figure 4.4 The schematic diagram and the photo of Raman spectroscope. The laser beam from the laser source interacts with the sample and the signal from the sample is the analyzed in the spectrometer.

4.1.6. Mössbauer spectroscopy

Mössbauer spectroscopy or nuclear resonance fluorescence (Mössbauer effect) spectroscopy is defined as recoilless emission of gamma rays (only low energy) and their resonant absorption by the same kind of atoms. The ^{57}Fe Mössbauer spectra are sensitive to the local environment of the iron atoms in the crystal lattice. The hyperfine parameters, isomer shift (*IS*), quadrupole splitting (*QS*), quadrupole shift (ε), and magnetic splitting (*B*) [124], provide information about the electronic density and its symmetry and also about the magnetic properties of the ^{57}Fe Mössbauer probe nucleus. Two more quantities extractable from Mössbauer spectra are directly related to lattice vibrations. One is the recoilless resonant fraction and the other the so-called temperature shift (second-order Doppler shift). Valuable information is also obtained from the widths of spectral lines, their relative intensities, and asymmetries and also from the temperature dependence of hyperfine parameters.

From the Mössbauer parameters the following information applicable to Fe_2O_3 studies can be obtained: valence state, number, and identification of nonequivalent iron positions in a crystal lattice, type of coordination of iron in its individual positions, level of ordering and stoichiometry, cation substitution, magnetic ordering, and magnetic transition temperature. Mössbauer spectroscopy provides various material properties, which are particle size (volume), microscopic magnetic properties (sub-lattice magnetization opposed to bulk magnetization) and ionic charge. It is also possible to understand the thickness of the growth along with quantitative estimates of individual products. However, these measurements are not easy due to difficulties in spectral analysis and data interpretation, the limited numbers of Mössbauer isotopes, cryogenic requirements and radiation usage.

Our experimental measurements were performed at room temperature, ^{57}Co radioactive source with a half-life $t_{1/2}$ = 245 days was used, it decay by electron capture giving off 137 KeV gamma rays to its ground state $5/2^-$ and then decay to ^{57}Fe which gives off 14.4 KeV gamma rays. The Zeeman Effect which uses selection rule that state that $\Delta m=0, \pm 1$, (see Figure 4.5) [125] therefore some transitions are forbidden and some are allowed as a result the number of Mössbauer absorption and/or transmission spectral lines are determined by the number of allowed transitions.

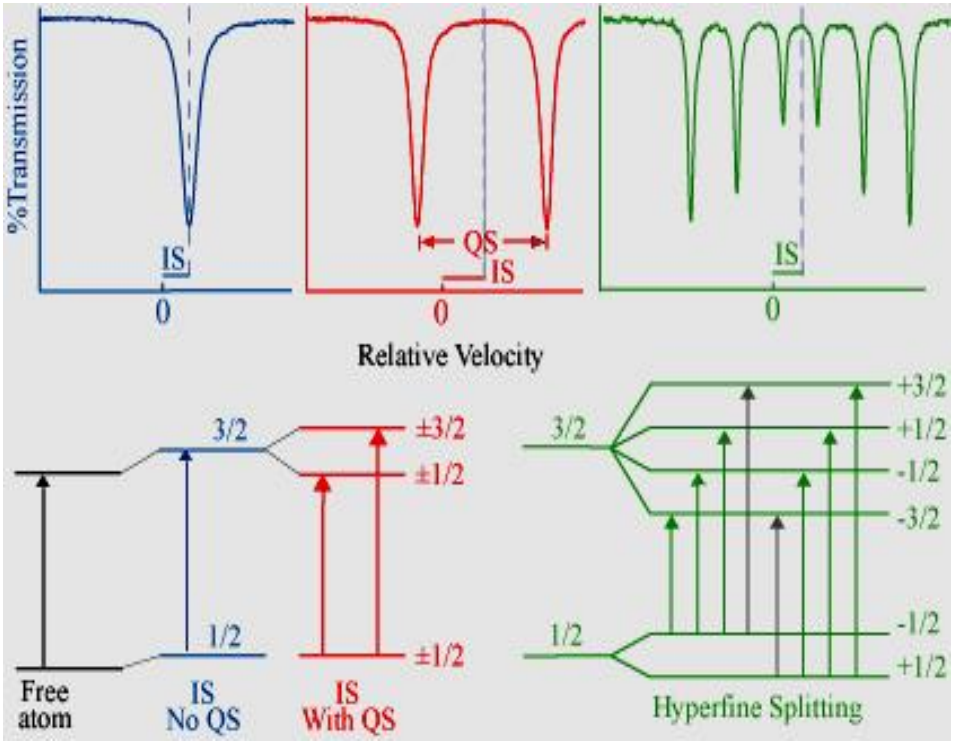

Figure 4.5 The Zeeman Effect (selection rule) indicates the origin of the Mössbauer absorption peaks for ^{57}Fe. At its simplest (blue), this appears in the transmission spectrum as a shift of the minimum away from zero velocity; this shift is generally called isomer shift (IS). The 1/2 and 3/2 labels represent the nuclear spin, or intrinsic angular moment, quantum numbers, I. Interaction of the nuclear quadrupole moment with the electric field gradient leads to splitting of the nuclear energy levels (red). For ^{57}Fe, this causes individual peaks in the transmission spectrum to split into doublets (red) having a quadrupole splitting of QS. When a magnetic field is present at the nucleus, Zeeman splitting takes place, yielding a sextet pattern (green) [125].

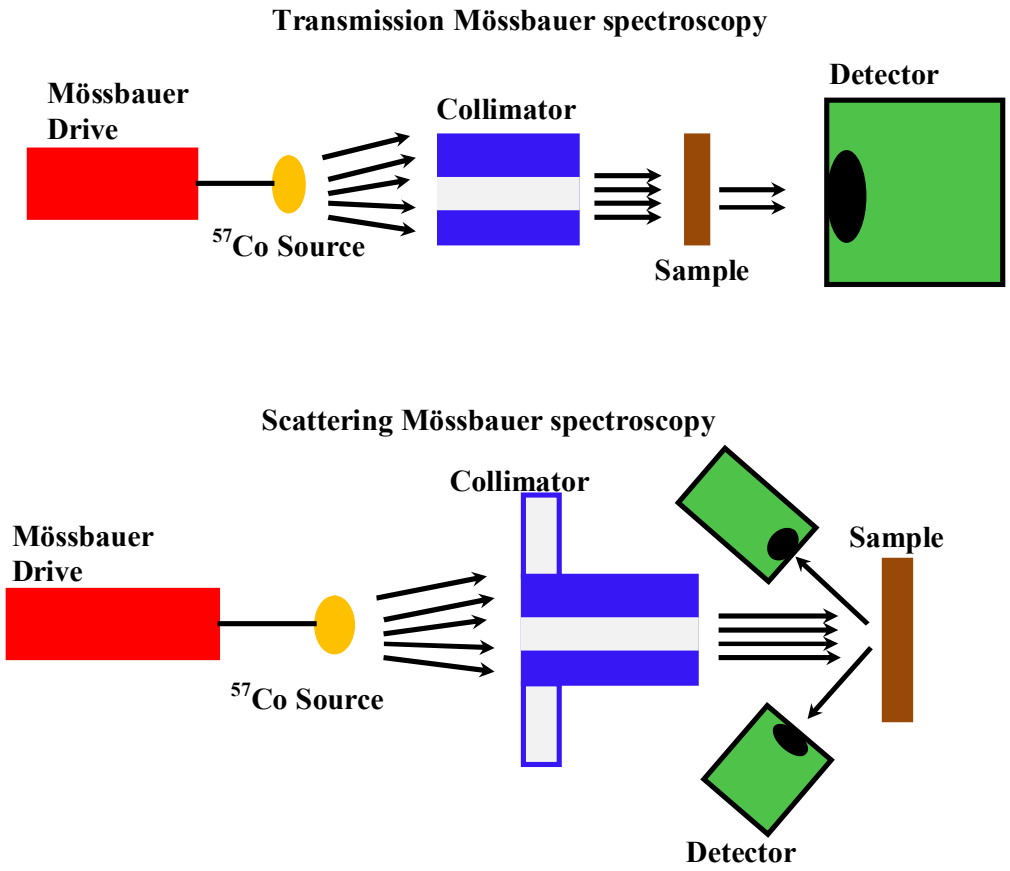

Figure 4.6 The schematic diagram of (above) transmission and (below) scattering Mössbauer spectroscopy setup for measurement adapted from ref [125].

The selection rule allows six of the eight possible transitions in the case of ^{57}Fe isotope. There are two methods that can be employed during Mössbauer analysis and are shown in Figure 4.6, which are the transmission Mössbauer, where powders can be used and the scattering Mössbauer where thin films is used. It does not need any special sample preparation. A single spectrum provides three Mössbauer parameters which are distinctly different for the oxides, oxyhydroxides and hydroxides of iron oxides. The only interference comes from iron species. Several specific materials properties can be measured, which include particle size, microscopic magnetic properties and ionic charge.

4.1.7. Gas Sensing

The chemiresistive is when gas experiences a change of resistance when exposed to target gas. During this process the change in the resistance induced by the interaction of the gas and the sensor is considered as one of the most important characteristics for the gas sensor. At equilibrium state in a gas sensor the sensitivity of the gas sensor is defined as the ratio of the resistance in air to the resistance after subjected to the analyte gas. The calculation of the sensitivity differs with the type of semiconductor. The sensitivity for the n-type semiconductor is given in the following:

$$S = \frac{R_{air}}{R_{gas}} \text{ , for n-type semiconductor} \qquad 4.6$$

While the one for the p-type semiconductor is given as:

$$S = \frac{R_{gas}}{R_{air}} \qquad 4.7$$

The percentage is calculated as: $S(\%) = \left(\frac{R_{air} - R_{gas}}{R_{air}} \right) \times 100$, for n-type semiconductor 4.8

R_{air} is the resistance of the gas sensor before passing the gas and R_{gas} is that after passing the gas and reaching the saturation value [126]. It is well known that the fundamental sensing mechanism of semiconductor based gas sensors relies on a change in electrical conductivity due to the

interaction between the surface complexes such as O^{-}, O_2^{-}, reactive chemical species (OH^{-}), and gas molecules to be detected.

Therefore the stability in the gas sensor is very important because gas sensors should operate consistently under repeated condition, experiencing response and recovery by detecting the gas at various concentrations and sometimes in the extremely harsh environments. Stabile performance without showing a drift is another important measure to evaluate the performance of the gas sensor. It is very important to note the response and the recovery time. The response time is defined as the time taken to reach 90% of the saturation value of the resistance and the recovery time is defined as the time taken to drop to 10% of the saturation value of the resistance when the gas sensor is placed in the clean environment or air. The smaller the response and the recovery time mean that the gas sensorôs performance is high or good. The setup of the gas sensing shown in Figure 4.7 and Figure 4.8 was used for the analysis of the samples in this work.

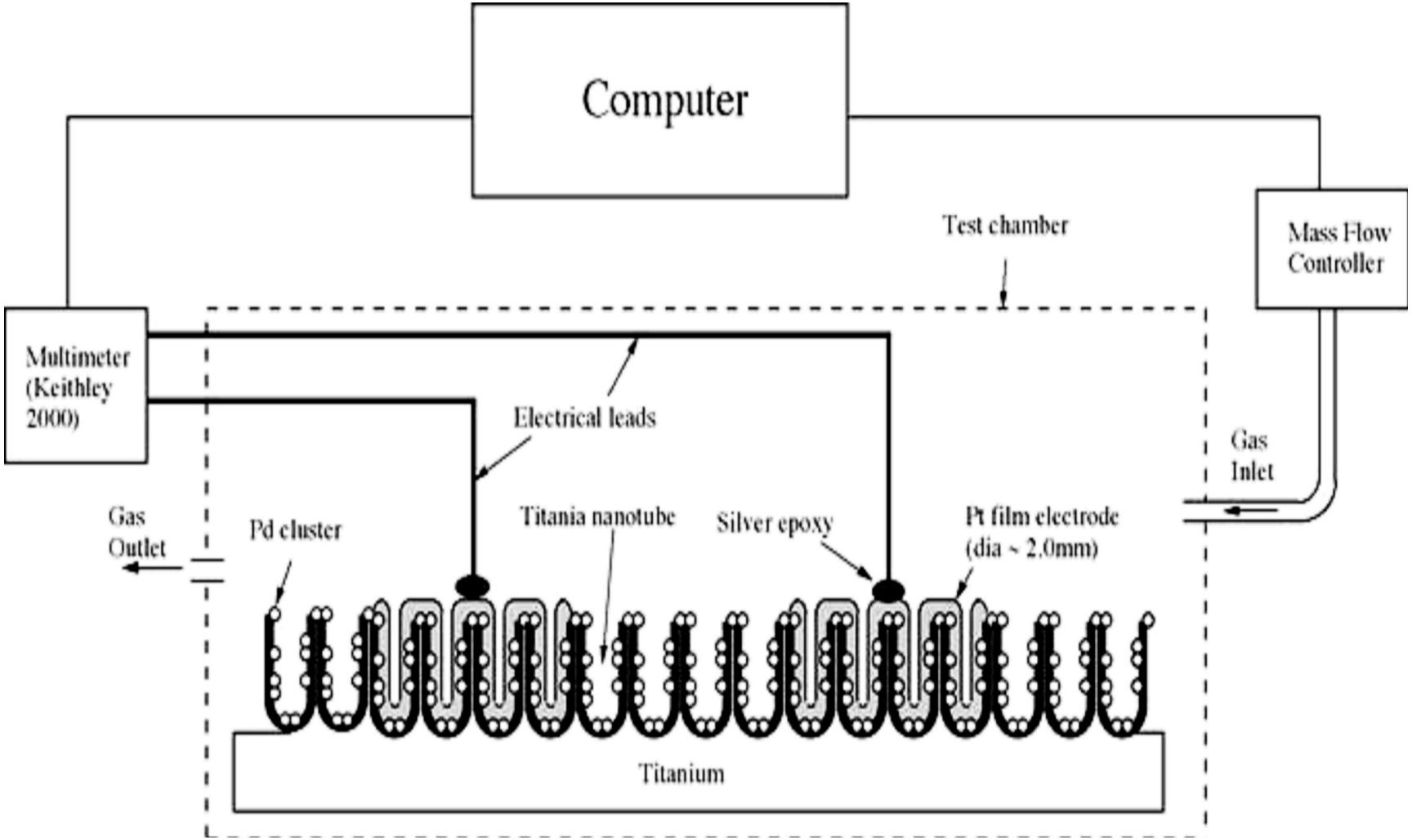

Figure 4.7 Schematic diagram of a typical setup for gas-sensing experiments

Figure 4.8 The photograph of the gas sensing experimental setup showing the gas sensing chamber, gas regulators a multimeter coupled to a computer.

CHAPTER V

5. EXPERIMENTAL RESULTS AND DISCUSSION

5.1. Sample Preparation

Hematite (Ŭ-Fe_2O_3) nanostructured thin films were synthesized on fluorine doped tin oxide (FTO) conducting glass substrate using ACG method in a regular laboratory oven. Substrates such as silicon wafers and corning glass were also used during the deposition. FTO substrate is useful for scanning electron microscopy and for optical measurement as it is a translucent conducting substrate and is chemically stability. Substrates are cut to fit in the 100 mL autoclave bottle, which was used during the deposition. Before deposition, it is very important to clean the substrates. The cleaning of the substrates was done in the ultrasound bath using the following chemicals in the following sequence: first washed with methanol, followed acetone and subsequently trichloroethylene and acetone, methanol, deionized water and lastly the substrates were immersed in the solution with pH the same as the one that will be used during deposition. After cleaning the substrates were dried in the laboratory oven at 95^{o}C.

5.2. Experimental procedure

The deposition of nanostructured hematite samples was undertaken using the aqueous chemical growth. The chemical were purchased at Industrial analytical Ltd and they were of pure quality as indicated to be 99.99%. The following precursorôs concentrations were used during the synthesis, 0.1 M of anhydrous ferric chloride ($FeCl_3$) and 1 M of sodium nitrate ($NaNO_3$) and for doping different concentration of ruthenium chloride ($RuCl_3$. xH_2O) was used.

The pH was set using concentrated hydrochloric acid (37%) drop by drop and the pH meter was used to measure the pH. All precursors were highly soluble in water and to quickly dissolve the salts, the method of shaking a bottle by hand was used. After all precursors were dissolved the substrates were immersed and the bottles were quickly taken in to the laboratory oven.

The deposition temperature was set to 95^{o}C. This method allowed the growth of these nanomaterials at different times. After each deposition time, the samples were washed to remove all the residual salt with deionized water and dried in the oven at 95^{o}C. FTO cannot be heated above 550^{o}C due to the possible degradation of the conducting layer at this temperature. However the samples were heat treaded at 500^{o}C for 1h in air to obtain the alpha phase of iron oxide.

Hematite photoelectrodes requires external bias when used for water splitting application due to the band edge therefore the fabrication of a well suited photoelectrode for this application requires a dopant. The doping was performed to optimize the absorption of the samples in the visible region of the solar spectrum. It was decided to use ruthenium salt as a dopant because ruthenium oxide has a high electrocatalytic activity and very good thermal and chemical stability and it represents one of the best materials for supercapacitors [110].

5.3. Samples Colours

The colour of the samples before annealing were yellowish, which was the indication of the existence of the natural occurring iron oxide material called akaganeite (β-FeOOH) as described by Vayssieres et al (2001) [84] and after heat treatment at 500^{0}C, the colour changed to reddish, which indicates the presence of α-Fe_2O_3 phase on the glass substrate and was confirmed in the x-ray diffraction analysis. This means that different phase have different colour. By reducing the particle size to nano scale, transparent iron oxide pigments can be obtained.

Manufacturing process of transparent iron oxide pigments depend on the control of physical and surface chemistry properties. Particle size is optimized to minimize light interference that may occur therefore maximizing transparency. In general particle size from 2 to 10 nm increases transparency 3-10 time when compared to the bulk form [127]. Recently such transparent iron oxide pigments are preferably used. These have good stability to temperature, the red pigment can resist up to 300^{0} C while the yellow pigment , black pigment, green and brown pigments can withstand up to 160 ^{0}C.

Wang et al (2005) [128] reported that hematite changes color depending on size, shape and synthesis condition such as doping. This was reported to be due to both quantum size effects and shape dependent reflectance [11]. For very small particles and ultrathin films, also the choice of substrate is important and effects the possible iron oxide phases that can be formed [55].

5.4. The growth of undoped hematite nanostructures

5.4.1. Structural properties

The XRD peak patterns of as grown iron oxide samples deposited at different times are shown in Figure 5.1. The XRD patterns of all samples are of hematite (α-Fe_2O_3) which is rhombohedral with the R-3C space-group structure and the lattice parameter a=0.50356 nm, c=1.37489 nm and z=6, according to JCP2. CAT: No. 73-0603. The five strong peaks, namely, (012), (104), (110), (116) and (300) are the reflections of α-Fe_2O_3 (hematite). The presence of the other minor peaks such as (006), (113), (024), (122), (018), and (214) provides further evidence for the existence of hematite polycrystalline.

There are two pronounced XRD peaks named with γ which are the signature of maghemite (γ-Fe_2O_3) contamination in our sample as indicated in Figure 5.1. Beside the contamination of maghemite, the results are still in good agreement with the literature reported by Tahir et al (2009) [129] on the α-Fe_2O_3 grown by CVD method, and Glasscock et al (2006) [21] on iron oxide nanostructures grow using ACG method. Vayssieres et al (2005) also reported the XRD patterns of α-Fe_2O_3 grown using the ACG method, which are also in good agreement with our results without the presences of the peak from the contamination. The higher intensity of the (104) peak indicates that the α-Fe_2O_3 particles are textured along the (104) direction. The presence of a number of strong diffraction patterns of hematite in the XRD data as illustrated in Figure 5.1 confirms that the deposited samples are highly polycrystalline.

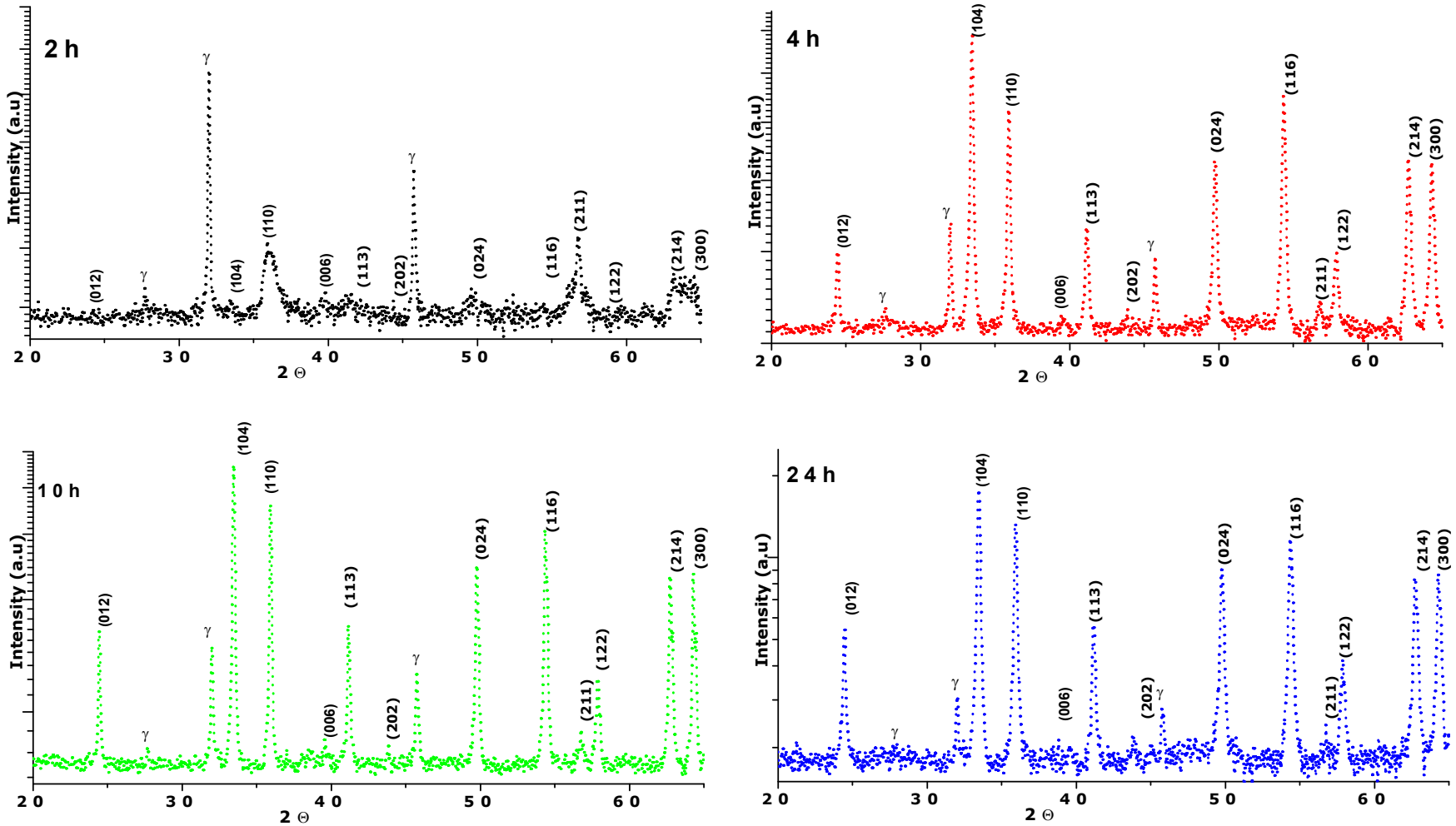

Figure 5.1 XRD patterns of α-Fe_2O_3 powder samples collected from the bottom of the autoclave bottle after each deposition time.

5.4.2. Morphology of undoped hematite nanostructures

The SEM images of hematite nanostructures grown at different deposition time ranging from 2h, to 24h on FTO substrate are presented in Figure 5.2. In all samples, the full substrate coverage was obtained and the nanorods were strongly adhered onto the substrate. The orientation of hematite nanorods in all images for 2h ï 24h are randomly parallel onto the substrate. This is due to the fast appearance of a large number of nuclei that result in the fast growth of 3D anisotropic nanorods that are parallel to the substrate.

The size of the nanorods increases with the increase in the deposition time is increasing. The surfaces of the films are consisting of small needle-like nanostructures. The lengths of needles increase from 300 nm to a maximum of 800 nm with the deposition time. Their diameters range from 30 nm to 80 nm with the increased in the deposition time. Each needle-like nanostructure is a result of the incorporation and agglomeration of~5-10 nm individual particles. Guo et al (2007) [130] and Vayssieres et al (2004) [110] have reported the same phenomena. Individual needles are fused together and create the formation of an interconnected 3D network with electronic connections and this would facilitate the photo-induced charge transport. The nanostructured α-Fe_2O_3 electrodes of this nature contain unique physical and chemical properties that are essential for photoelectrochemical water splitting devices. The formation of needle like nanostructures by interconnecting with adjacent individual particles provides a large surface area which is beneficial for light-induced charge transfer at the surface of α-Fe_2O_3.

The TEM images of the iron oxide nanoparticles are rod-like as seen in Figure 5.3. The samples were ultrosonicated in acetone before putting the drop on the copper grid. The particles seem to have a large tendency of agglomeration, which may be due to the magnetic interaction between particles. It is clear that bigger rods in the nanoscale region are an agglomeration of very small rods. These small rods which can be seen in all the images are called ultrafine [130] nanorods with the diameter of about 5 ï 12 nm. The shapes of the nanostructures are rod-likes and their sizes depend on the deposition time.

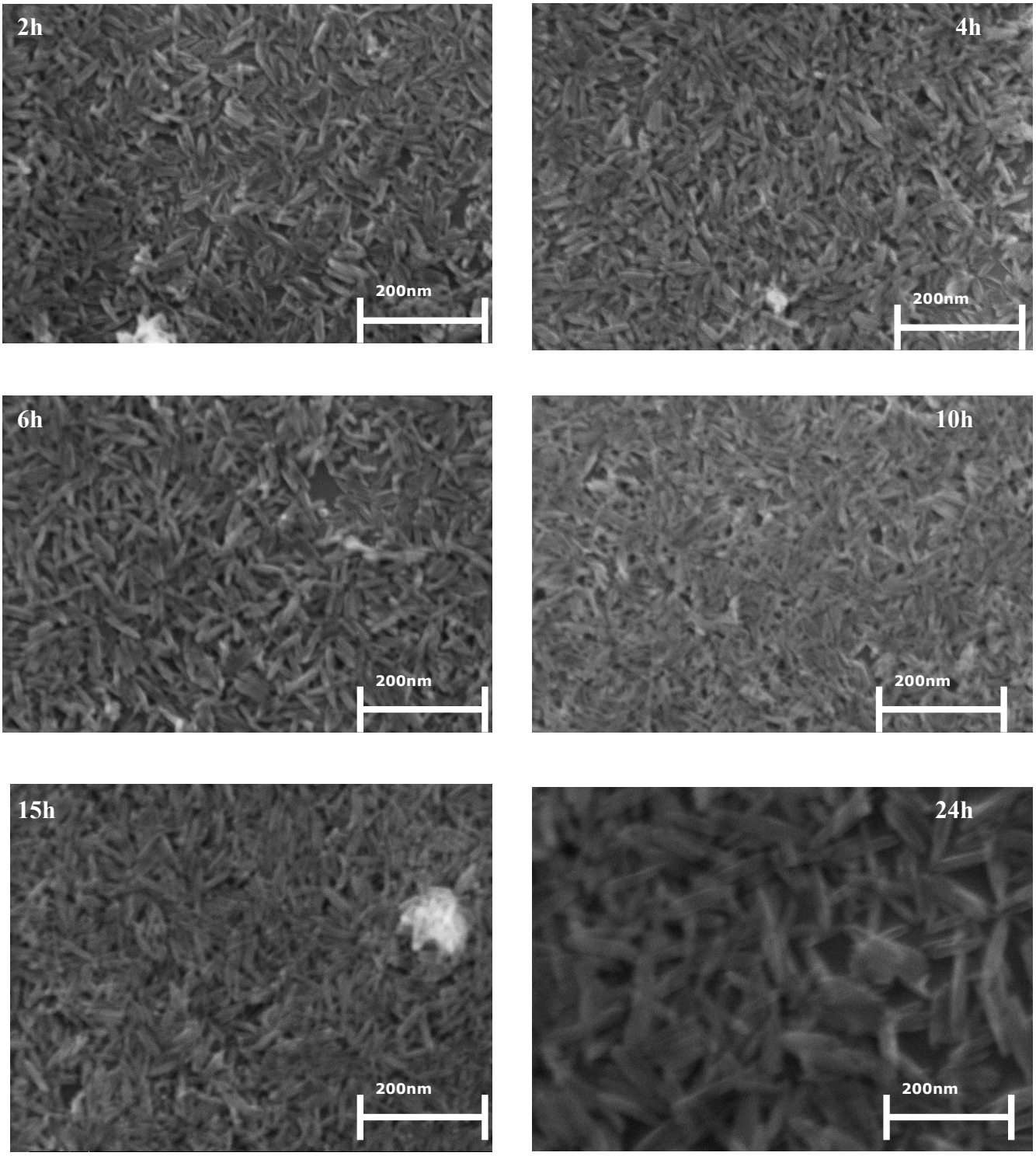

Figure 5.2 The SEM images of hematite nanorods grown on FTO substrate at different aging time at 95^{o}C.

Attempts have been made to obtain information regarding the growth mechanisms of α-Fe_2O_3 based on the time evolution of the average diameter and length of the nanorods. In Figure 5.4 and Figure 5.6 the growth mechanism as a function of deposition time of the rod likes nanostructureôs diameter and length of α-Fe_2O_3 are shown respectively. In the literature it has been reported that, if the diffusion-limited Ostwald ripening according to the Lifshitzï Slyozovï Wagner (LSW) theory [131, 132] is to be the only contributor of the growth mechanism, then the rate law would be given by $p^3 - p_0^3 = kt$ where p is the average growing parameter (which is the diameter or the length in our case) at time t and p_0 is the average initial parameter of particles and k is the rate constant which is given by $K=8\ \gamma\ DV_m^2C_Đ/\ (9RT)$, where D is the diffusion constant at the temperature T, V_m the molar volume, γ is the surface energy and $C_Đ$ the equilibrium concentration at the flat surface.

We have tried to fit the data of the nanorods diameter and length obtained from SEM to the diffusion-limited Ostwald ripening growth mechanism. The fits are reasonably good with the correlation of $R^2 = 0.99$ and $R^2 = 0.96$ for the diameter and the length of the nanorods of α-Fe_2O_3 respectively. At the initial stage the nucleation starts and the particles orientate themselves to form ultrafine nanorods via oriented arrangement growth mechanism. Moreover the theoretical data fit is in good agreement with the experimental data which suggest that both the length and the diameter grow via the diffusion-limited Ostwald ripening growth mechanism where these ultrafine rods agglomerates and form bigger rods in both diameter and length.

Figure 5.5 shows the particles diameter size distribution while Figure 5.7 shows the particle length size distribution of α-Fe_2O_3 nanorods grown at a given time. These results are in a good agreement with the results of the effect of the aging time on the average diameter and length of α-Fe_2O_3. This is manifested by a shift in particle size distribution owing to the disappearance of the smaller particles diameter and length and the formation of larger and longer ones with an increase in deposition time.

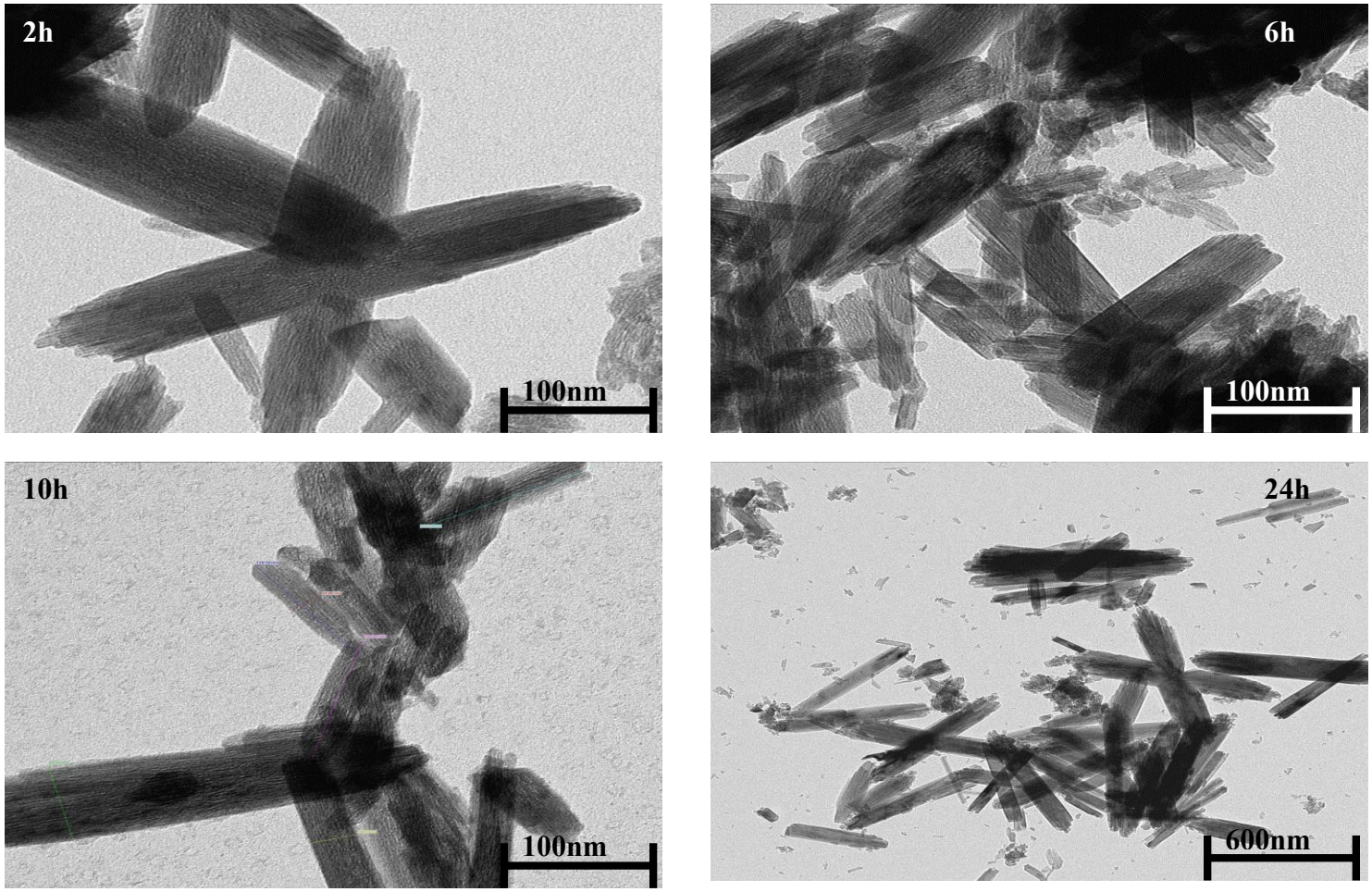

Figure 5.3 The TEM images of α-Fe_2O_3 nanorods grown at different deposition times.

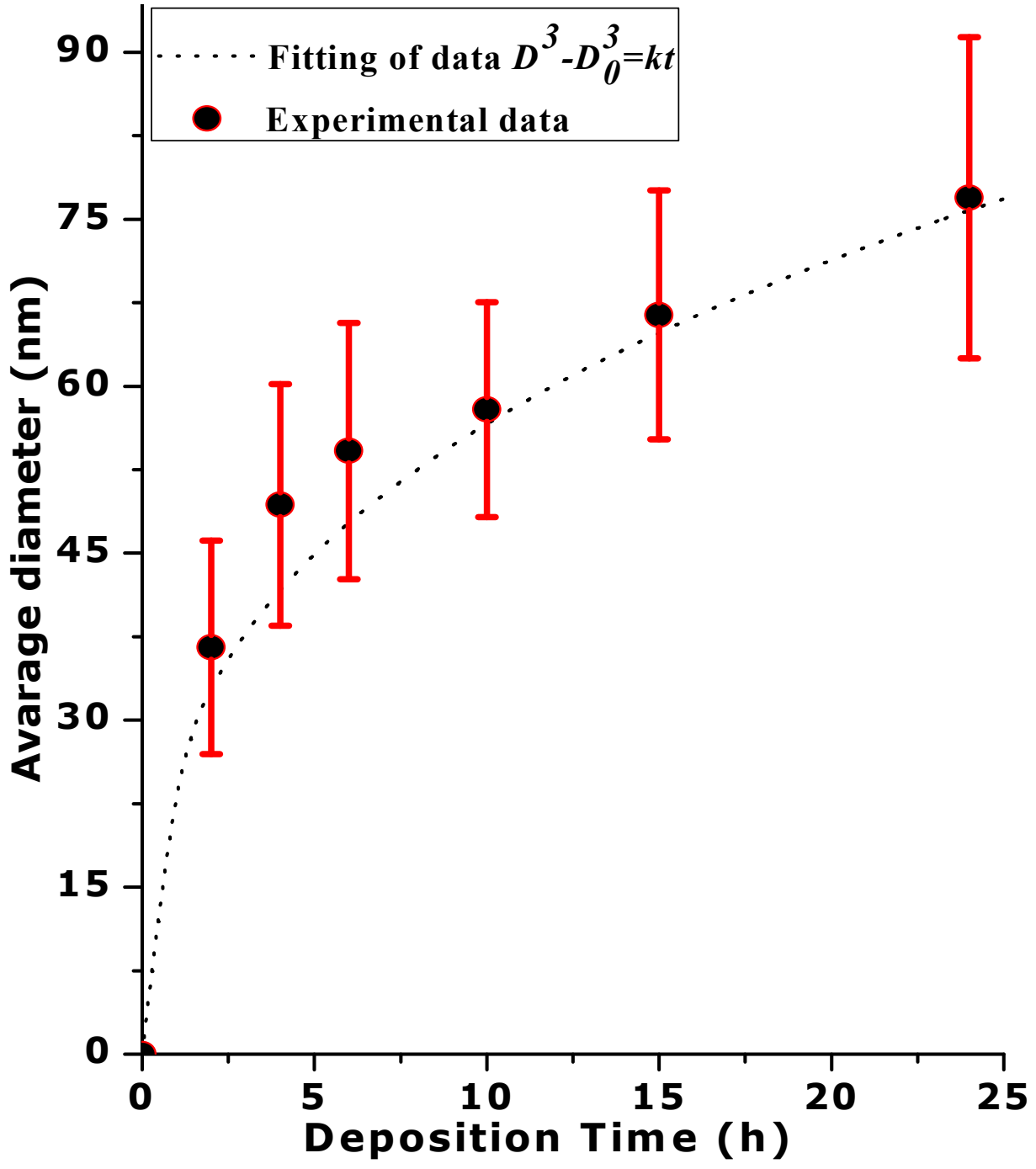

Figure 5.4 The effect of deposition times (h) on the average diameter of the α-Fe_2O_3 nanorods. The dotted line is the D^3 fit and the dots represent the experimental data and he calculated error.

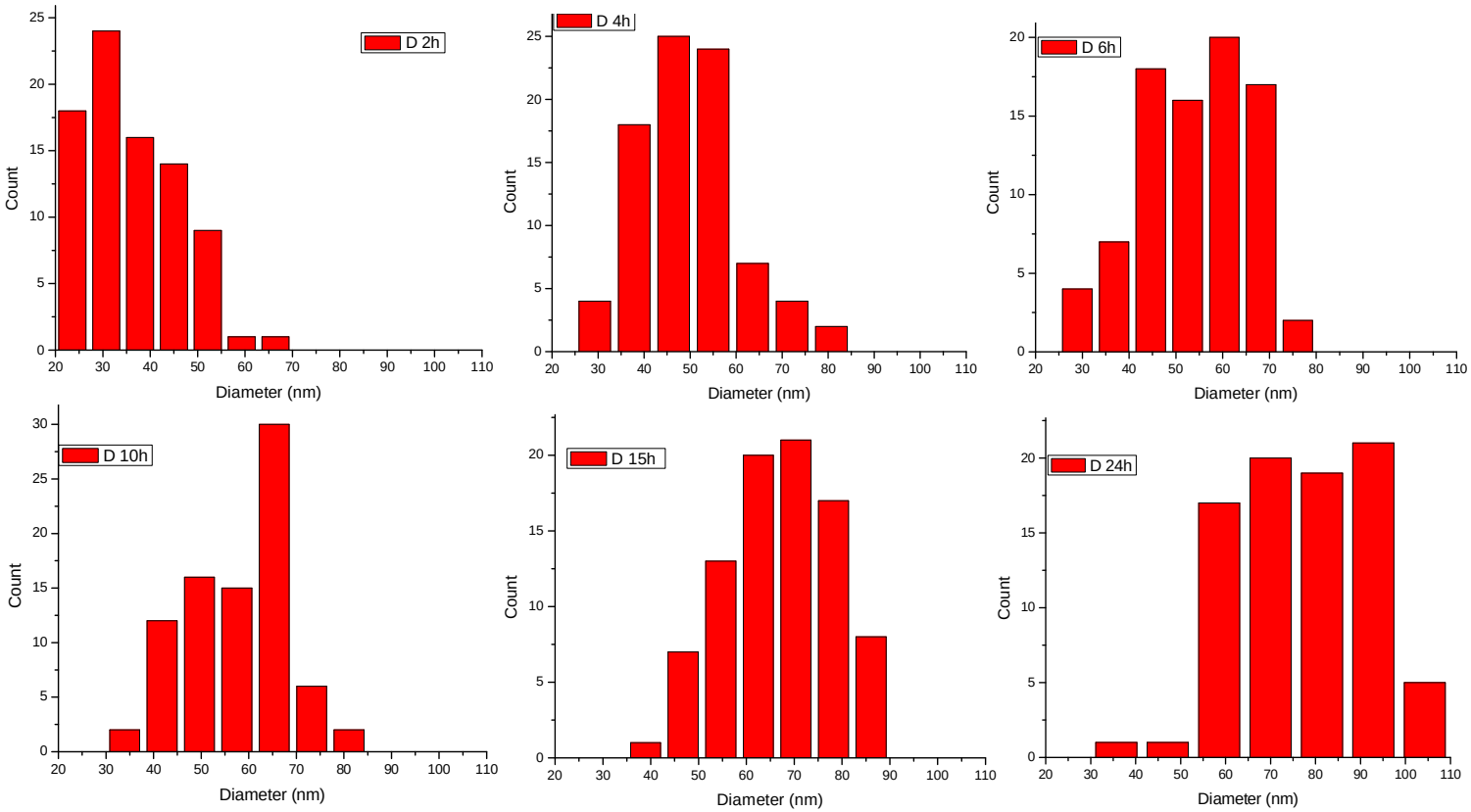

Figure 5.5 Particle diameter size distribution for deposition different times.

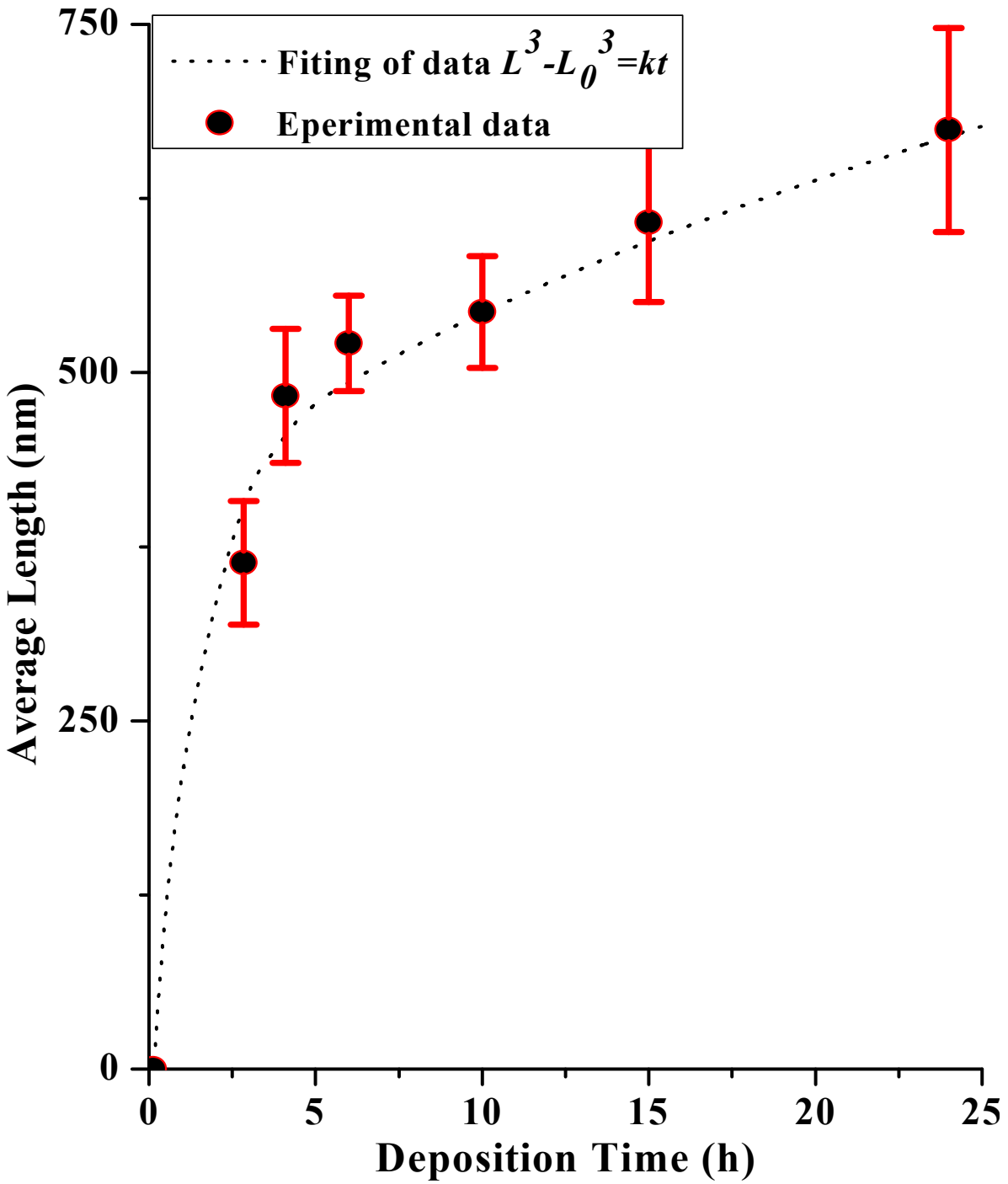

Figure 5.6 The effect of deposition times on length of α-Fe_2O_3 nanorods. The dotted line is the L^3 fit and the dots represent the experimental data and calculated error.

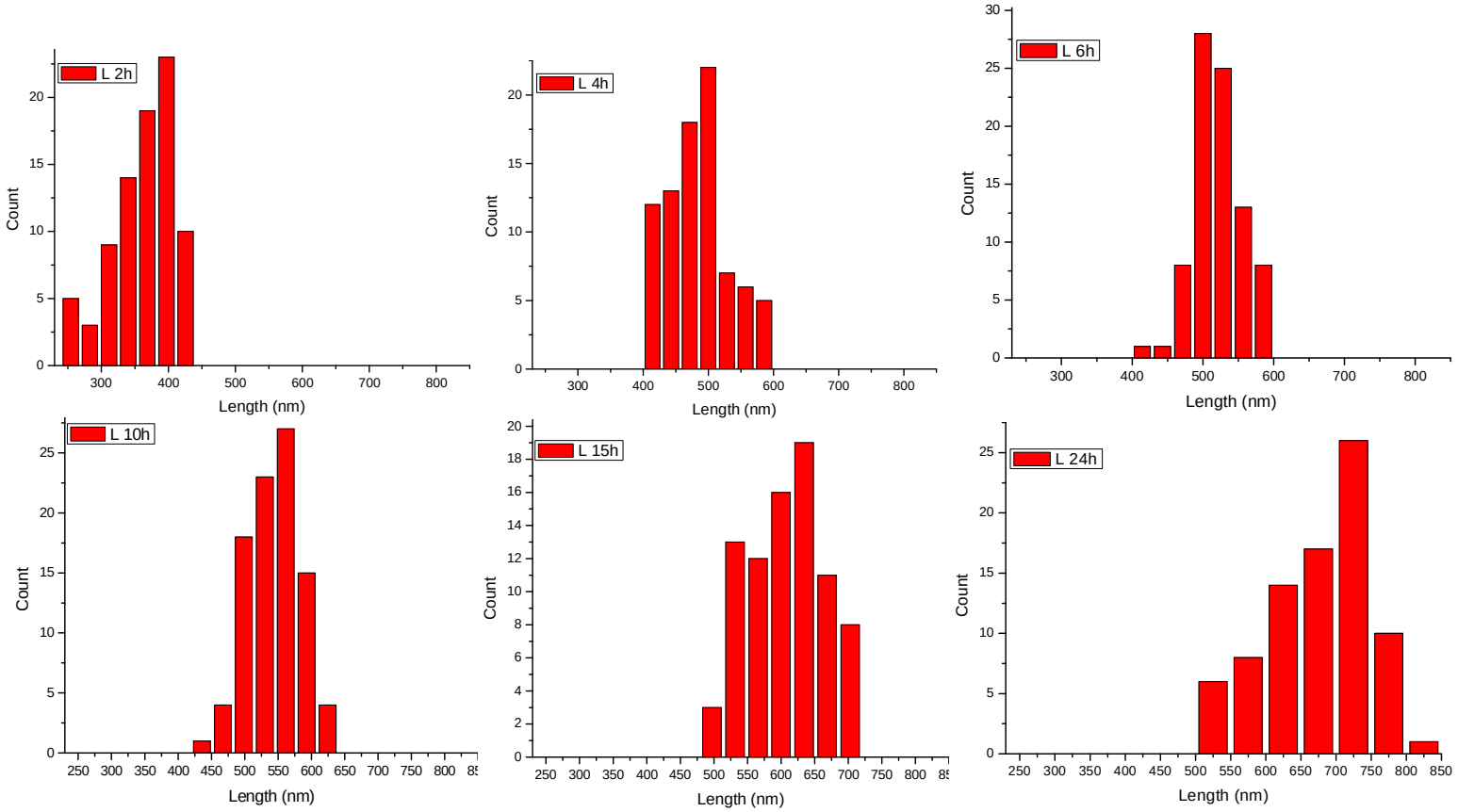

Figure 5.7 Particle length size distribution for different deposition times.

5.4.3. Raman analysis on undoped hematite nanorods

The Raman spectra of the α-Fe_2O_3 films deposited at different times (2, 4, 10 and 24 h) on FTO coated glass substrate are shown in Figure 5.8. The spectra are typical of α-Fe_2O_3 phase. The Raman bands at 219 and 496 cm^{-1} can be assigned to the A_{1g} vibrational mode, while the ones at 243, 288, 408, and 608 cm^{-1} belong to E_g vibrational mode and the band centered at 1312 cm^{-1} is from the 2Eu vibrational mode. The bands appearing between 920 and 1200 cm^{-1} wavenumbers, are due to the substrate contribution.

The Raman bands observed in our results are slightly shifted towards small wavenumbers from the reported Raman bands of α-Fe_2O_3 grown by CVD method by Tahir et al (2009) [129]. This shifting may be due to the synthesis procedure. The Raman bands of all our samples matched well with the previously reported Raman data for hematite prepared by chemical route [18].

The forbidden Raman mode around 660 cm^{-1} observed in our hematite spectra has been reported by a number of studies who describe it as attributed to a large amount of defects, which would lead to a significant lattice distortion, as an evidence for the space-symmetry reduction [133,134 135]. However Sartoretti et al (2005) [136] have assign this vibrational mode to Fe_3O_4. Our XRD study shows no reflection from Fe_3O_4, so the presence of this mode is a signature that our samples are not defects free. Hematite Raman modes reported by Beattie et al (1970) [137], Massey et al (1990) [138] and Shim et al (2001) [139]] in the literature are compared with our study in Table 5.1.

The allowed phonon bands occurs below 620 cm^{-1} with an additional large band at about 1320 cm^{-1} which is attributed to the two-magnon scattering [140] but subsequently interpreted as an overtone of a forbidden 660 cm^{-1} (odd symmetry IR-active phonon), probably activated by disorder [141] and this is observed in our study as demonstrated in Figure 5.8.

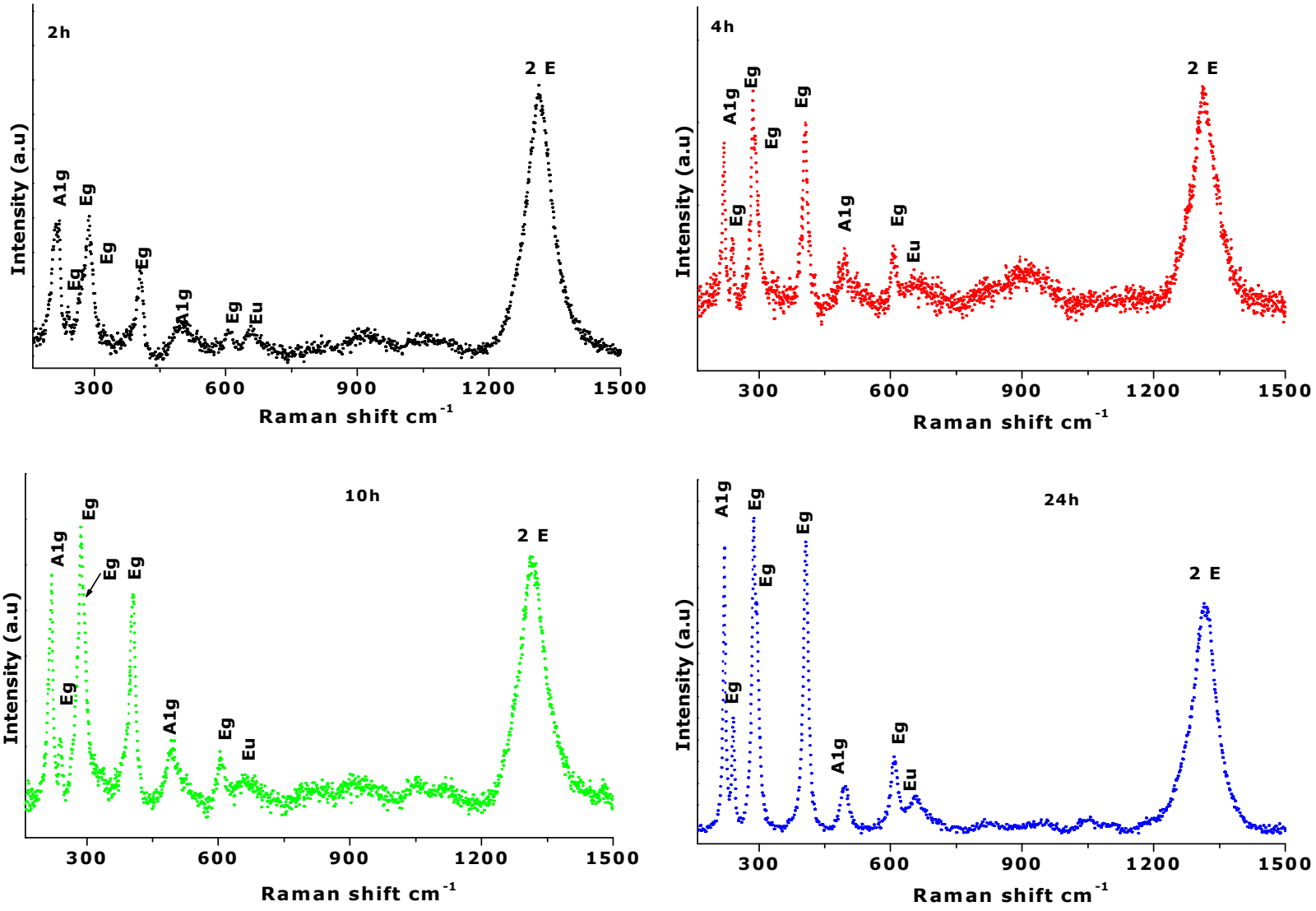

Figure 5.8 The Raman shifts of hematite (α-Fe_2O_3) nanorods grown on FTO glass substrate at different aging time at 95^{o}C.

Table 5.1 The Raman vibrational peaks position in cm^{-1} of hematite nanorods on FTO glass substrate grown at different aging time as indicated in the Table compared with the vibrational modes positions reported in the literature.

Vibrational Mode	**Beattie et al (1970)[137]**	**Massey et al (1990)[138]**	**Shim et al (2001)[139]**	**2h**	**4h**	**10h**	**24h**
$\mathbf{A_{1g}(1)}$	226	228	224	219.6	219.1	219.1	221.1
$\mathbf{E_g(1)}$	245	246	243	240.0	238.4	237.9	241.0
$\mathbf{E_g(1)}$	293	294	290	288.3	285.3	286.3	287.8
$\mathbf{E_g(1)}$	298	300	297	297.0	290.4	294.4	293.9
$\mathbf{E_g(1)}$	413	412	408	404.4	405.9	403.9	405.4
$\mathbf{A_{1g}(2)}$	500	496	496	490.4	494.5	498.5	490.4
$\mathbf{E_g(1)}$	612	614	609	602.4	604.4	603.4	608.0
$\mathbf{E_u}$	-	-	659	651.2	653.3	677.2	657.3
$\mathbf{2E_u}$	-	1320	1316	1312.9	1311.4	1310.9	1322.1

5.4.4. FT-IR analysis on undoped hematite nanorods

Figure 5.9 present the FTIR spectra of α-Fe_2O_3 samples deposited for 10 h and 24 h. The 10 h sample exhibited pronounced IR active modes with the absorption bands at 330 cm^{-1},394 cm^{-1} 475 cm^{-1}, 553 cm^{-1}, 630, 714 cm^{-1} and 874 cm^{-1}. The 24 h sample exhibited the same absorption bands but with weaker intensities which are due to the difference in thickness in both samples.

All the vibrational modes are assigned to hematite. The vibrational modes reported by Sahoo et al (2010)[142] at 555 cm^{-1} and 463 cm^{-1} and in our sample they appear at 475 cm^{-1} and 553 cm^{-1} for 10 h while they appear at 471, 536 cm^{-1} for 24 h, which are due to the Fe-O stretching and bending vibration mode, respectively of γ-Fe_2O_3 and for α-Fe_2O_3. Zhao et al (2007) [143] reported the same bands at wavenumbers of 538 cm^{-1} and 466 cm^{-1}, therefore correlating the FTIR results with the XRD investigation, the mode at 471cm^{-1} and 475 cm^{-1} which are present in the sample prepared respectively for 24 h and 10 h can be assigned to the Fe-O stretching mode of γ-Fe_2O_3.

Different synthesis procedure may exhibit different IR absorption bands position[144], and Sidhu et al (1988) [145] observed that by heating maghemite to 500^oC for 3 h to produced sintered aggregates of hematite having only two major infrared (IR) bands, at 550 cm^{-1} and 480 $cm^{-1}$and Fischer et al (1975) [146] observed only three IR bands, at 557, 465, and 325 cm^{-1}, for ellipsoidal hematite formed by the aqueous incubation at 70^oC of Ferrihydrite at pH 6-7 in the presence of oxalate. Rendon et al (1981) [147] found that hematite formed by the thermal transformation of goethite at 300^oC gave IR bands at 650, 525, 440, and 300 cm^{-1}, while hematite formed by heating goethite at 600 ^oC gave an additional band at 400 cm^{-1}. Serna et al. (1987) [148], used classical theory of absorption of IR radiation by small particles and concluded that the differences in IR bands of hematite were largely dependent on particle morphology.

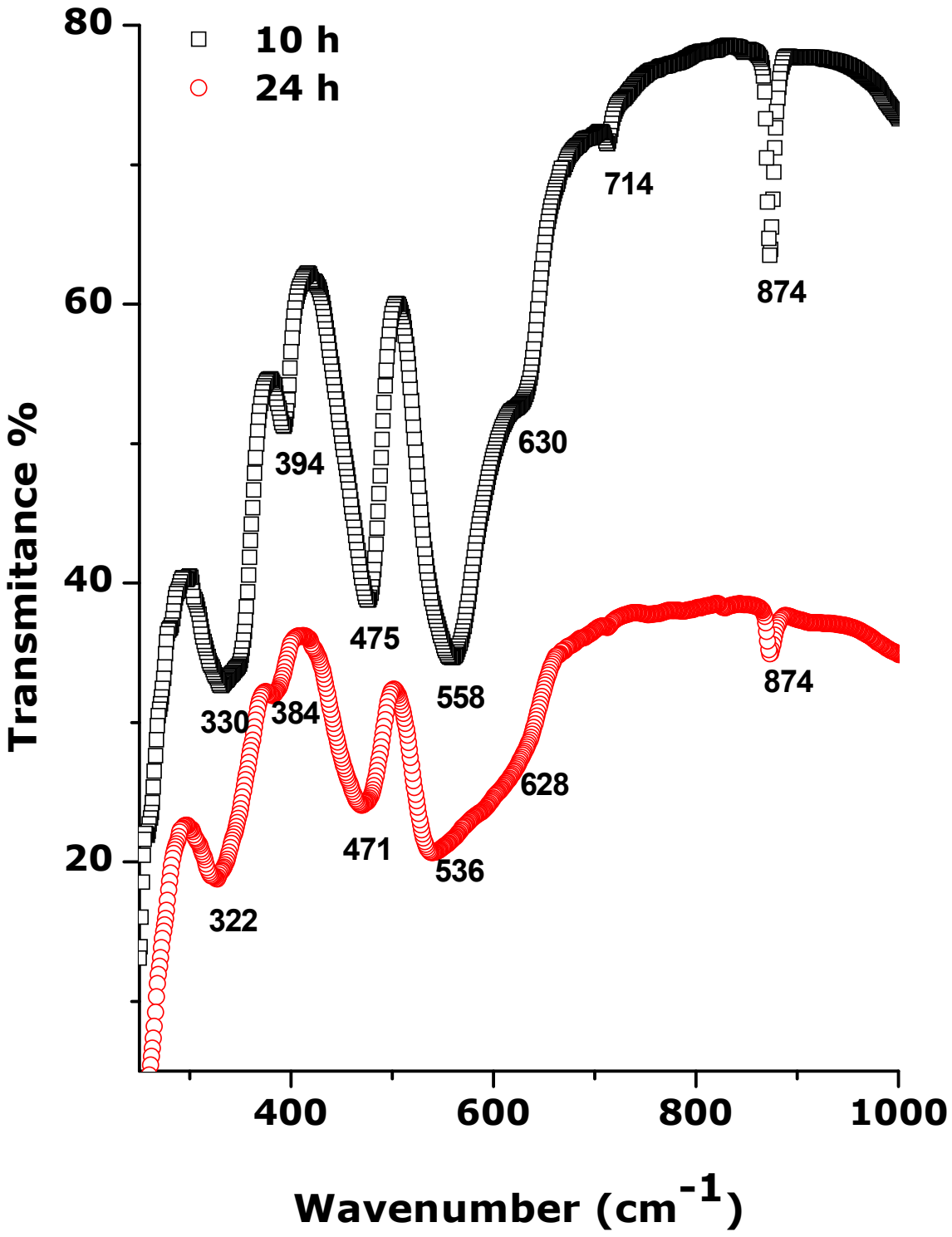

Figure 5.9 The FTIR signals of the undoped hematite powder samples grown for 10 and 24 h. KBr was used to make a pallet for the analysis.

5.4.5. Magnetic properties of undoped hematite nanorods

The Mössbauer spectra recorded for hematite samples synthesized using ACG are presented in Figure 5.10. The Mössbauer spectra of the samples grown for 4 h, 10 h, and 24 h are composed of hyperfine patterns with 6 lines. The analyzed results of the hyperfine pattern are listed in Table 5.2. The sample grown for 4 h exhibits a doublet that may be due to the superparamagnetism of the nanoparticles [59]. This means that our samples are a mixture of hematite (92.6%) and maghemite (7.4%). On the other hand, the spectra of the sample grown for 10 h and 24 h show a 6-line hyperfine pattern without a superparamagnetism phase. The magnetic field of 505.1 kOe with the isomer shift of 0.326 mm/s and the quadrupole splitting of -0.112 mm/s was obtained for the sample grown for 4 h. The sample grown for 10 h has the magnetic field of 507.9 kOe with the isomer shift of 0.325 mm/s and the quadrupole splitting of -0.110 mm/s. The 24 h sample has also a magnetic field 459.1 kOe and the isomer shift and the quadrupole splitting of 0.300 and -0.108 mm/s, respectively. The 24h sample has a magnetic field that suggests that the sample is made of maghemite. These magnetic field values are slightly smaller than the magnetic field of the bulk hematite of 519 kOe. This might be due to the presence of the gamma phase iron oxide in the samples as indicated by the XRD results.

However Zboril et al (2002) [37] and Kim et al (2001) [149] reported that the magnetic features of hematite, including the temperature values of magnetic transitions, can be largely influenced by numerous factors, such as pressure, external magnetic fields, lattice defects, presence of impurities, surface phenomena and, in particular, ion substitution, and the size of particles, which maybe the case in our samples.

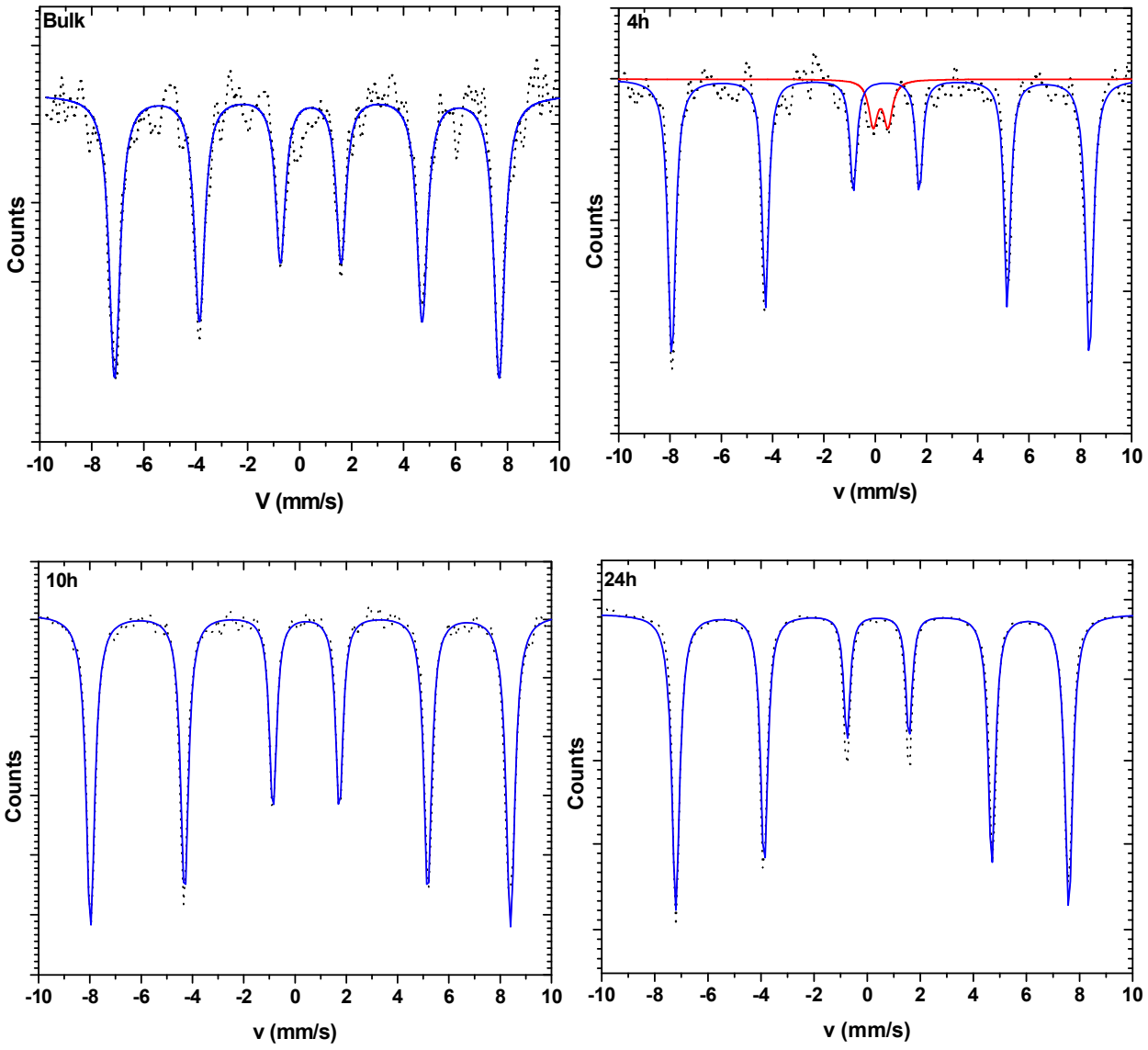

Figure 5.10 The Mössbauer analysis of the undoped hematite powder samples grown at different aging time at the growth temperature equal to 95^{o}C.

Table 5.2 The values of the magnetic field, Isomer (CS) and quadrupole shift (e) of hematite samples as extracted direct from the Mössbauer analysis.

Sample ID	**H (kOe)**	**CS (mm/s)**	**QS (mm/s)**	**A(counts mm/s)**	**w3(mm/s)**
Bulk sample sextet	459.02	0.35	-0.076	12800	0.216
4 h sample Sextet (92.4%) Doublet(7.7%)	505.09	0.33 0.23	-0.112 0.56	92800 7400	0.193
10 h sample Sextet	507.99	0.32	-0.110	161500	0.160
24 h sample Sextet	459.09	0.30	-0.108	441300	0.146

5.4.6. Optical properties of undoped hematite nanorods

The optical transmission and absorption spectra of the α-Fe_2O_3 films deposited at different times (2, 4, 10 and 24 h) on FTO coated glass substrate are shown in Figure 5.11 and Figure 5.12, respectively. The transmission gradually increases while the absorption gradually decreases as the wavelength extends toward the visible region. The absorption of the samples increases as the deposition time increases and this is clearly observed in Figure 5.13, which is due to the increase in the thickness.

From 540-600 nm wavelength range the absorption decreases significantly and becomes linear into the infrared region. Beermann et al (2000) [39] reported that, the presence of an absorption tail between 540 and 600 nm probably indicates the existence of sub-band gap states.

The Tauc plot in Figure 5.13 shows the relationship between the incident photon energy ($h\nu$) and the absorption coefficient (α) near the absorption edge. The band gap is estimated from the intercept of the extrapolated linear fit to the experimental data of $(\alpha\, h\nu)^2$ vs. photon energy plot. The obtained values of the band gap which are not following a trend with increase of the deposition time; are in the range of 2.1 to 2.22 eV and these are in good correspondence with the previously reported values of 1.9 to 2.2 eV depending on crystalline status and methods of preparation of α-Fe_2O_3 thin films.

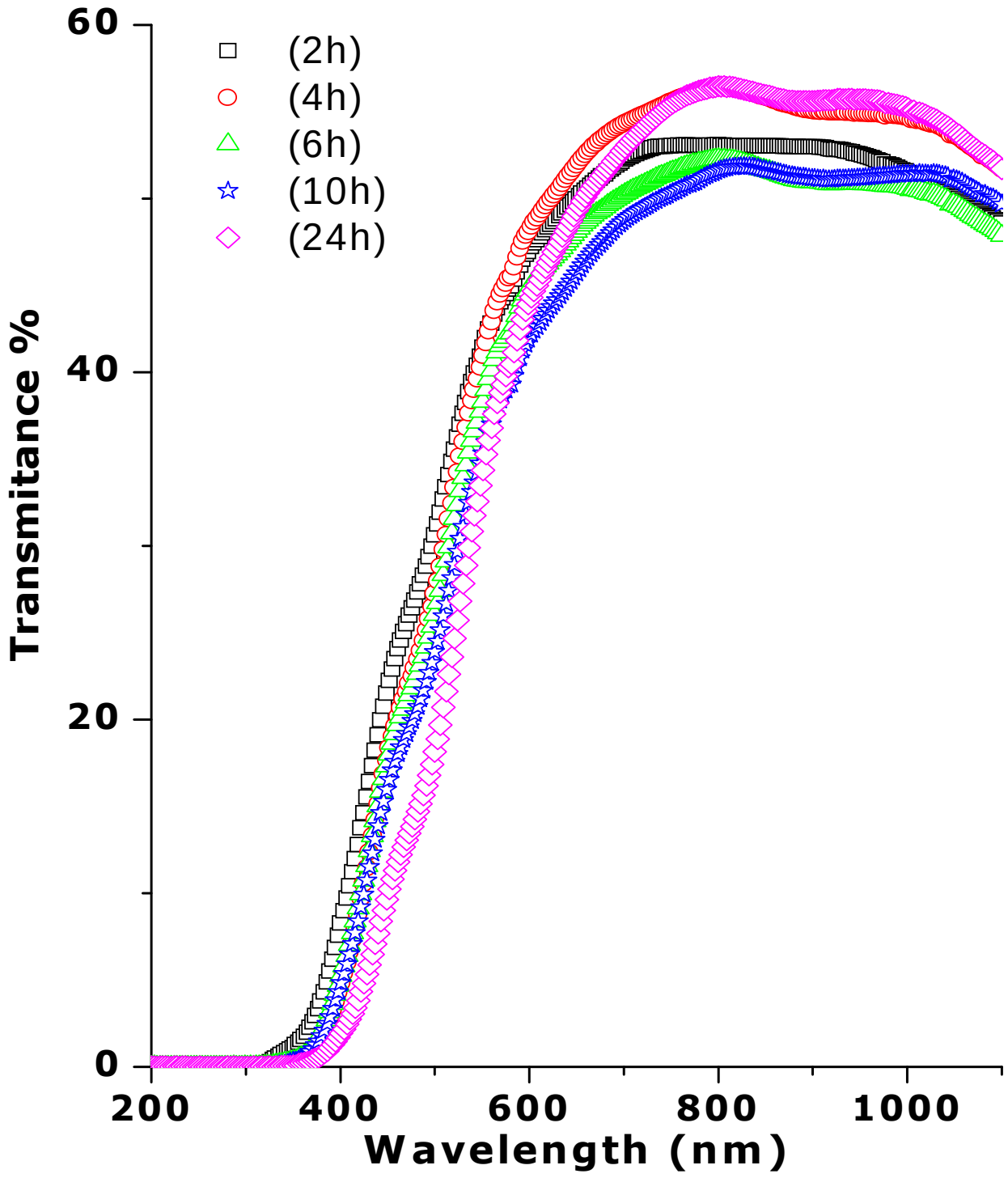

Figure 5.11 The transmission curves of α-Fe_2O_3 nanorods thin films samples deposited on FTO glass substrate at different aging times (as indicated on the graph) at the deposition temperature of 95^{o}C.

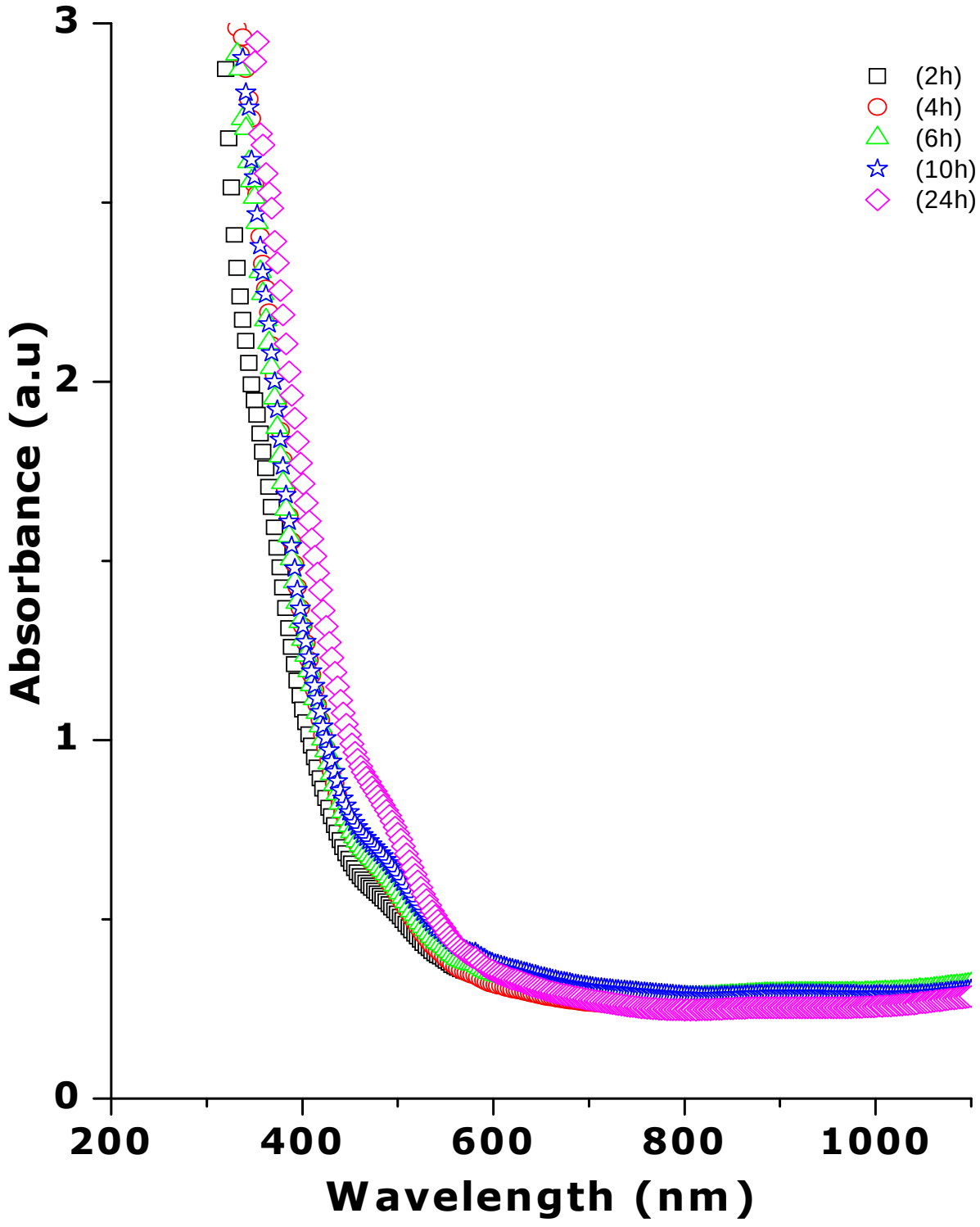

Figure 5.12 The absorption curves of α-Fe_2O_3 nanorods thin films samples deposited on FTO glass substrate at different aging times at the deposition temperature equal to 95^{o}C.

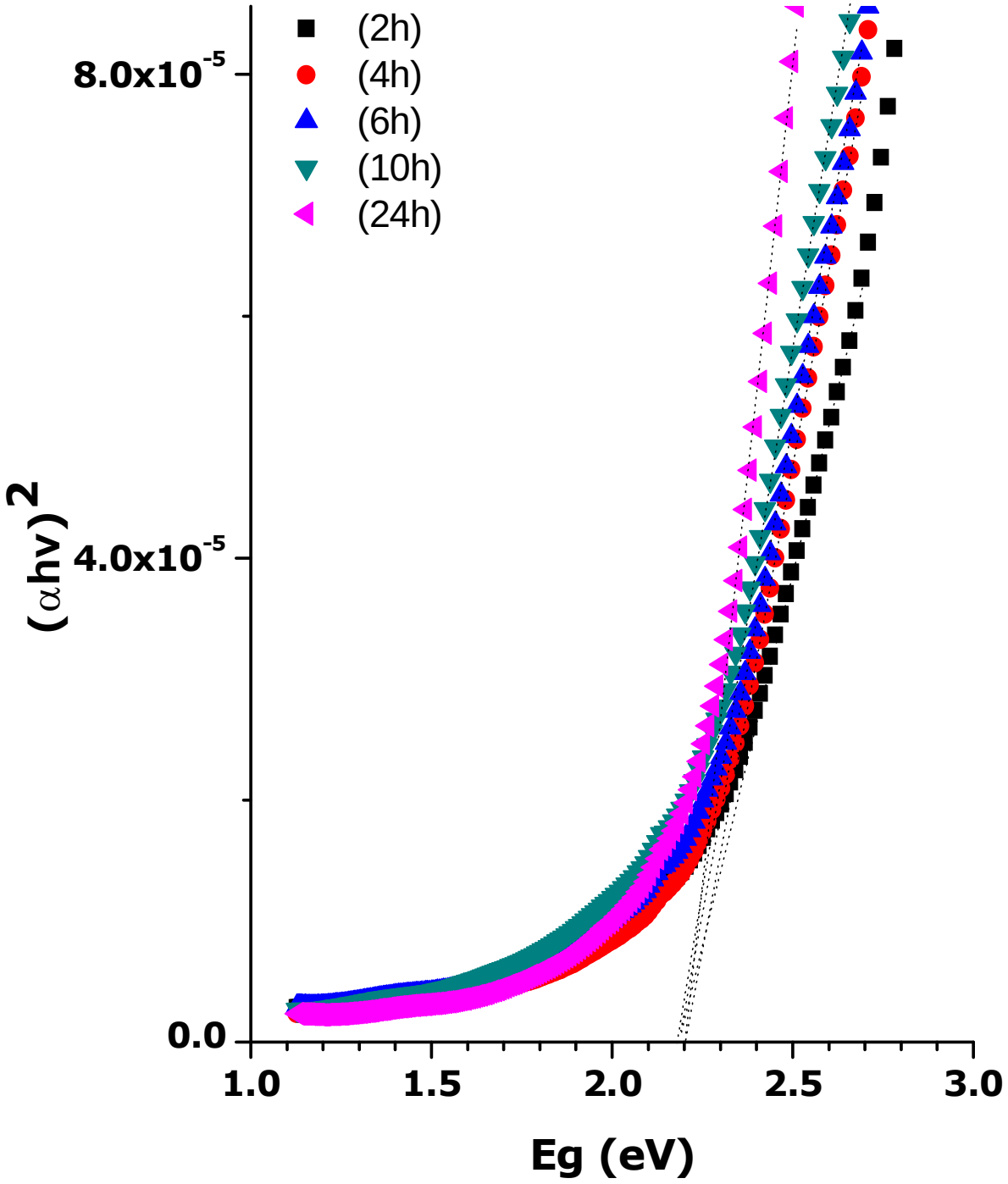

Figure 5.13 The band gap estimation of the hematite samples grown on FTO glass substrate at different aging time using ACG

5.5. The effect of pH on the properties on the iron oxide nanostructures.

5.5.1. Structural properties

The samples were grown for 24 h on corning glass substrate. After deposition the samples were cleansed and heat-treated at 500^{o}C for 1 hour. The thin films samples were then subjected to XRD for crystalinity measurement. Figure 5.14 presents the XRD patterns of hematite thin films as function of pH. According to the JCP2 CAT: No. 73-0603, the peaks corresponding to the values of 2thetha equal to 24.14^{0}, 33.15^{0}, 35.61^{0}, 39.28^{0}, 40.86^{0}, 49.48^{0}, 54.09^{0}, 56.15^{0}, 57.59^{0}, 62.45^{0} and 63.99^{0}, can be assigned to the following planes (012), (104), (110), (113), (024) (116), (214) and (300) respectively and are the reflections from α-Fe_2O_3 (hematite) rhombohedral with the R-3C space-group structure and the lattice parameters a=5.0356, c=13.7489 and z=6. Whiles the peak at 2thetha (32.1^{o}) marked with γ is a reflection of the maghemite (γ-Fe_2O_3) phase according to the JCP2 CAT No 00-039-1346. The samples prepared at a pH 1.16 and pH 1.5; were seem to be likely amorphous. The samples grown at the pH of 1.75, 2.0 and 2.5 are found to be a mixture of γ-Fe_2O_3 and α-Fe_2O_3 phases, while an increase in the pH deposition leads to the pure α-Fe_2O_3 phase.

5.5.2. Surface morphology

The SEM images of α-Fe_2O_3 nanostructures are presented in Figure 5.15. The morphology and orientation of the obtained Fe_2O_3 nanostructures were found to be affected by the pH of the solution. At a pH of 1.16 very small size needle-like nanorods random oriented parallel onto the substrate were obtained. At a pH of 1.5 the nanorods exhibits a cubic shaped with the mixed orientation (random and perpendicular) onto the substrate. Increasing the pH to 1.75 and 2.0, the cubic shaped nanorods perpendicular oriented onto the substrate are observed while from pH 2.5 to pH 3.2 only cubic structured nanorods with a spherical shape at the tip are observed to be perpendicular oriented onto the corning glass substrate. In addition in the range of pH 3.5 to pH 5.0 the spherical tip shape nanorods randomly parallel on the substrate are observed. Following the above observations, it is clear that the morphological characteristics of as-prepared α-Fe_2O_3 nanorods arrays are controlled by the concentrated hydrochloric acid. This is due to the fact that

increasing the pH to higher values lead to, the increase in the precipitate after every generation time which promotes the random orientation of these nanostructures.

The (image J) software was used to measure the average length and diameter of the nanorods and as shown in Figure 5.16, the increase in pH values induces a noticeable increase in the diameter of the rods. The effect of the pH on the rodôs average lengths is that the longest rods were obtained at the pH 1.5 and above this pH values there was a noticeable decrease in the average length as illustrated in and Figure 5.17, respectively. This is true because the nanoparticles size is strongly dependent on the acidity of the precipitation medium: the lower the pH the smaller the particle size. It is therefore demonstrated that the best engineered pure nanorods of α-Fe_2O_3 as manifested by the XRD results can be grown at pH range of pH 3 and pH 3.2. The nanorods with the longest length and smaller diameter are obtained at pH range of pH 1.16 and pH 2.0. Pottier et al (2003) [150] reported that for metal oxides, both the pH and the ionic strength impose the electrostatic surface charge of particles and consequently the chemical composition of the surface.

The pH acts on the protonation deprotonation equilibrium of surface hydroxylated groups (positive charge at pH < PZC); the ionic strength carries out electrostatic screening between charged groups on the surfaces and then, at fixed pH, the electrical charge depends on the ionic strength (I). Adsorption of chemical species (H^{1+}, anions of the electrolyte) and settling of the surface electrical charge must therefore induce a decrease in the interfacial tension with respect to its value at the point of zero charge (PZC).

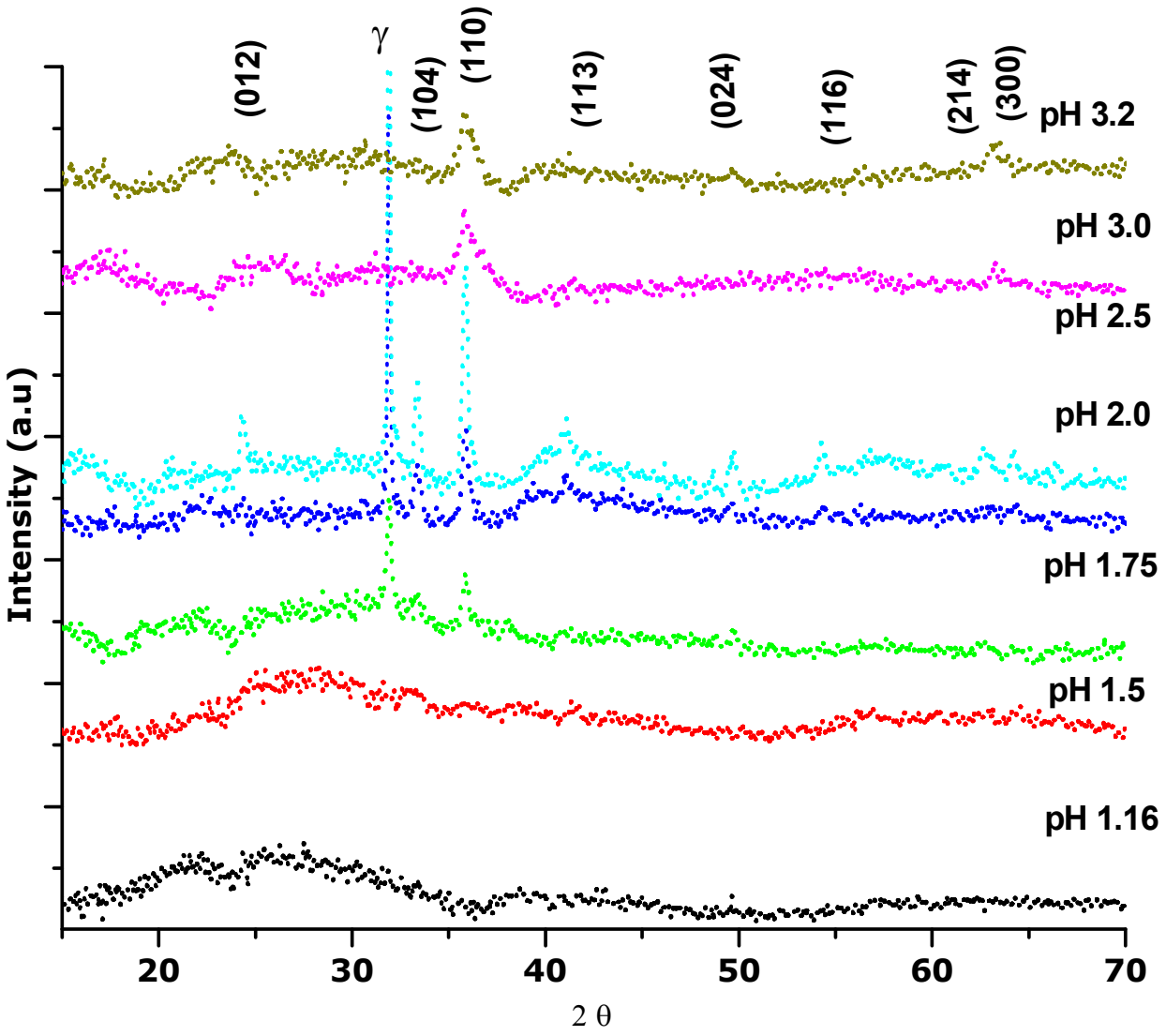

Figure 5.14 The XRD pattern of the pH dependent growth of hematite nanorods on corning glass substrate at a constant aging time equals to 24h and deposition temperature equals to 95^{o}C.

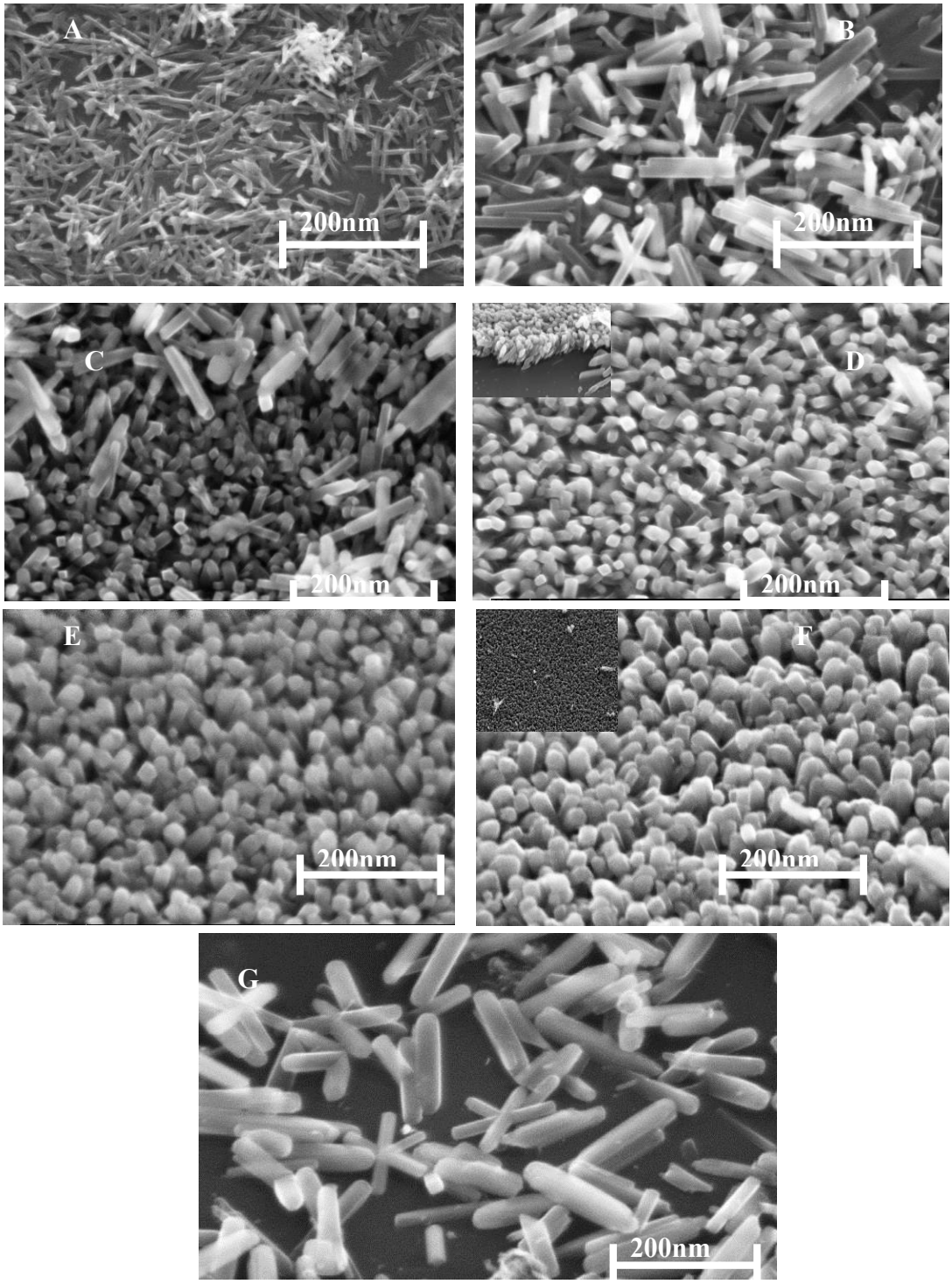

Figure 5.15 The pH dependent SEM images of hematite nanorods deposited on corning glass substrate grown using ACG for a deposition time equals to 24 h and deposition temperature equals to 95 ^{o}C. (a) pH 1.15, (b) ph1.5, (c) pH 1.75, (d) pH 2.0, (e) pH 2.5, (f) pH 3.0 and (g) pH 5.0. The imaging was done at a scale of 200nm.

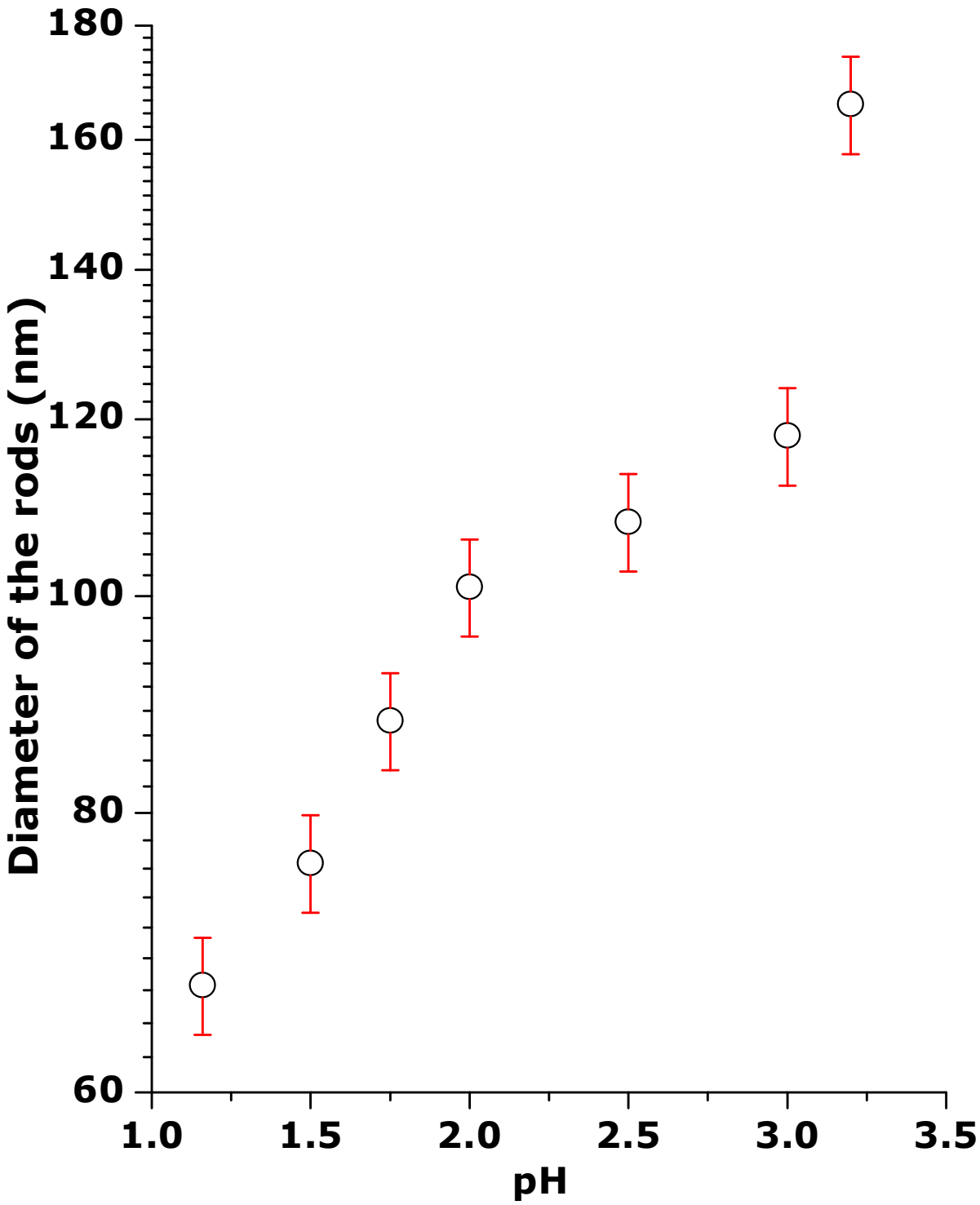

Figure 5.16 The pH dependent average diameter of hematite nanorods grown on corning glass substrate at a constant aging temperature and aging time equals to 95^{o}C and 24 h respectively.

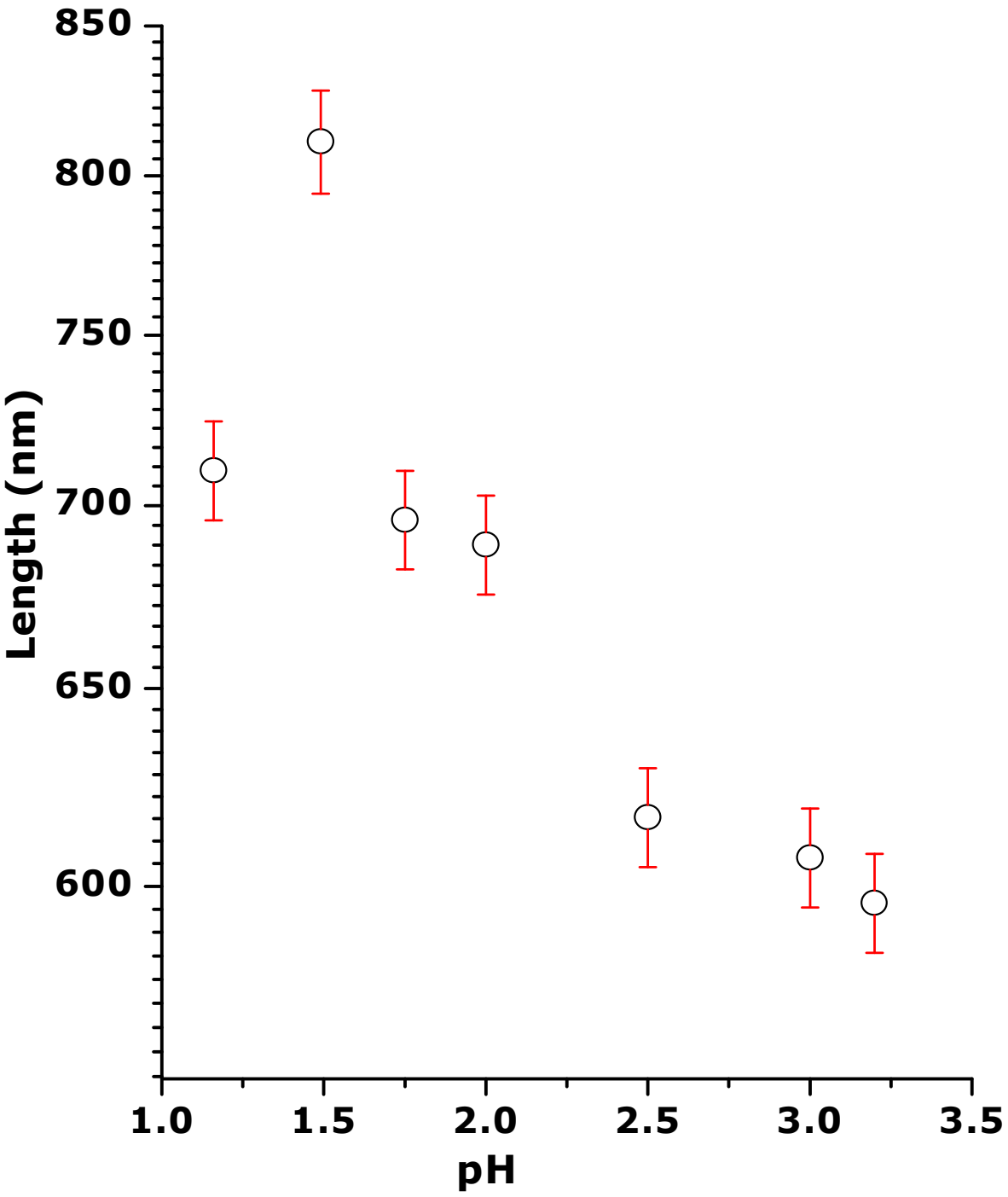

Figure 5.17 The pH dependent average length of hematite nanorods grown on corning glass substrate at a constant aging temperature and aging time equals to 95^{o}C and 24 h, respectively.

5.5.3. The Mössbauer analysis on the samples grown for various pH values

The Mössbauer spectra for the samples grown with the pH 1.16, pH 1.5 and pH 2.0 are presented in Figure 5.18. The measurements were performed at room temperature on thin films. The Mössbauer spectra of the samples grown with pH 1.16, pH 1.5 and pH 2.0 for 24h are composed of two hyperfine patterns with 6 lines.

The analyzed results for the hyperfine pattern are listed in Table5.3. As summarized in the Table the sample grown at pH 1.16 has a first sextet with magnetic field of 517 kOe, the isomer shift of 0.38 mm/s and the quadrupole splitting of -0.11 mm/s. The second sextet with the magnetic field 415 kOe, isomer shifts 0.29 mm/s and the quadrupole splitting -0.12 mm/s have been observed.

The first hyperfine with 6 lines for pH 1.5 exhibit the magnetic field 518 kOe with the isomer shift of 0.36 mm/s and the quadrupole splitting of -0.114 mm/s, while the second sextet have the magnetic field of 411 kOe with the isomer shift and the quadrupole splitting of 0.18 mm/s and -0.16 mm/s, respectively.

The pH 2 sample have the first sextet with the magnetic field 518 kOe and the isomer shift of 0.37 mm/s and the quadrupole splitting of -0.104 mm/s, the second sextet have the magnetic field of 413.6 kOe, isomer shift of 0.38 mm/s and the quadrupole splitting of -0.031 mm/s.

The isomer and the quadrupole splitting are in good agreement with the results reported by Zboril et al (2002) and Kim et al (2001).The results for the first hyperfine in all the samples are in good agreement of the magnetic hyperfine of hematite. The second hyperfine with 6 lines has a smaller magnetic field which may be related to the nanosize interference. This also may be the indication of the mix phase of iron oxide, which may be linked to of maghemite as suggested by XRD results.

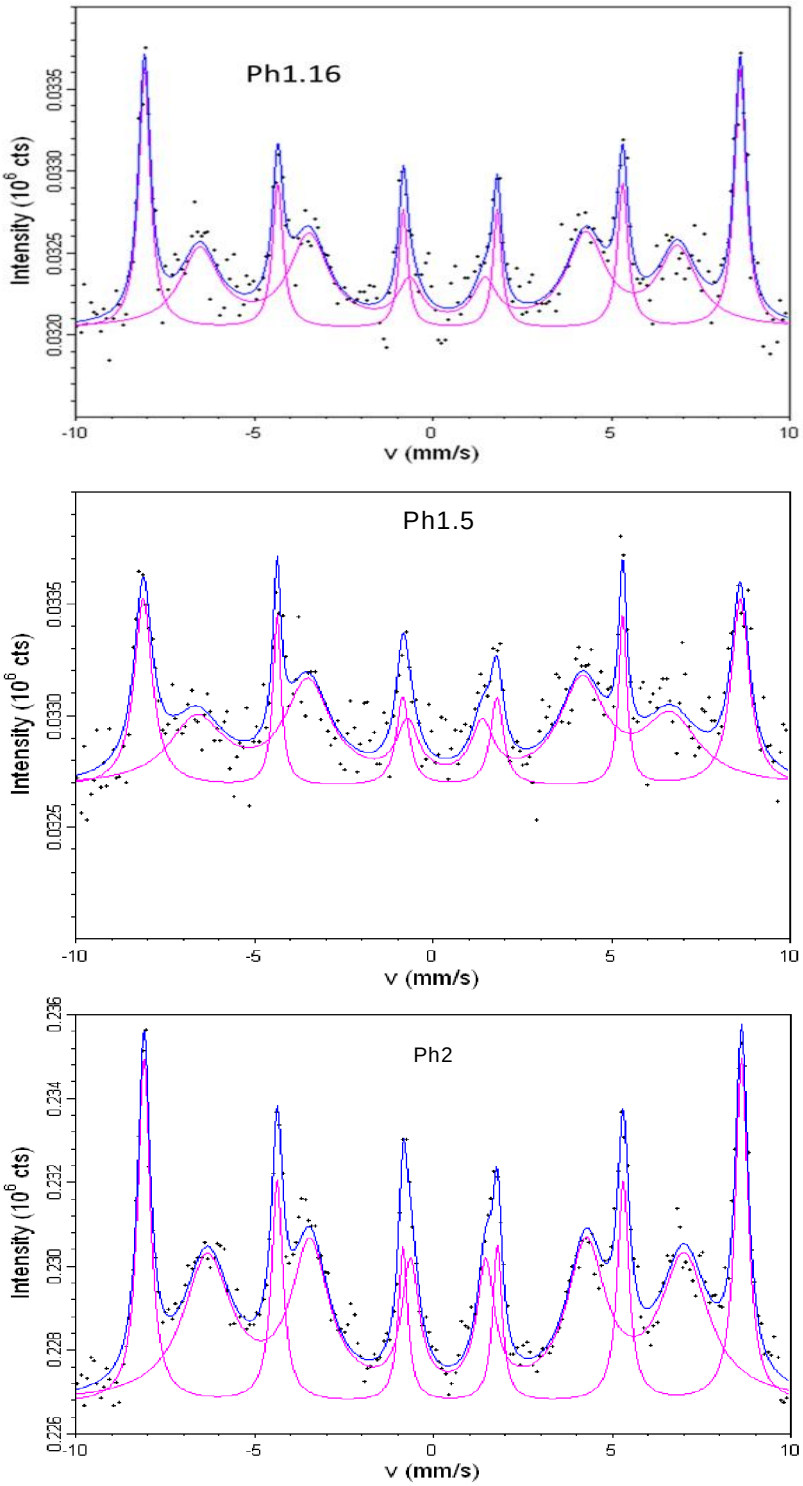

Figure 5.18 The pH dependent Mössbauer analysis of hematite nanorods grown on corning glass substrate for 24h at constant temperature equals to 95°C.

Table 5.3 The summary of the Mössbauer analysis for the hematite nanorods grown at pH 1.16, pH 1.5 and pH 2 for 24 h at 95 °C.

Sample with two sextet	**H(kOe)**	**CS(mm/s)**	**QS (mm/s)**	**A(counts mm/s)**	**w3(mm/s)**
pH 1.16 (1)	517.3	0.38	-0.11	-3640	0.15
(2)	415.0	0.29	-0.12	-4900	0.40
pH 1.5 (1)	518.0	0.36	-0.11	-2800	0.22
(2)	411.0	0.18	-0.16	-4500	0.37
pH 2 (1)	518.4	0.37	-0.10	-20900	0.16
(2)	413.6	0.38	-0.03	-37700	0.30

5.5.4. The optical properties

Figure 5.19 and Figure 5.20 present the transmission and the absorption of the thin films of hematite grown at various pH values. The increase in the pH from 1.16 to 3.2 does not only affect the orientation of the nanorods but also affect the band gap as reported previously on the morphological study section. This may be due to the change in the thickness on the samples. From 540-650 nm the absorption decreases significantly and becomes linear into the Infrared region as shown in Figure 5.20.

The estimated values of the band gap from Figure 5.21 are ranging between 2.1 eV to 2.3 eV, which are in correlation with the previously reported values [16,129,151,152]. The evolution of the band gap as a function of the pH does not follow any trend. This is may be due to the change in the crystallinity or due to the quantum confinement effect as reported previously by Vayssieres et al (2005) [16].

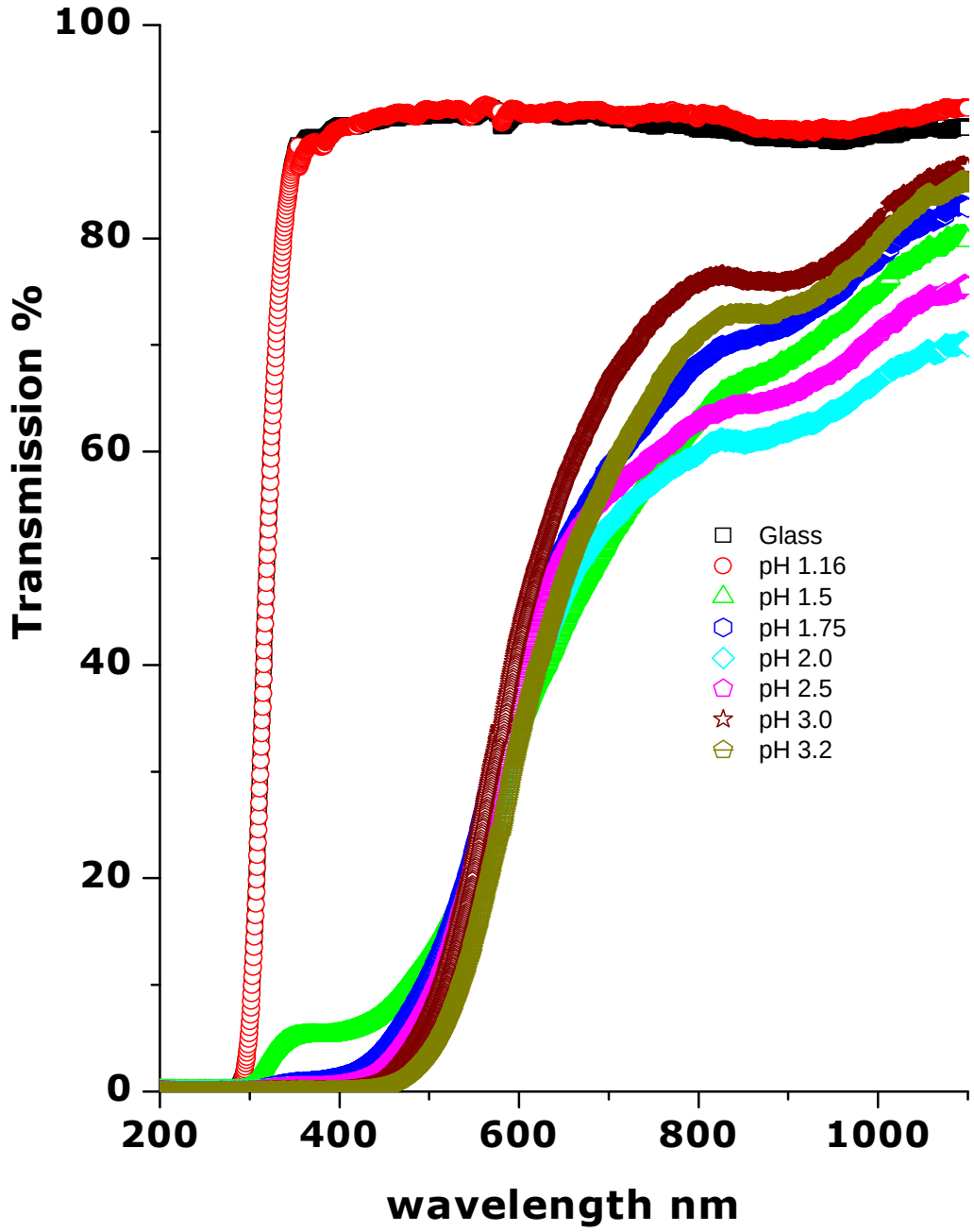

Figure 5.19 The pH dependent UV-Vis transmission curves of hematite nanorods deposited on corning glass substrate at the growth temperature equals to 95^{o}C deposited for 24h.

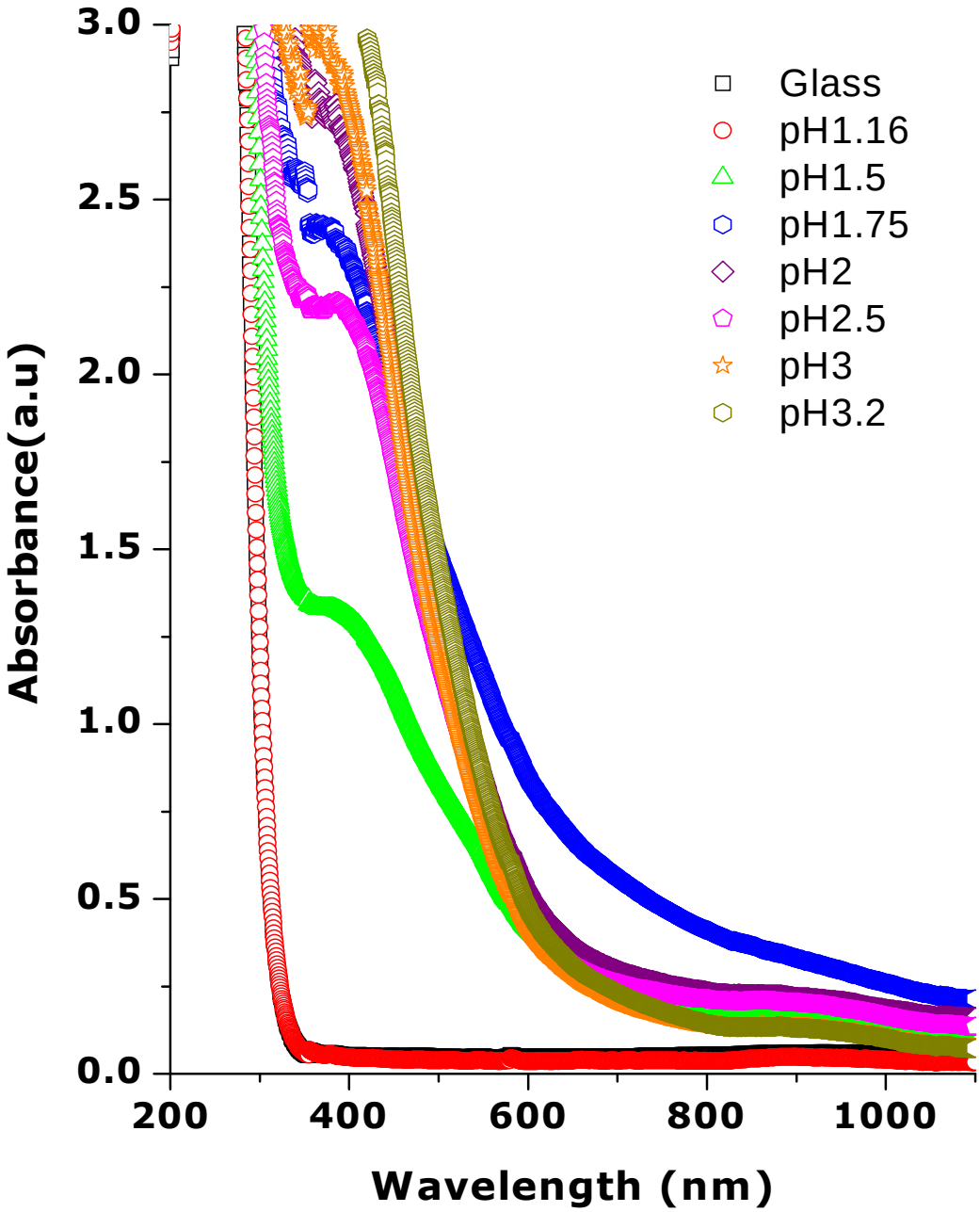

Figure 5.20 The absorption curves of hematite nanorods deposited for 24 h on corning glass substrate at different pH values 95^0C.

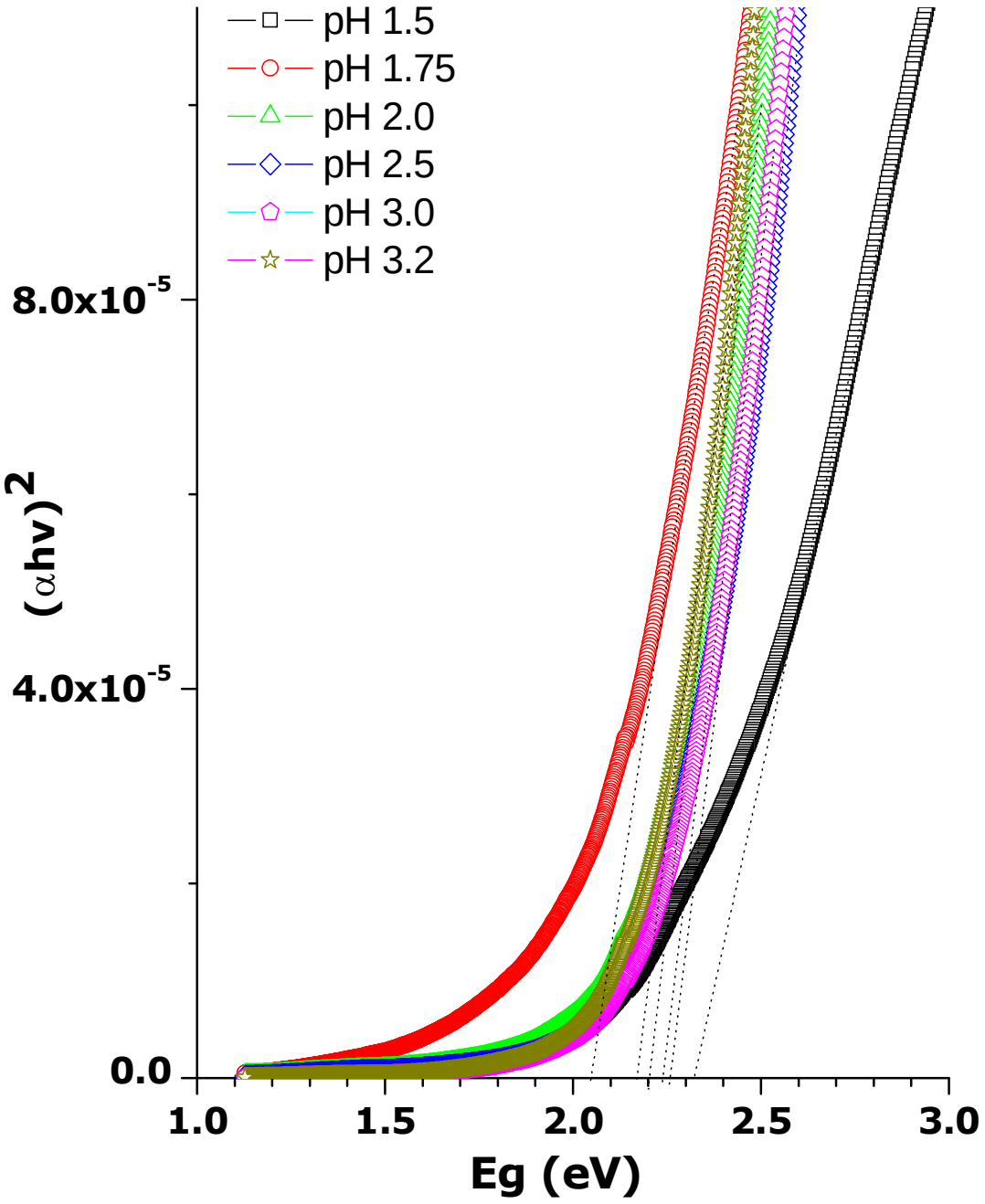

Figure 5.21 The band gap estimation of hematite nanorods grown for 24 h on corning glass at different pH values at 95°C.

5.6. The synthesis and characterization of Ru doped hematite nanorods

The samples analyzed in the following sections have been deposited with the pH 1.5 at the temperature 95^{o}C on FTO substrate. This specific pH value is use because of its ability to produce the perpendicular orient nanorods with the longest length and the smallest diameter. The growth of nanorods of hematite at this pH has been reported previously in the literature [153].

5.6.1. Structural and morphological properties (XRD) of Ru-doped hematite

The samples were grown for 24 h on FTO coated glass substrate. Figure 5.22 presents the XRD patterns of hematite nanostructures as a function of dopant concentration. According to the JCP2 CAT: No. 73-0603 and No. 1309-37-1 of α-Fe_2O_3, the peak corresponding to the values of 2thetha equal to 24.14^0, 33.15^0, 35.61^0, 39.28^0, 40.86^0, 49.48^0, 54.09^0, 56.15^0, 57.59^0, 62.45^0 and 63.99^0, can be assigned to the following planes (012, 104, 110, 024, 116, 214,113, 018, 134, 1010, 220 and 300) respectively. The intensity of the plane of (104) indicates that the Ru-doped hematite particles are oriented in (104) direction. The intensity of this strongest peak turns to decrease and broadens as the Ru dopant concentration increases. This is probably due to the interstitial substitution and structural disorder induced by Ru atom in hematite crystal structure. There is no XRD reflection coming from RuO_2 which confirm the purity of the α-Fe_2O_3 doped. The FWHM of (104) plane was used in the Schererôs equation ($D = K\lambda / B\cos\theta_B$) as described in chapter 4 to calculate the crystal size (D) as shown in Figure 5.23. The crystalline size of the doped samples ranges from (1.5 nm ï 3 nm) with an increase in the dopant concentration. Figure 5.24 present the EDX information, where the peaks assigned for Si, Ca and K are the reflection from the glass substrate. The analyzed samples gives a reflection of ruthenium (Ru) as a dopant, iron (Fe), and oxygen (O). The following ruthenium atomic weights were found in each sample 0.14 a%, 0.08 a% and 0.06 a% which correspond respectively to 0.03g, 0.018g and 0.006g of $RuCl_3xH_2O$ precursor used during the synthesis. Figure 5.25 presenting SEM images of the undoped and Ru-doped hematite samples. The thin films contain nanorods. The undoped sample exhibits perpendicular oriented nanorods arrays while the doped ones contain randomly oriented nanorods arrays onto the substrate. The further increase in the dopant concentration leads to the disappearance of the nanorods on the substrate.

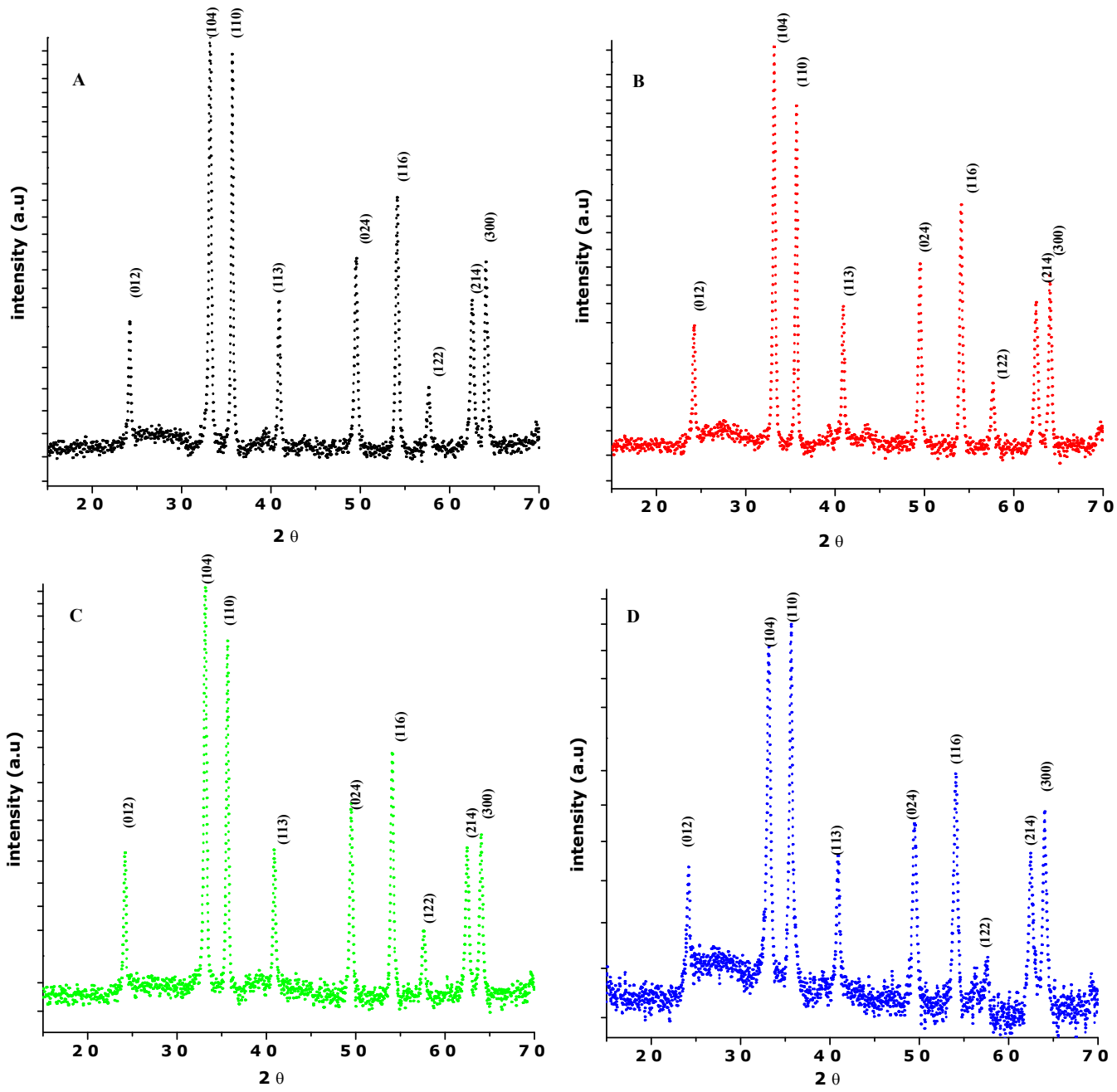

Figure 5.22 The XRD patterns of hematite powder samples grown for 24 h at 95°C as a function of dopant concentration, where A is represent undoped, B for 0.006g, C for 0.018g, D for 0.030g. The $RuCl_3.xH_2O$ salt was used as a doping precursor.

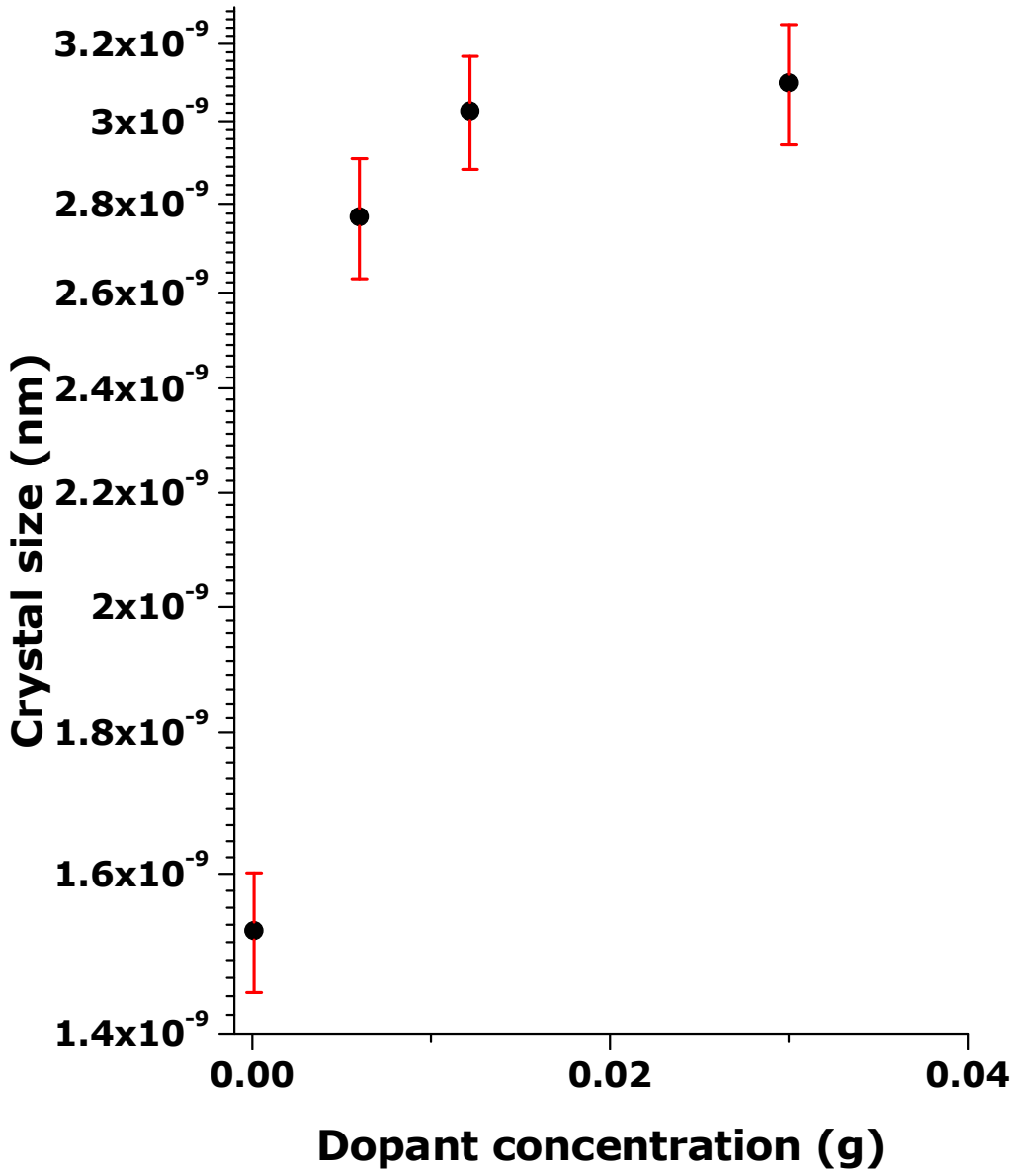

Figure 5.23 The Schererôs equation is used to estimate crystal size of the grown nanoparticles using the FWHM of (104) peak on the XRD patterns of each of the patterns.

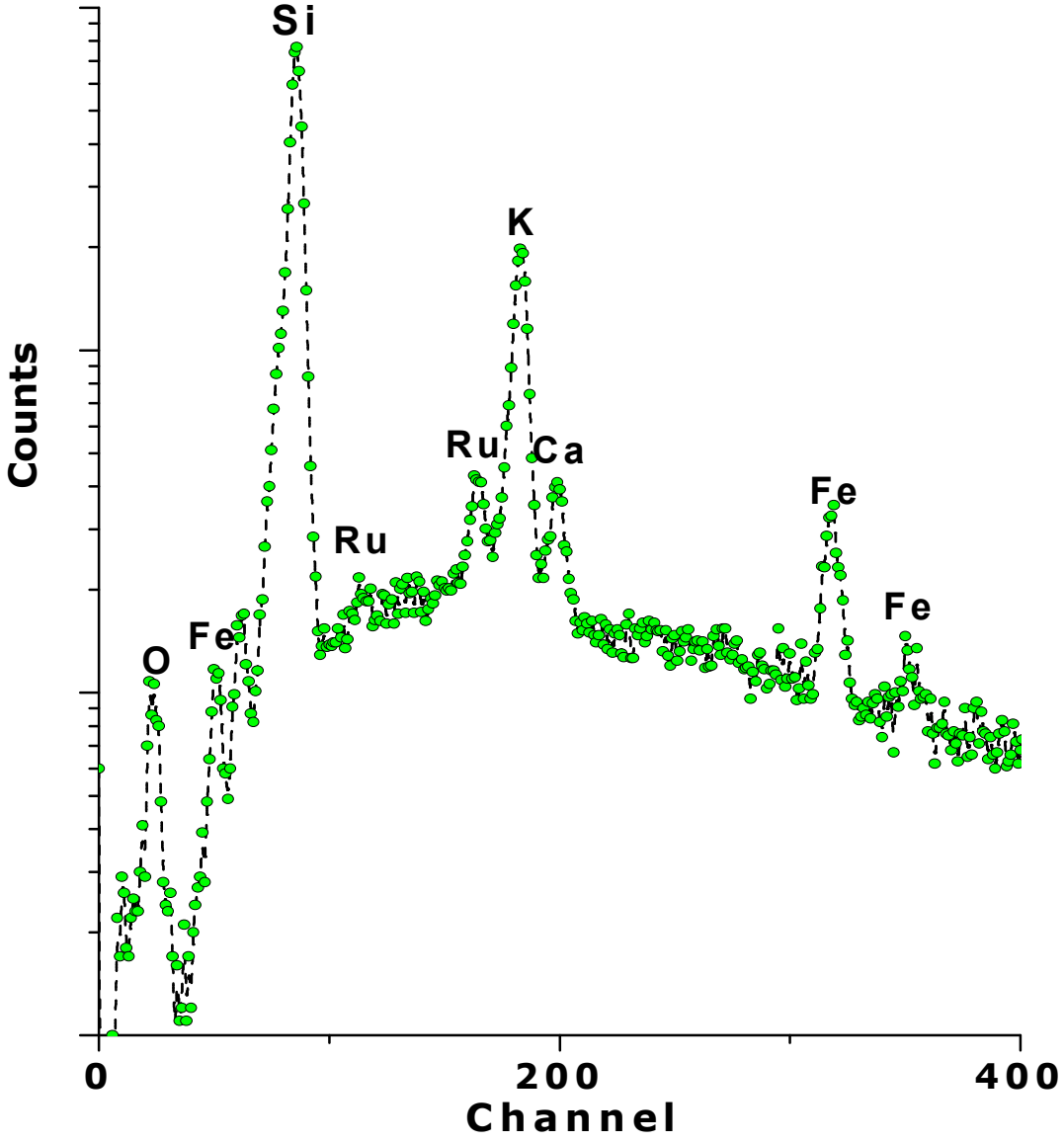

Figure 5.24 The EDX results showing the presence of Ru as the dopant. The Si, Ca and K were originating from the silicon wafer substrate.

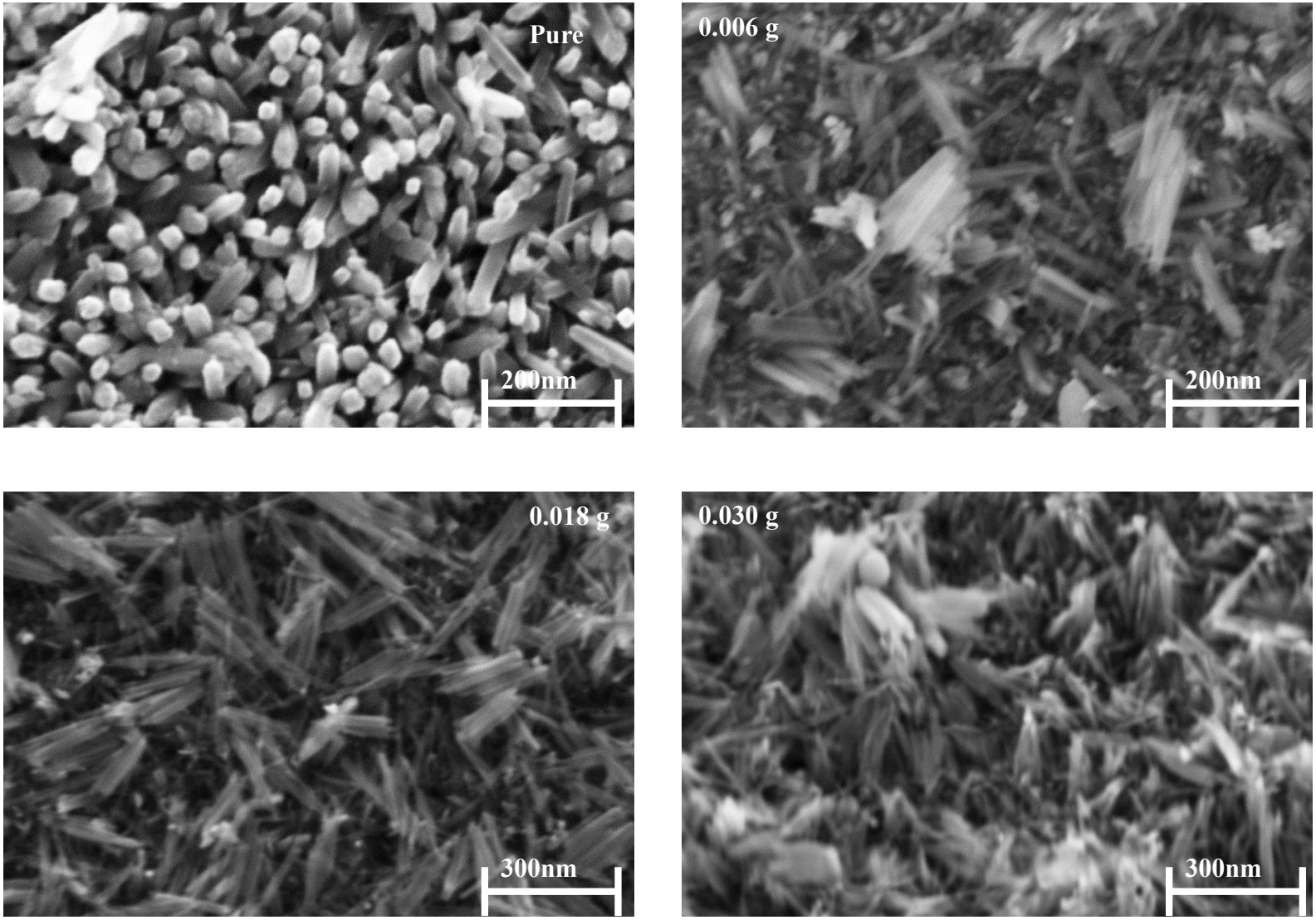

Figure 5.25 The SEM images of the undoped and Ru doped α-Fe_2O_3 samples grown on FTO glass substrate for 24 h at 95^{o}C and the amount of $RuCl_3.XH_2O$ is indicated on each image.

5.6.2. Raman analysis on Ru doped hematite nanorods

The Raman spectra for Ru doped hematite samples are shown in Figure 5.26. All vibrational modes for hematite are present as shown in Figure 5.26. The Raman mode positions are summarized in Table 5.4. The Eg (1) vibrational mode at about 288 cm^{-1}intensity decreases with an increasing in the dopant concentration. The vibrational mode around 1124 cm^{-1} is due to Ruthenium bonded to oxygen as reported by Jo et al (2005) [154]. The higher the dopant concentration, the lesser the intensity and also the broader is the width of the vibration modes. This indicates the loss of crystalinity in the samples when the dopant concentrations increases, and can be correlated to the broadening of the XRD patterns as reported above.

5.6.3. FT-IR analysis on the doped hematite nanorods

Figure 5.27 present the FTIR spectra of α-Fe_2O_3 samples deposited with concentration 0.006g and 0.03g of $RuCl_3xH_2O$ precursor. The sample prepared with 0.006g of $RuCl_3xH_2O$ exhibited pronounced IR active modes with the absorption bands at 337 cm^{-1}, 391 cm^{-1}, 471 cm^{-1}, 548 cm^{-1}, 874 cm^{-1}. The sample prepared with 0.03g of $RuCl_3xH_2O$ exhibited the same absorption bands but with weaker intensities which are due to the difference in crystalline quality with the doping. All the vibrational modes are assigned to hematite.

The vibrational modes reported by Sahoo et al (2010) [142] at 555 cm^{-1} and 463 cm^{-1} and in our sample they appear at 471 cm^{-1} and 548 cm^{-1} on sample prepared with 0.006g of $RuCl_3xH_2O$ while they appear at 456 cm^{-1}, 532 cm^{-1} on the sample deposited with 0.03g, of $RuCl_3xH_2O$, are due to the Fe-O stretching and bending vibration mode, respectively for α-Fe_2O_3. Zhao et al (2007) [143] reported the same bands at wavenumbers of 538 cm^{-1} and 466 cm^{-1}, therefore correlating the FTIR results with the XRD investigation. The mode at 471cm^{-1} and 456 cm^{-1} which are present in the sample prepared respectively for 0.03g and 0.006g can be assigned to the Fe-O stretching mode of Fe_2O_3.

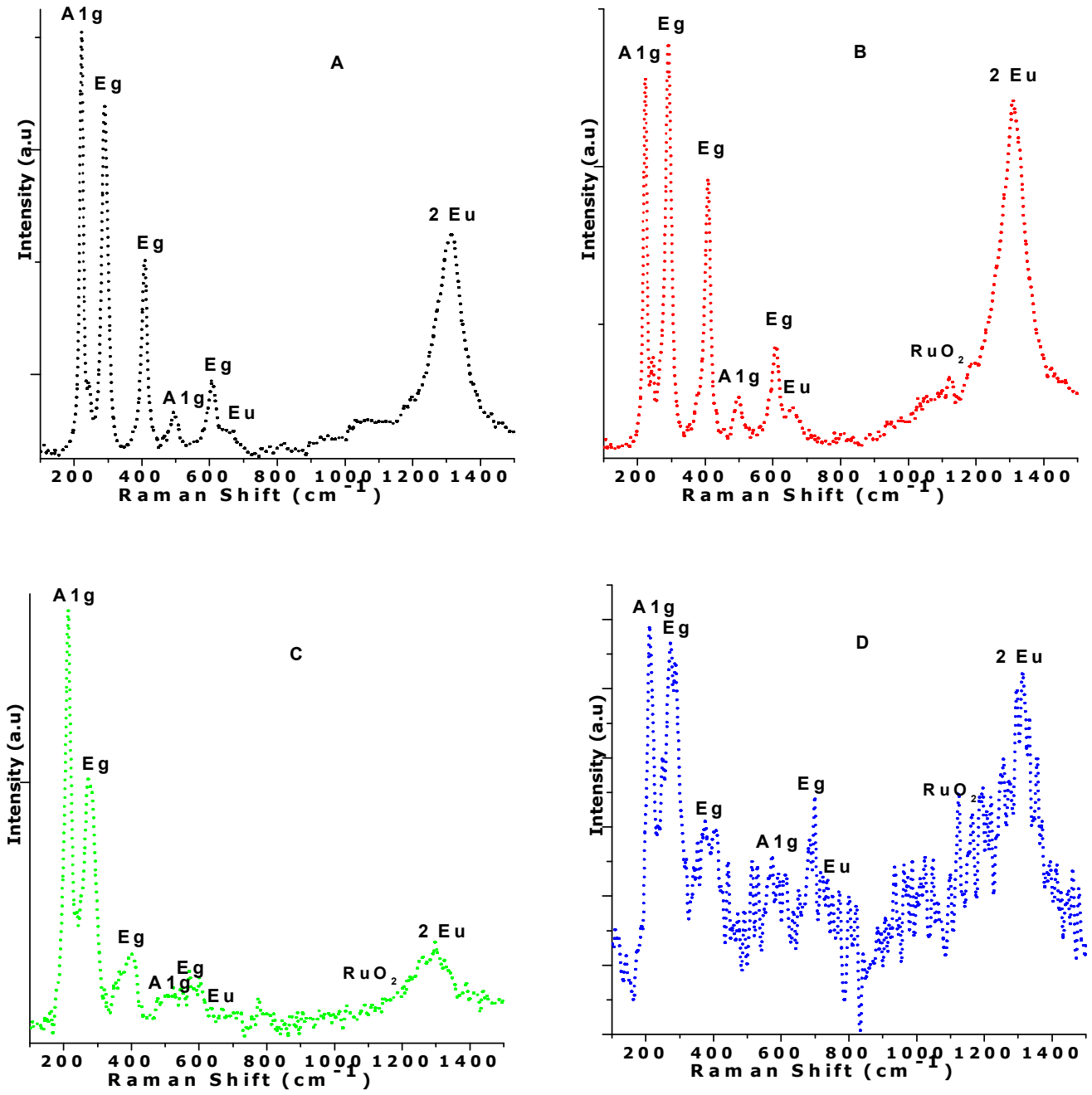

Figure 5.26 The Raman shifts of Ru doped hematite (Ru-α-Fe_2O_3) nanorods grown for 24 h on FTO glass substrate, where **A** present pure Fe_2O_3, **B** for 0.006g, **C** for 0.018g, **D** for 0.03g.

Table 5.4 The Raman shifts (cm^{-1}) for the Ru doped hematite nanorods grown for 24 h on FTO glass substrate, where **A** present pure Fe_2O_3, **B** for 0.006g, **C** for 0.018g, **D** for 0.03g.

Vibrational Mode	**A**	**B**	**C**	**D**
$A_{1g}(1)$	221.2	222.2	210.2	212.1
$E_g(1)$	241.9	243.4	-	-
$E_g(1)$	288.5	289.9	272.4	271.9
$E_g(1)$	407.5	407.5	374.3	398.7
$A_{1g}(2)$	492.3	494.6	-	-
$E_g(1)$	606.6	607.5	-	-
E_u	654	655.9	-	-
$2E_u$	1314	1307.8	1311.9	1311.9

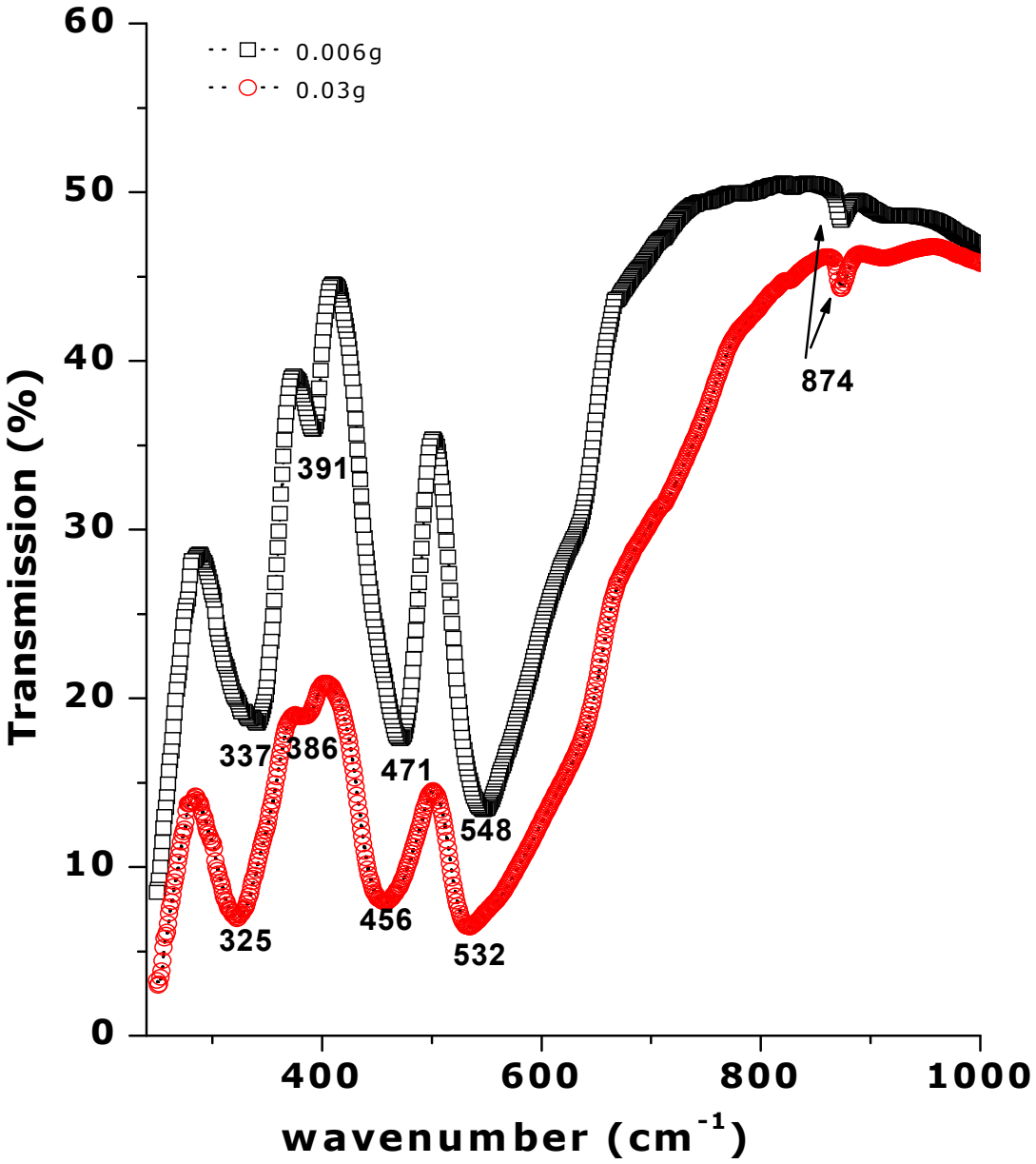

Figure 5.27 The FTIR signal of Ru doped hematite powder synthesized for 24 h at 95°C mixed in a pallet of KBr.

5.6.4. Mössbauer analysis on Ru doped hematite nanorods

Figure 5.28 presents the Mössbauer analysis of the Ru doped unheated samples of iron oxide. The Mössbauer spectra for samples grown with 0.006g, 0.018g, and 0.03g of dopant concentration have a doublet. This is the indication of the presence Ru-β-FeOOH in a super-paramagnetic form. Table 5.5 present the summarized values of the isomer shift and quadrupole splitting of the samples.

The Mössbauer spectra recorded for the ruthenium doped hematite samples synthesized using ACG are presented in Figure 5.29. The Mössbauer spectra of the samples grown with the dopant concentration of 0.006g, 0.018g, and 0.03g for 24h are composed of hyperfine patterns with 6 lines which mean that the phase present is of well crystalline [124].

The analyzed results for the hyperfine pattern are listed in Table5.6. Our results are slightly different from the results reported the on the same material by Helgason et al (2002) [155] which may be due to the synthesis procedure.

The samples provide the magnetic field ranging between 456 to 459 kOe, which confirm that the grown samples are of maghemite and this due to the fact that the samples were grown for 24 h and particle sizes are bigger therefore providing a bulk magnetic field. There is no signature of γ-Fe_2O_3 in the XRD data pattern. The same behavior has been observed for undoped samples grown for 24h.

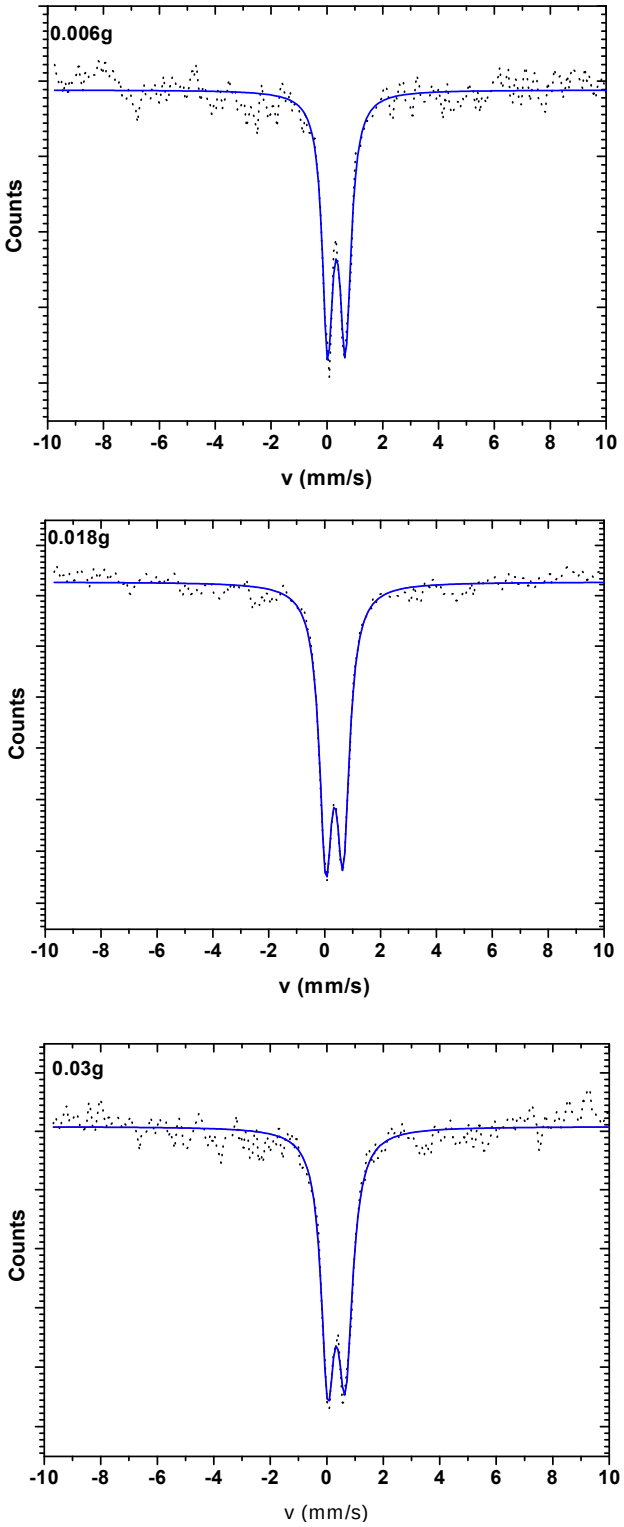

Figure 5.28 The Mössbauer analysis on an unheated Ru-doped iron oxide (akaganeite) powder samples deposited for 24 h.

Table 5.5 The Mössbauer analysis showing the isomer shifts and quadrupole splitting values for Ru doped unheated powder samples synthesized for 24 h at 95^{o}C.

Sample	**CS (mm/s)**	**QS (mm/s)**	**A(counts)·mm/s**	**w+(mm/s)**
0.006g	0.34	0.62	36400	0.32
0.018g	0.34	0.64	47100	0.24
0.03g	0.35	0.62	85800	0.28

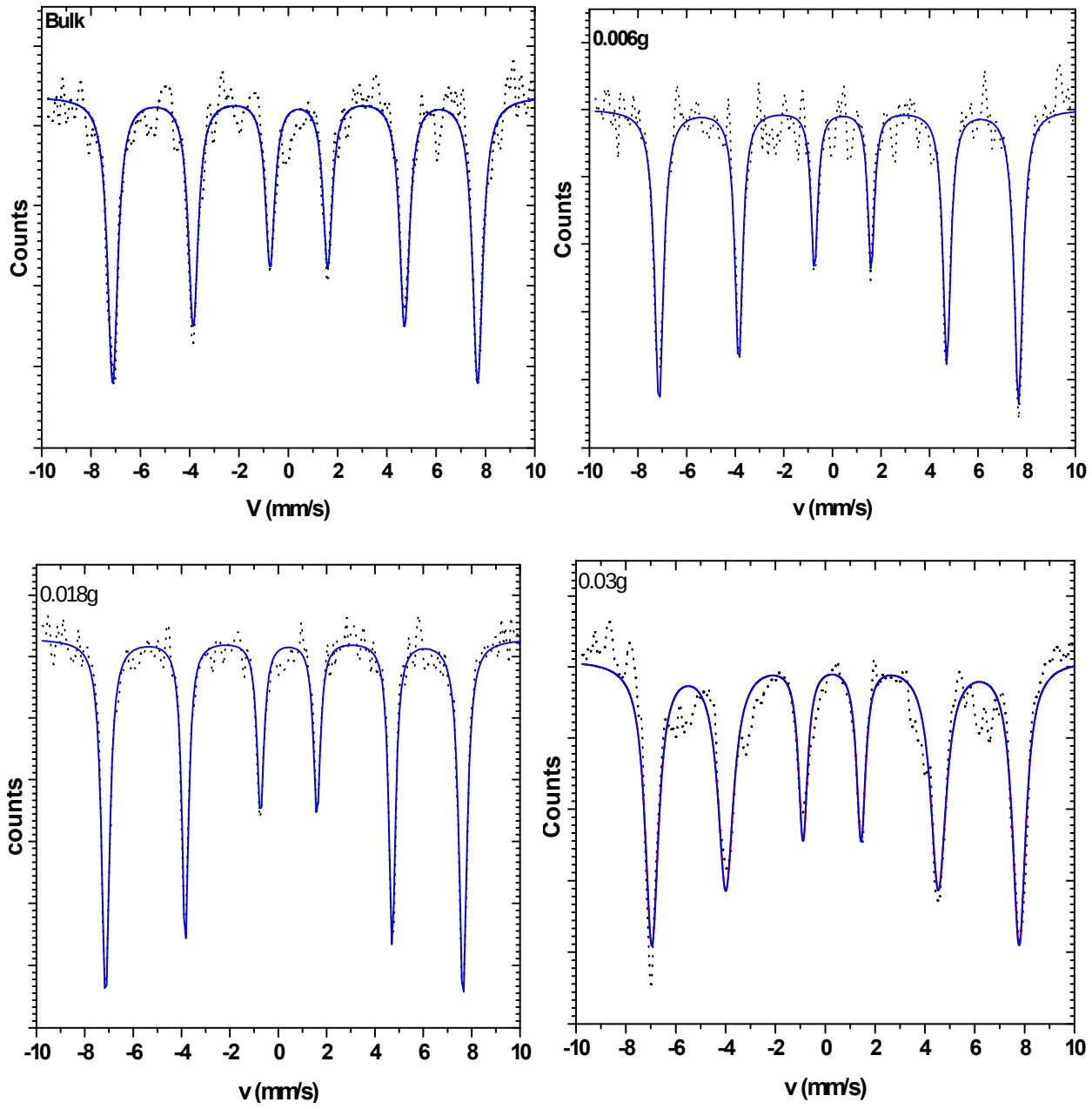

Figure 5.29 The Mössbauer analysis of Ru doped hematite powder samples deposited for 24 h at 95°C.

Table 5.6 The Mössbauer analysis indicating the magnetic field, isomer shifts and quadrupole splitting values for Ru doped hematite powder samples deposited for 24 h at 95^{o}C.

Sample	**H (kOe)**	**CS (mm/s)**	**QS (mm/s)**	**A(counts mm/s)**	**w3(mm/s)**
0.03g	458.72	0.345	-0.082	24900	0.133
0.018g	458.27	0.341	-0.093	73400	0.136
0.006g	458.73	0.348	-0.092	58100	0.161
Bulk sample sextet	459.02	0.355	-0.076	12800	0.216

5.6.5. Optical properties of Ru doped hematite nanorods

Figure 5.30 presents the UV-Vis optical transmission of Ru doped hematite samples. The transmission decreases as the dopant increases. The optical absorption spectra are presented in Figure 5.31. The absorption spectra of the samples were used to calculate the band gap of Ru doped hematite samples. It has been reported that the band edge position can be tailored by the electronegativity of the dopants as well as by quantum confinement effects.

Figure 5.32 presents the plot of the $(\alpha h\nu)^2$ as a function of $h\nu$ from which the band gap of the Ru dope hematite nanorods was estimated to be 2.46 eV for both samples deposited with 0.006g and 0.018g and for the sample prepared with 0.03g of $RuCl_3xH_2O$ the band gap was found to be 2.48 eV. This indicate a shift of about (0.26-0.56 eV) for both samples prepared with 0.006 and 0.018g of $RuCl_3xH_2O$ doping precursor and (0.29-0.59 eV) for sample deposited with 0.03g of $RuCl_3xH_2O$ doping precursor.

These shifts are in correspondence with the required shift on hematite band gap reported in the literature that induces the upward shift of the conduction band edge. This substantial increase in the band gap may be due to the dopant and the quantum confinement. It has been reported that the optimal band gap of 2.46 eV [15] is required for water photo-oxidation without an external bias therefore our obtained values would allow to manufacture a water splitting device without external bias which was in line with the objectives of this thesis work.

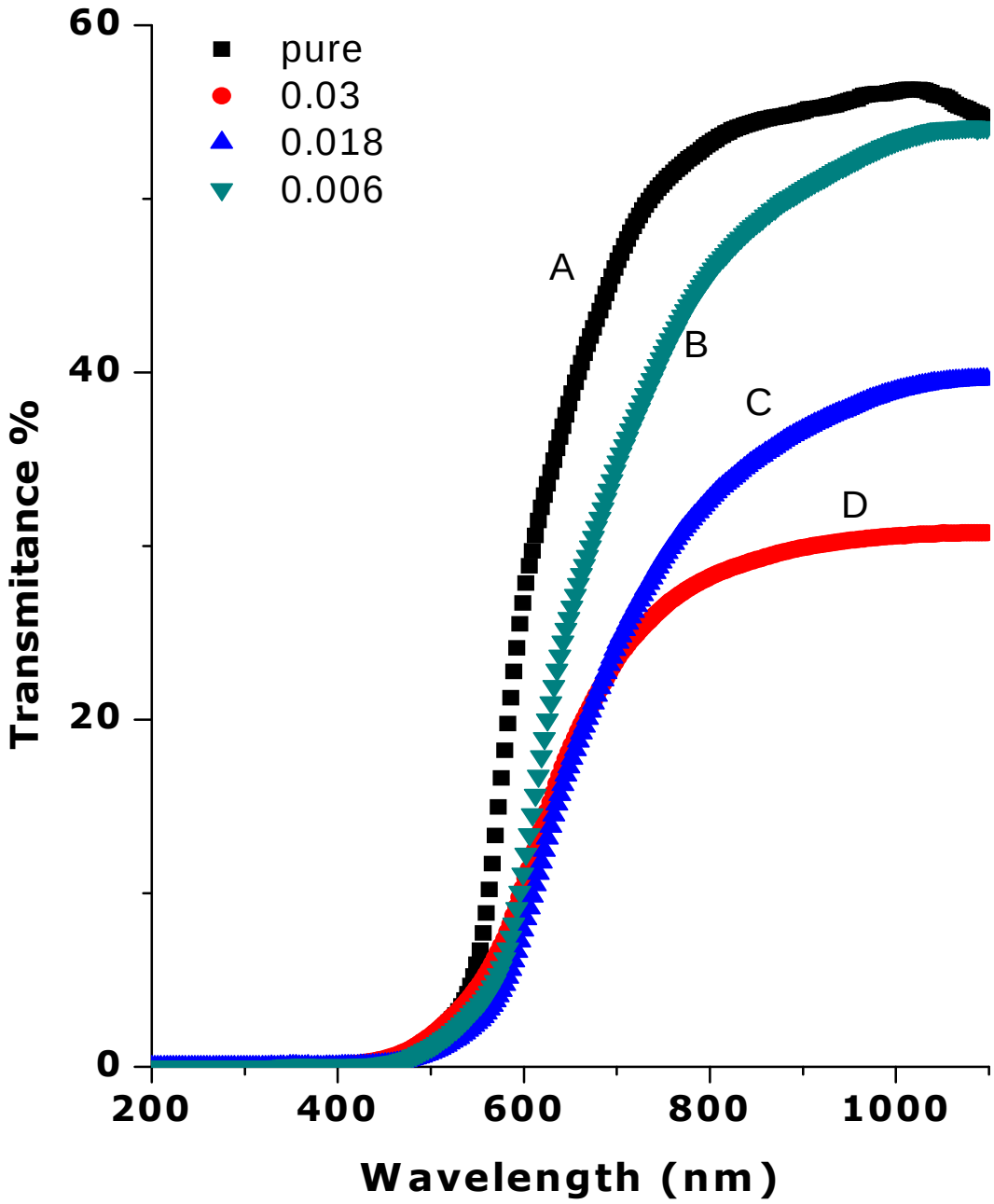

Figure 5.30 The UV-Visible transmission curves of Ru doped hematite samples grown on FTO glass substrate at 95°C for 24 h, where A is a undoped, B is 0.006g, C is 0.018g and D is 0.03g of $Ru.xCl_3$.

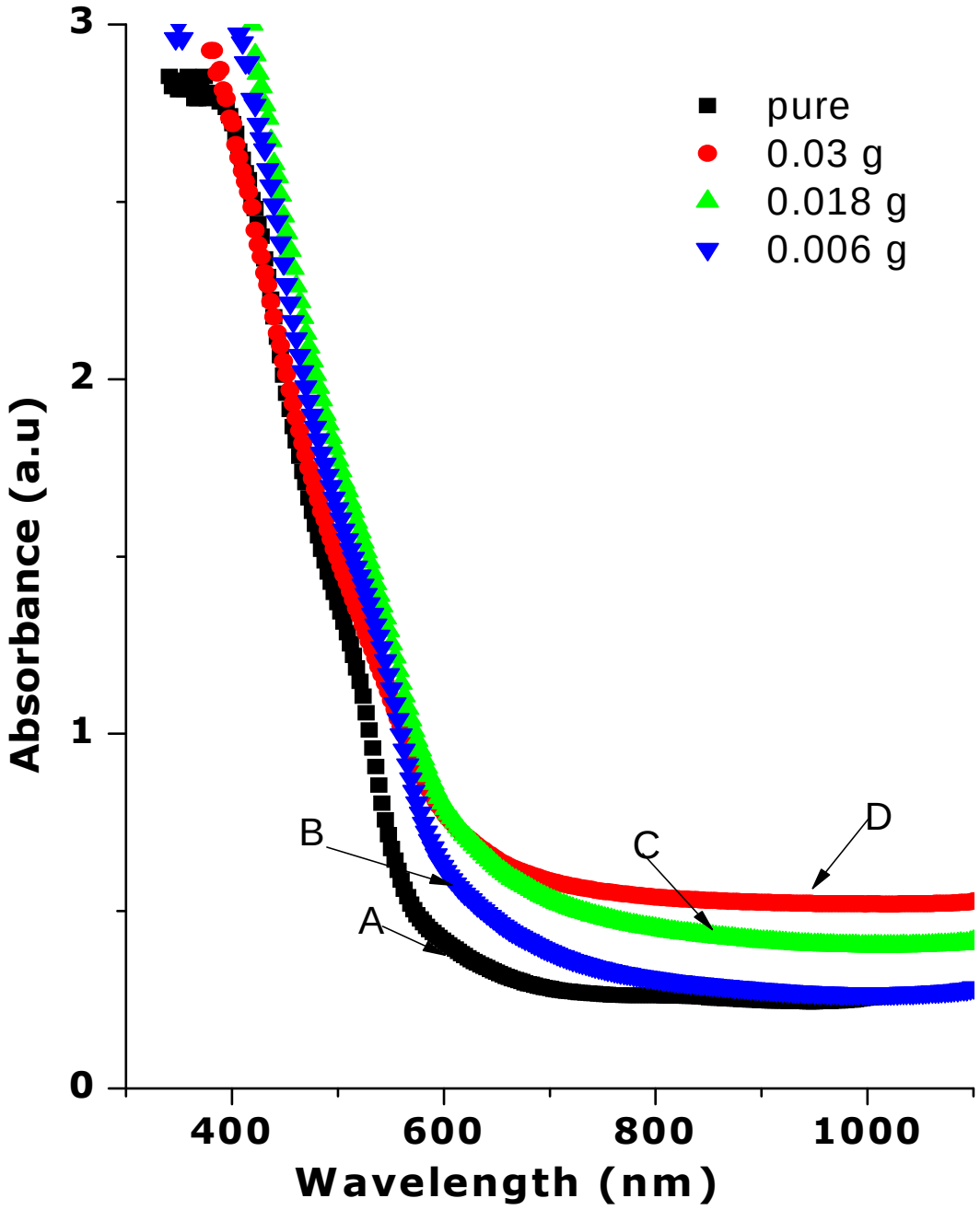

Figure 5.31 The UV-Visible absorption curves of Ru doped hematite nanorods grown on FTO glass substrate at 95^{o}C for 24 h, where A is a undoped, B is 0.006g, C is 0.018g and D is 0.03g of Ru.xCl_3.

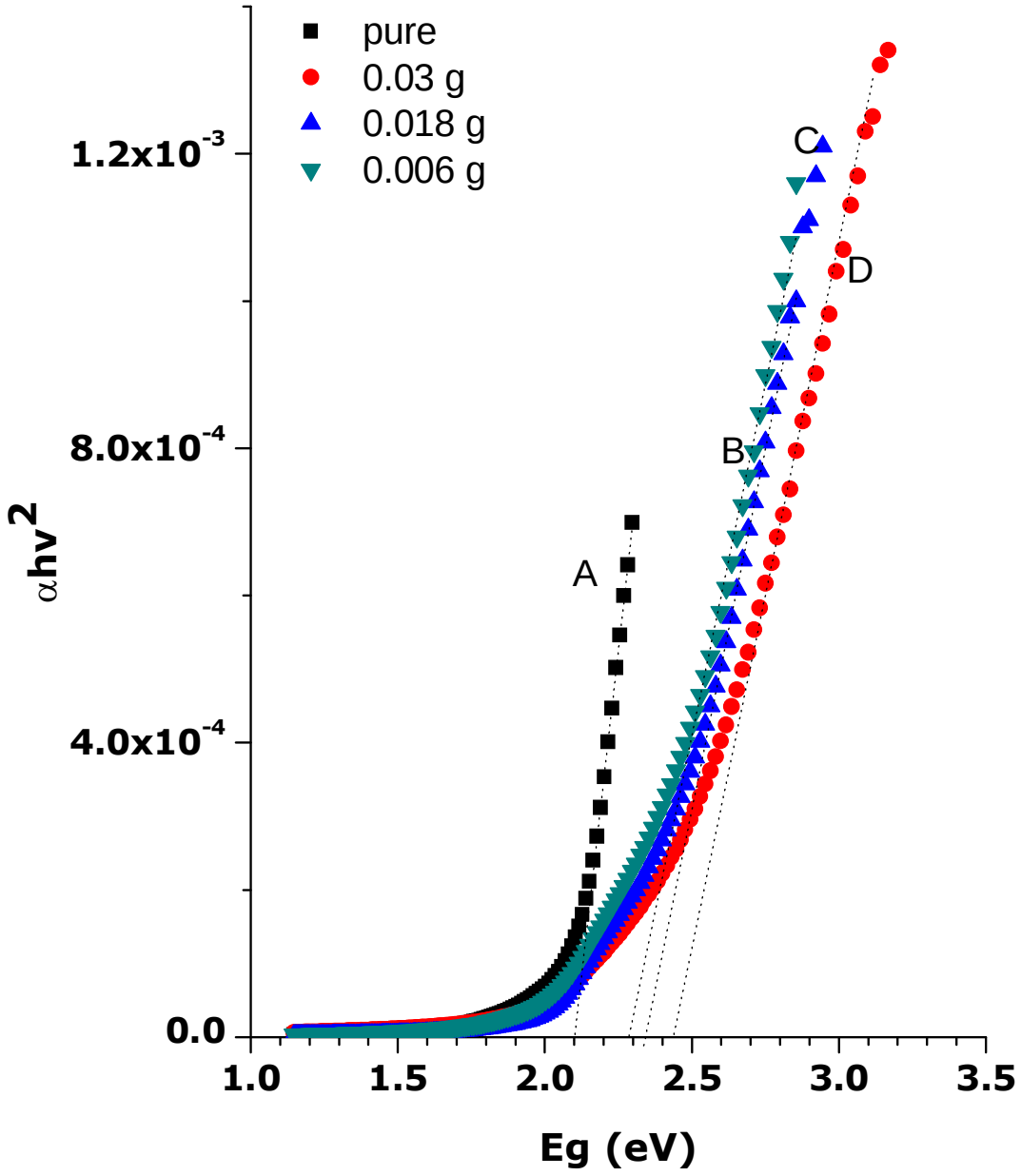

Figure 5.32 The band gap estimation deduced from a plots of $(\alpha h\upsilon)^2$ as a function of photon energy ($h\upsilon$) for a Ru doped hematite thin films grown on FTO glass substrate at 95°C for 24 h, where A is a undoped, B is 0.006g, C is 0.018g and D is 0.03g of $Ru.xCl_3$.

5.7. Applications

5.7.1. Hydrogen gas sensing on hematite nanorods

Hydrogen gas sensing on hematite samples was performed in a chamber with a gas inlet and outlet. The heating stage in the chamber was couple to the thermocouple, which was also coupled to the fluke multimeter that was also coupled to the computer. The gas sensing measurements were performed in the nitrogen gas environment.

It is well known that the fundamental sensing mechanism of semiconductor based gas sensors relies on a change in electrical conductivity due to the interactions between the surface complexes such as $O^{\bar{I}}$, $O_2^{\bar{I}}$, reactive chemical species ($OH^{\bar{I}}$), and gas molecules to be detected. In many gas sensors, the conductivity response is determined by the efficiency of catalytic reactions with detected gas participation, taking place at the surface of gas-sensing material. Therefore, control of catalytic activity of gas sensor material is one of the most commonly used means to enhance the performances of gas sensors. However, in practice, the widely used gas sensing metal oxide materials such as TiO_2, ZnO, SnO_2, Cu_2O, Ga_2O_3, Fe_2O_3, are the least active with catalytic point of view [156].

Figure 5.33 presents the hydrogen gas sensing graph of undoped hematite nanorods. The high resistive sample of pure hematite was heated at 300^{o}C. The hydrogen flow rate of 120 ppm was used. In our experiments, the oriented nanostructures are highly crystalline with a typical diameter of 30ï 100 nm, and a thickness of ~550 nm to 800 nm, so that they provide a high surface area and, in turn, provide sufficient ionize sub-surface oxygen adsorbed states [157,158]. The nanorods create a significant amount of surface acceptor states, leading to a high resistance in the normal state without H_2.

When hydrogen gas is allowed in to the chamber; the conductance of hematite nanostructures is enhanced due to the reaction of hydrogen with the material surface and is also due to the removal of chemisorbed oxygen from the nanostructure surface by H_2 [159,160]. The results on the gas sensing of the undoped give a response of 46 seconds and the recovery time of 166 seconds and a sensitivity of S=6%.

The sensitivity of iron oxide-based sensors have been enhanced by various doping schemes and a number of different dopants such as Pd , Sn, Ti, Zn etc (Kanai et al (1992)[161]; Neri et al (2002)[162]; Reddy et al (2002)[163]; Vasiliev (1992)[164]; Tan et al (2003)[165].

While doping is an important factor for controlling the sensing characteristics, the sensor structure, and especially the thickness of its active layer, also has a great influence on the sensitivity. In reality, bulk and thick-film type sensors display a relatively low sensitivity, which substantially improves when the same sensing material is used in a thin-film type of a sensor [166].

The hydrogen gas sensing results for the Ru dope hematite film is presented in Figure 5.34. Navale et al (2009) [167] reported Ru-ZNO is highly sensitive on Liquid Petroleum Gas (LPG) and hydrogen gas compare to undoped ZNO. The Ruthenium doped hematite samples displayed an improved response time of 24 seconds and recovery time of 11 seconds compared to the undoped films, which is very important in gas sensors. This system exhibit the sensitivity of S=10.2%.

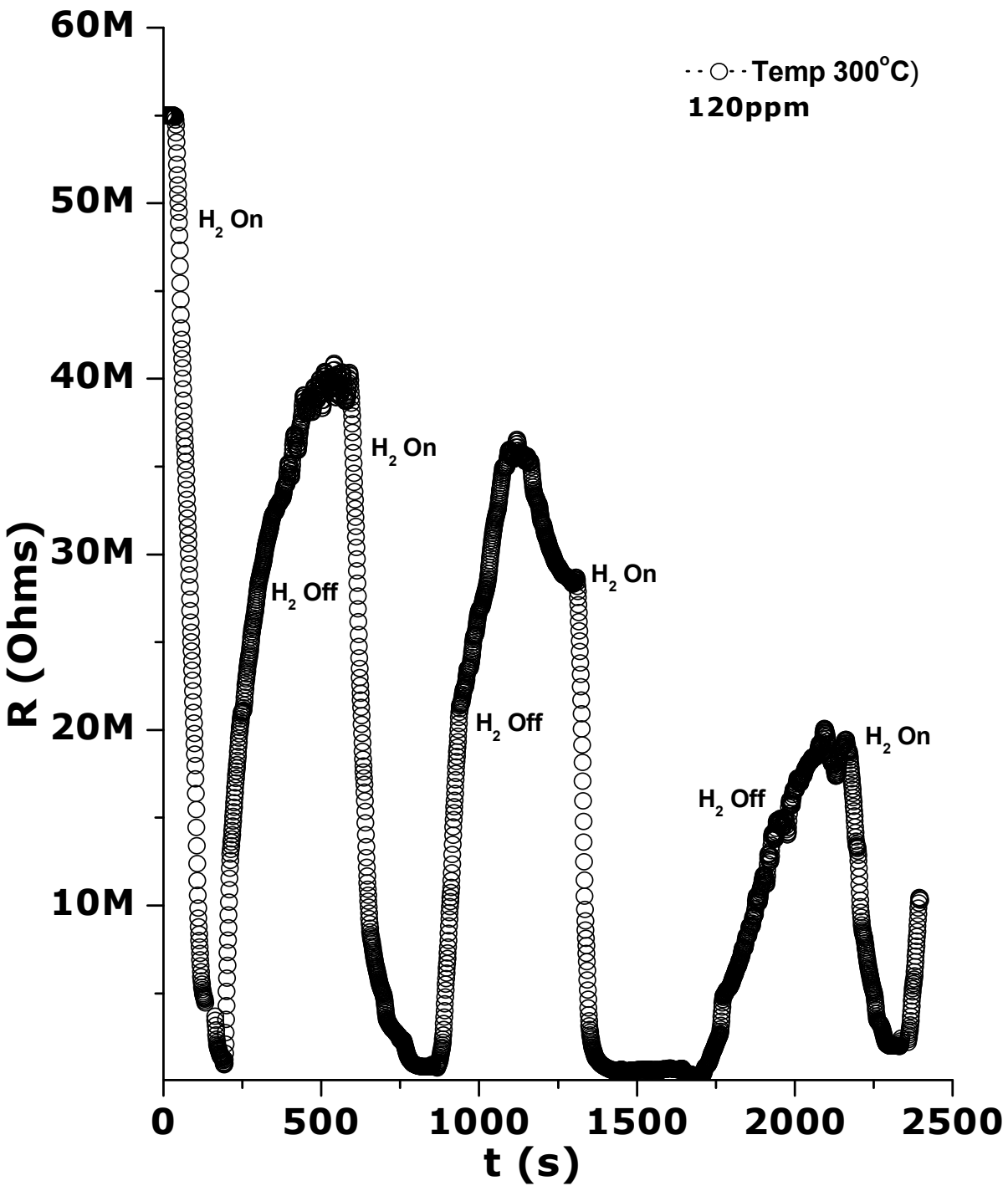

Figure 5.33 The graph of hydrogen gas sensing of undoped hematite sample grown on corning glass substrate at 95°C for 24 h.

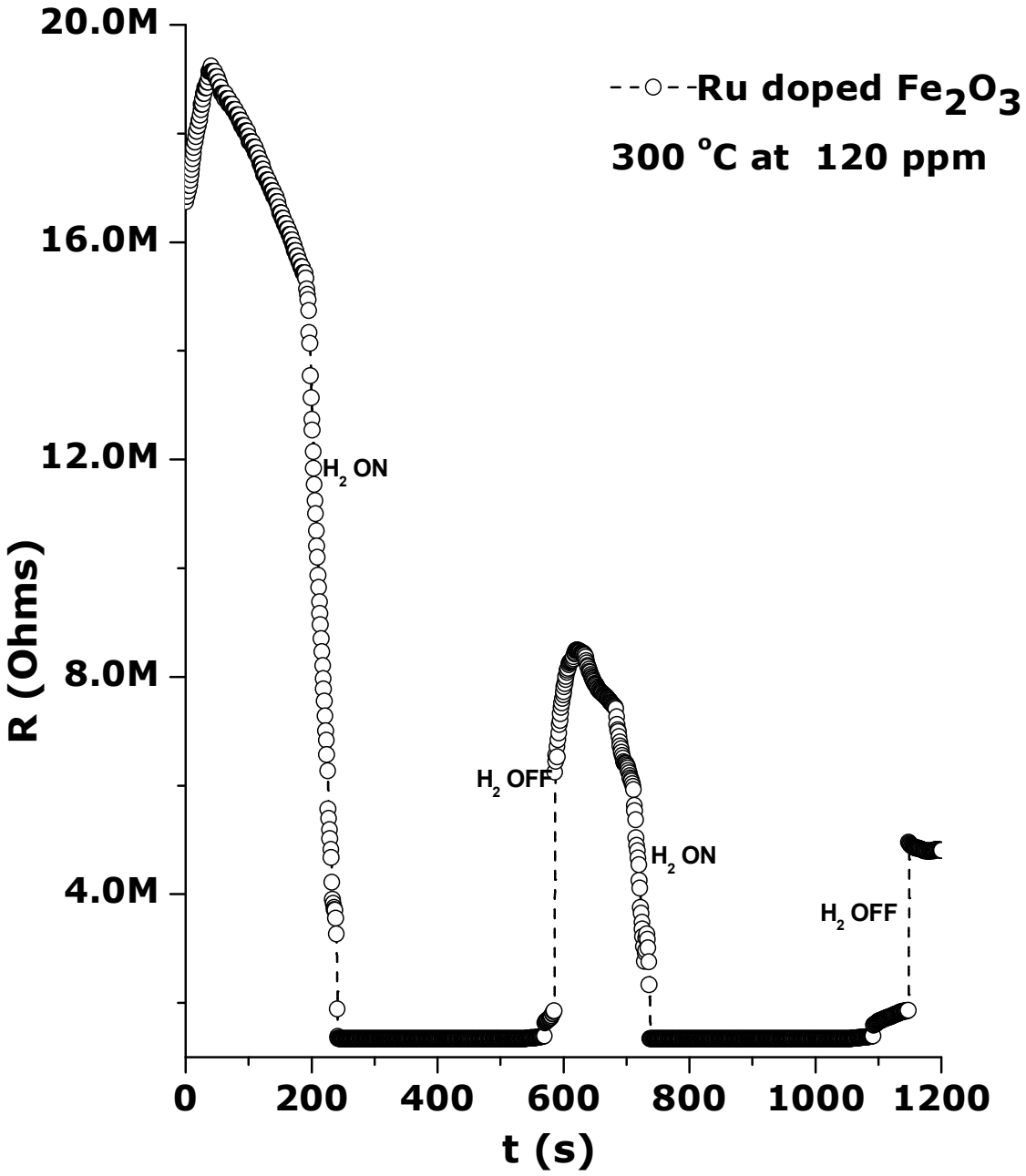

Figure 5.34 The graph of hydrogen gas sensing of Ru doped hematite sample grown on corning glass substrate at 95°C for 24 h. The doping was done with 0.03g of $RuCl_3xH_2O$ salt.

5.7.2. Electrochemistry on undoped and Ru doped hematite nanoparticles

Photocurrent was measured in a three-electrode configuration in 1 M NaOH solution, Ag/AgCl as the reference electrode, and platinum counter electrode. The bare FTO area of the hematite photoelectrode was used to make the electrical contact. The electrical contact with the α-Fe_2O_3 film was made with a crocodile clip and kept above the level of electrolyte solution. The electrode potential was controlled by a potentiostat (micro-Autolab, type III). The 25 mm^2 of the sample was exposed to the electrolyte at room temperature. Nitrogen gas was continuously bubbled in to the electrolyte to prevent oxygen from the external environment to enter in to the electrolyte. Figure 5.35 (a) to Figure 5.35 (d) present the forward and reverse reaction I-V curve of undoped and doped hematite films. The measurements were taken from -0.7 V to 0.7 V at a scan rate of 10 mV/s.

Our samples showed good photocurrent which may be due to the fact that the films were rough in nano form, which helps in trapping more photons due to inter-scattering across the grains in the photoactive layer. Sample A has two reduction peaks at (-0.29V and 0.56V), B has reversible oxidation peak around 0.159V that reverses at about 0V and this sample has a reduction peak at 0.497 V, C has a reduction peak that appear around 0.49V and the is a broad separation between the forward and the reverse reaction. D has a peak at 0.251V. In all the graphs there is no pronounced peaks that are from the oxidation of the photo electrode, this may be due to the fact that the samples are oxides so it only reduces water to form hydrogen. The Ru doped hematite samples show some improvement since there is a shift to the smaller values of voltages, which could mean practically that the splitting of water would require a small amount of bias voltage. This also could be due to the fact that the samples are very rough.

Souza et al (2009) [168] reported that the dark current is negligible up to about 0.6 V, where electrocatalytic oxygen evolution starts and also stated that the photocurrent obtained could not be distinguished from the dark current and Bora et al (2012) suggested that this might be due to very compact nature of the film or the film has less porosity which resists the electrolyte to see the nanograin. Our hematite thin films looked very shiny in the electrolyte when illuminated, which reflects most of the incident light and absorb very less amount. The same was observed by Bora et al (2012) [169] on the hematite samples obtained by spin coating.

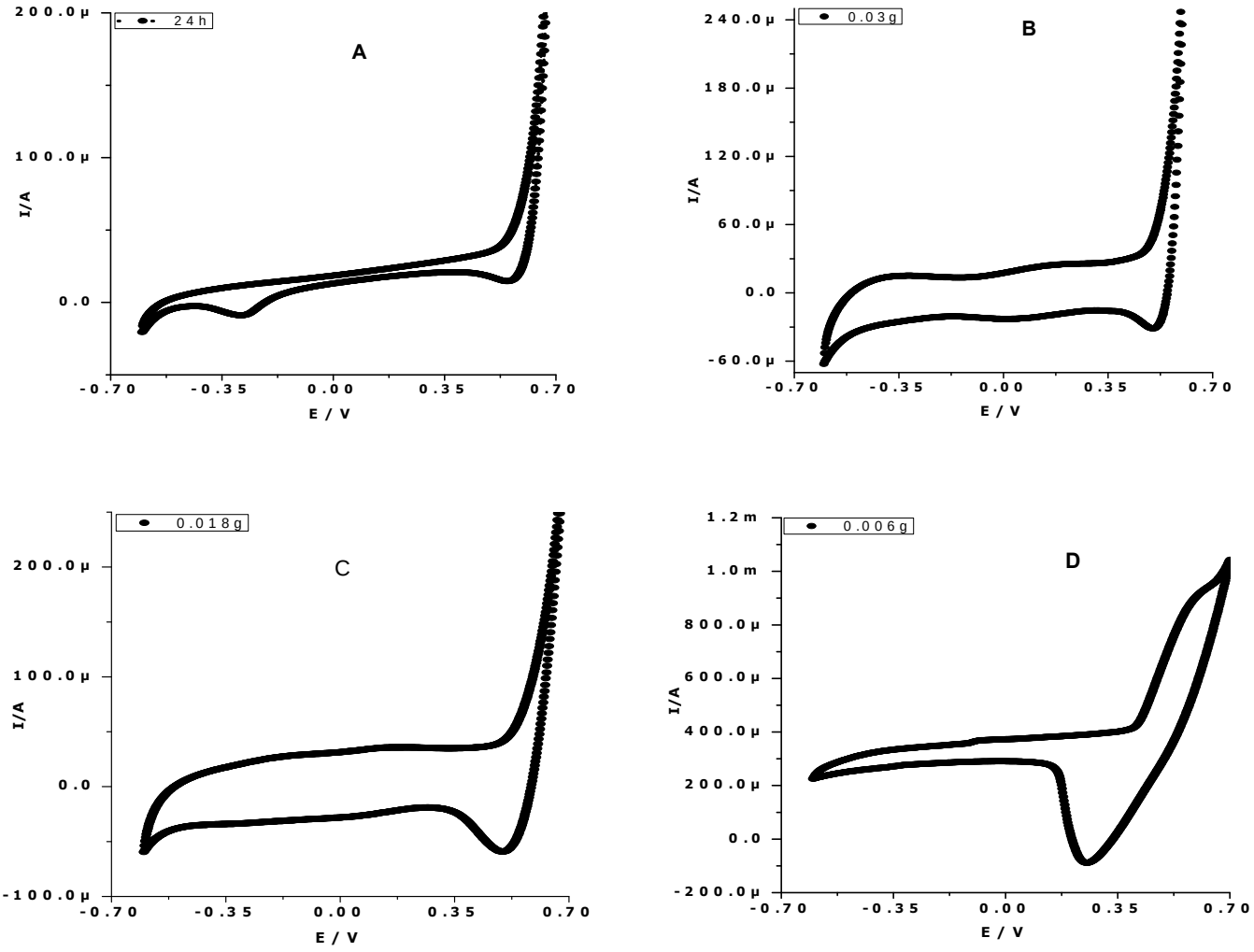

Figure 5.35 The cyclic voltammetry graphs of undoped and Ru doped hematite samples grown at 95^{o}C for 24 h. Therefore A is for the undoped sample, B is for (0.03g), C is for (0.018g) and D for (0.006g) of $RuCl_3xH_2O$. The measurements were done at 10 mV/s scan rate. The Ag/AgCl reference electrode and the platinum counter electrode in 1M of NaOH solution were used.

CHAPTER VI

6. CONCLUSIONS

The growth of hematite nanorods of various lengths and diameters were synthesized using ACG on FTO and other substrates such as silicon and corning glass substrate. SEM and TEM images confirmed that the grown nanostructures were indeed nanorods. The orientations and sizes of these nanorods depend on the solution pH. Perpendicular oriented nanorods with the diameters ranging between (20 and 60 nm) and lengths ranging between (500 and 800 nm) were grown at pH 1.5 as suggested by Vayssieres. The same orientations with shorter length and bigger diameters were obtained at pH 2 to pH 3. Therefore all experiments were performed at pH 1.5 to investigate the effect of Ru dopant on the structural morphology as well as on its sensing and electrochemical properties and the results were compared to the undoped hematite nanorods. The structure and the crystallinity of our samples were investigated using XRD. The XRD analysis suggested that the as-grown samples were of a polycrystalline hematite with a preferred orientation at the [104] plane. According to JCP2 CAT: (73-0603) these XRD pattern were of a rhombohedral structure with a space group of R-3c and the lattice parameters a=0.50356 nm, c=1.37489 nm and z = 6. And to investigate the amount of Ru on the doped samples was done using SEM equipped with EDX. Raman and FTIR spectroscopies were used to further analyze the samples and all confirmed that the grown nanostructures were of hematite material and were in good correlation with the published data. The ruthenium doped hematite samples exhibit the decrease in Raman intensities and the shift in the wavenumbers and some Raman modes vanished as the amount of dopant concentration was increasing. There were only four instead of five Eg modes. The mode at 660 cm^{-1} vanished as the dopant concentration was increasing. FTIR analysis of both the undoped and dope samples exhibit the Eu band which is for the stretching of the Fe-O and Fe-O-Fe bonds. Mossbauer analysis of undoped samples indicated that the sample grown for 4 h exhibits a doublet that may be due to the superparamagnetism of the nanoparticles. This would mean that our samples were a mixture of hematite (92.6%) and maghemite (7.4%). On the other hand, the spectra of the sample grown for 10 h and 24 h show a 6-line hyperfine pattern without a doublet. The magnetic field of 505.1 kOe with the isomer shift of 0.326 mm/s and the quadrupole splitting of -0.112 mm/s was obtained for the sample grown for 4 h. The sample grown for 10 h has the magnetic field of 507.9 kOe with the isomer shift of 0.325 mm/s

and the quadrupole splitting of -0.110 mm/s. The 24 h sample has also a magnetic field 459.1 kOe and the isomer shift and the quadrupole splitting of 0.300 and -0.108 mm/s, respectively. The 24h sample has a magnetic field that suggests that the sample is made of maghemite. These magnetic field values are slightly smaller than the magnetic field of the bulk hematite of 519 kOe. This might be due to the presence of the gamma phase iron oxide in the samples as indicated by the XRD results. And the doped unheated samples exhibit the doublets which indicate that the samples were super-paramagnetic while the heated Ru-hematite samples have sextet with the magnetic field collapsed to a bulk magnetic field and this was due to the fact that the samples were grown for 24 h and have bigger particles and this agrees to the undoped samples grown for 24 h which resembles a bulk signature on a Mössbauer analysis. The UV-Vis optical transmission of the samples grown for different pH values reveals that the pH was indeed controlling the band gap of the material. The estimated band gap for the randomly oriented hematite nanorods grown as a function of time and pH at the constant temperature exhibit a band gap ranging between 2.12 eV and 2.4 eV and these band gap values are in good agreement with the reported band gap of hematite depending on the synthesis procedure. The ruthenium doped hematite nanorods were also grown at the pH of 1.5 and different doping amount were achieved the most attractive amount of doping was found at 0.03g of ruthenium chloride and also the optical measurements on these samples were performed and the blue shift of about 0.3 to 0.56 eV was found on the samples doped with 0.03g of ruthenium chloride. This improvement on the band gap would means that this electrode is well suitable to drive water splitting. For the targeted applications we have look at the gas sensing and electrochemical properties of the deposited films of hematite. In terms of the response time and recovery time we observed an improvement on the doped sample compare to the undoped hematite samples. The Ru doped hematite samples show also some improvement in their electrochemical properties, which could mean practically that the water splitting with Ru doped hematite, would require a small amount of bias voltage.

REFERENCES

[1]. Momirlan, M. and Veziroglu, T. N. (2002) ôCurrent status of hydrogen energyö, *Renewable and Sustainable Energy Reviews,* Vol. 6, pp. 141ï 179

[2]. Midilli, A., Ay, M., Dincer, I., Rosen, M. A. (2005) ôOn hydrogen and hydrogen energy strategies: I: current status and needsö, *Renewable and Sustainable Energy Reviews,* Vol. 9, pp. 255ï 271

[3]. International Partnership for Hydrogen and fuel cell in the Economy (IPHE) Renewable Hydrogen Report of March, (2011), http://www.iphe.net/docs/Renew_H2_Introduction.

[4]. IEA Energy Technology Essentials, April, (2007), The IEA Energy Technology Essentials are regularly-updated briefs that draw together the best-available, consolidated information on energy technologies from the IEA network, ô*Hydrogen Production & Distribution*ö, http://www.iea.org

[5]. Archer D. M. and Nozik A. J. (2008) ôNanostructured and photoelectrochemical system for solar photon conversionö, Series on photoconversion of solar energy, *imperial college press, Vol. 3.*

[6]. Kudo, A., Omori, K., and Kato, H. (1999) ôA novel aqueous process for preparation of crystal form-controlled and highly crystalline $BiVO_4$ powder from layered vanadates at room temperature and its photocatalytic and photophysical propertiesö, *American. Chemical Society,* Vol. 121 No. 49, pp. 11459 -11467

[7]. Murphy, A. B., Barnes, P. R. F., Randeniya L. K., Plumb, I. C., Grey, I. E., Horne, M. D., and Glasscock, A. J. (2006) ôEfficiency of solar water-splitting using semiconductor electrodesö, *International Journal of Hydrogen Energy,* Vol. 31, pp. 1999-2017

[8]. Bolton, J. R., Stricklerô S. J., and Connolly, J. S. (1985) óLimiting and Realizable Efficiencies of Solar Photolysis of Waterô, *Nature,* Vol. 316, pp. 495-500

[9]. Sporar, D. (2007) *Sputter Deposition of Iron Oxide and Tin Oxide Based Films and the Fabrication of Metal Alloy Based Electrodes for Solar Hydrogen Production*. Unpublished MSc Thesis, University of Toledo, USA.

[10]. Morel, A., Gentili, B., Claustre, H., Babin, M., Bricaud, A., Ras, J., and Tieche, F. (2007) óOptical properties of the ñclearestò natural waterô, *Limnology and Oceanography,* Vol. 52 No.1, pp. 217ï 229

[11]. Wheeler, D. A., Wang, G., Ling, Y., Li, Y., and Zhang J. Z, (2012) óNanostructured hematite: synthesis, characterization, charge carrier dynamics, and photoelectrochemical propertiesô, *Energy Environmental Science,* Vol. 5, pp. 6682ï 6702

[12]. Sivula, K., Le Formal, F., and Grätzel, M. (2011) óSolar Water Splitting: Progress Using Hematite (Ŭ-Fe_2O_3) Photoelectrodesô, *ChemSusChem,* Vol. 4, pp. 432-449

[13]. Sivula, K., Zboril, R., Le Formal, F., Robert, R., Weidenkaff, A., Tucek, J., Frydrych, J., and Grätzel, M. (2010) óPhotoelectrochemical Water Splitting with Mesoporous Hematite Prepared by a Solution-Based Colloidal Approachô, *Journal of the American Chemical Society,* Vol. 132 No. 21, pp. 7436ï 7444

[14]. Desai, J. D., Pathan, H. M., Min, S. K, Jung, K. D., Joo, O. S. (2005) óFT-IR, XPS and PEC Characterization of Spray Deposited Hematite Thin Filmsô, *Applied Surface Science,* Vol. 252 No. 5, pp. 1870ï 1875

[15]. Matsumoto, Y. (1996) óEnergy positions of oxide semiconductors and photocatalysis with iron complex oxidesô, *Journal of Solid State Chemistry,* Vol. 126 No. 2, pp. 227-234

[16]. Vayssieres, L., Sathe, C., Butorin, S. M., Shuh, D. K., Nordgren, J., and Guo, J. (2005) ó1-D quantum confinement in Ü-Fe_2O_3 ultrafine nanorod arraysô, *Advanced Materials,* Vol. 17 No. 19, pp. 2320 ï 2323

[17]. Lin, Y., Yuan, G., Liu, R., Zhou, S., Sheehan, S. W., Wang, D. (2011) óSemiconductor nanostructure-based photoelectrochemical water splitting: A brief reviewô, *Chemical Physics Letters*, Vol. 507 No. 4-6, pp. 209ï 215

[18]. Glasscock, J. A., Barnes, P. R. F., Plumb, I. C., Bendavid, A., Martin, P. J. (2008) óStructural, optical, and electrical properties of undoped polycrystalline hematite thin films produced using filtered arc depositionô, *Thin Solid Films,* Vol. 516 No.8, pp. 1716-1724

[19]. Vayssieres L. (Eds.), (2006) ón Solar Hydrogen & Nanotechnologyô, *SPIE Proceedings*, Vol. 6340, pp 63400 I1-63400 I 12

[20]. Bolton, J. R. (1996) óSolar photoproduction of hydrogen: A reviewô, *Solar Energy,* Vol. 57 No. 1, pp. 37-50

[21]. Glasscock, J. A. (2008) *Nanostructured materials for photoelectrochemical hydrogen production using sunlight*. Unpublished PhD thesis, The University of New South Wales, Australia.

[22]. Shannon C. Riha, Michael J. DeVries Vermeer, Michael J. Pellin, Joseph T. Hupp, and Alex B. F. Martinson (2013) óHematite-based Photo-oxidation of Water Using Transparent Distributed Current Collectorsô, *ACS Applied Materials and Interfaces,* Vol. 5, pp. 360−367

[23]. Cornell, M. and Schwertmann, U. (2003) *The Iron Oxides, Structure, Properties, Reactions, Occurrence and Uses*, Wileyï VCH, Weinheim, Germany, pp. 664

[24]. Jolivet, J. P., Tronc, E., Chaneac, C. (2006) ôIron oxides: From molecular clusters to solid. A nice example of chemical versatilityö, *Comptes Rendus Geoscience,* Vol. 338, pp. 488-497

[25]. Jolivet, J. P. (2000) *Metal Oxide Chemistry and Synthesis: From Solution to Solid State,* John Wiley and Sons, Chichester, pp. 321

[26]. Matijevic, E. (1988) ôColloid science of ceramic powdersö, *Pure and Applied Chemistry,* Vol. 60, pp 1479-1491

[27]. Pulgarin, C., Kiwi, J. (1995) ôIron Oxide-Mediated Degradation, Photodegradation, and Biodegradation of Aminophenolsö, *Langmuir,* Vol. 11, pp. 519-526

[28]. Pelino, M., Colella, C., Cantallini, C., Faccio, M., Ferri, G., D'Amico, A. (1992) ôMicrostructure and electrical properties of an Ŭ-hematite ceramic humidity sensorö, *Sensors and Actuators B: Chemical,* Vol. 7 No.1-3, pp. 464-469

[29]. Wu, C., Yin, P., Zhu, X., OuYang C., Xie, Y. (2006) ôSynthesis of Hematite (Ŭ-Fe_2O_3) Nanorods: Diameter-Size and Shape Effects on Their Applications in Magnetism, Lithium Ion Battery, and Gas Sensorsö, *Journal of Physical Chemistry B,* Vol. 110, pp 17806-17812

[30]. Widder, K. J., Senyel, A., E.Scarpelli, D. G. (1978) ôMagnetic microspheres: a model system for site specific drug delivery in vivoö, *Proceedings of the Society for Experimental Biology and Medicine,* Vol. 58 No. 2, pp. 141-146

[31]. Garcon, G., Garry, S., Gosset, P., Zerimech, F., Martin, A., Hannothiaux, M., Shirali, P. (2007) ôBenzo(a)pyrene-coated onto Fe_2O_3 particles-induced lung tissue injury: role of free radicalsö, *Cancer Letters,* Vol. 167, pp. 7-15

[32]. Lawaczeck, R., Menzel, M., Pietsch, H. V. (2004) óSuperparamagnetic iron oxide particles: contrast media for magnetic resonance imagingô, *Applied Organometallic Chemistry,* Vol. 18, pp 506-513

[33]. Busch, M., Gruyters, M., Winter, H. (2006) óSpin polarization and structure of thin iron oxide layers prepared by oxidation of Fe (1 1 0)ô, *Surface Science,* Vol. 600 No 18, pp. 4166-4169

[34]. Walter, D. (2006) óCharacterization of synthetic hydrous hematite pigmentsô, *Thermochimica Acta,* Vol. 445, pp 195-199

[35]. Vayssieres, L. (Eds.), (2006) *In Solar Hydrogen and Nanotechnology*, SPIE Proceedings, Vol. 6340, pp. 63400 O 1- 63400 O 10

[36]. Rollmann, G., Rohrbach, A., Entel, P., and Hafner, J. (2004) óFirst-principles calculation of the structure and magnetic 210 phases of hematiteô, *Physical Review B,* Vol. 69, pp. 165107- 165119

[37]. Zboril, R., Mashlan, M., Petridis, D. (2002) óIron (III) Oxides from Thermal Processess Synthesis, Structural and Magnetic Properties, Mössbauer Spectroscopy Characterization, and Applicationsô, *Chemistry of Materials,* Vol. 14 No. 3, pp 969 ï 982

[38]. Iordanova, N., Dupuis, M., Rosso, K. M. (2005) óCharge transport in metal oxides: A theoretical study of hematite Ŭ-Fe_2O_3ô, *Journal of Chemical Physics,* Vol. 122, pp 144305- 144314

[39]. Beermann, N., Vayssieres, L., Lindquist, S.-E., and Hagfelt, A. (2000) óPhotoelectrochemical studies of oriented nanorod thin films of hematiteô, *Journal of the Electrochemical Society,* Vol. 147 No. 7, pp. 2456-2461

[40]. Townsend, T. K., Sabio, E. M., Browning, N. D. and Osterloh, F. E. (2011) "Photocatalytic water oxidation with suspended alpha-Fe_2O_3 particles-effects of nanoscaling", *Energy Environmental Science,* Vol. 4, pp. 4270–4275

[41]. Kennedy, J. H. and Frese, K. W. Jr. (1978) "Photooxidation of water at α-Fe_2O_3 electrodes", *Journal of the Electrochemical Society,* Vol. 125 No. 5, pp. 709-714

[42]. Tilley, S. D., Cornuz, M., Sivula, K. and Grätzel, M. (2010) "Light-induced water splitting with hematite: Improved nanostructure and iridium oxide catalysis", *Angewandte Chemie International Edition,* Vol. 49, pp. 6405–6408

[43]. Kokorin, A. I. et al (Eds.), (2003) *Photo-oxidation of water at hematite electrodes,* Chemical Physics of Nanostructured Semiconductors, VSP, Utrecht, The Netherlands.

[44]. Morin, F. (1954). "Electrical properties of α-Fe_2O_3", *Journal of Physical Review,* Vol. 93 No. 6, pp. 1195-1199

[45]. Gardner, R. F. G., Sweett, F. and Tanner, D. W. (1963) "The electrical properties of alpha ferric oxide-I. The impure oxide", *Journal of Physics and Chemisty of Solids,* Vol. 24, pp. 1183-1196

[46]. Launay, J. C. and Horowitz, G. (1982) "Crystal growth and photoelectrochemical study of Zr-doped α-Fe_2O_3 single crystal", *Journal of Crystal Growth,* Vol. 57 No. 1, pp. 118-124,

[47]. Le Formal, F. (2011) *On the Morphology and Interfaces of Nanostructured Hematite Photoanodes for Solar-Driven Water Splitting.* Unpublished PhD thesis, EPFL.

[48]. Khan, S. U. M., A-shahry, M. and Ingler, W. B. (2002) "Efficient Photochemical Water Splitting by a Chemically Modified n-TiO_2", *Science,* Vol. 297, pp. 2243-2245

[49]. Fujishima, A. and Honda, K. (1972) ôElectrochemical photolysis of water at a semiconductor electrodeö, *Nature,* Vol. 238, pp. 37-38

[50]. Ahn, K. S., Yan, Y. F., Lee, S. H., Deutsch, T., Turner, J., Tracy, C. E., Perkins, C. L. and Al-Jassim, M. (2007) ôPhotoelectrochemical properties of N-incorporated ZnO films deposited by reactive RF magnetron sputteringö, *Journal of the Electrochemical Society,* Vol. 154 No.9, pp. B 956-B 959

[51]. Wrighton, M. S. et al. (1976) ôPhotoassisted electrolysis of water by ultraviolet irradiation of an antimony doped stannic oxide electrodeö, *Journal of American Chemical Society,* Vol. 98, pp. 44-48

[52]. Ohnishi, T., Nakato, Y and Tsubumura, H. (1975) óQuantum yield of photolysis of water on titanium oxideö, *Physical Chemistry,* Vol. 79, pp. 523-525

[53]. Yang, B. and Luca, V. (2008) ôEnhanced long- wavelength transient photoresponsiveness of WO_3 induced by tellurium dopingö, *Chemistry Communication,* No. 37, pp. 4454-4456

[54]. Yu, Z. G., Pryor, C. E., Lau, W. H., Berding, M. A and MacQueen, D. B. (2005) óCore-shell nanorods for efficient photoelectrochemical hydrogen productionö, *Journal of Physical Chemistry B,* Vol. 109, pp. 22913-22919

[55]. Fondell, M., Jacobsson, J. T., Boman, M and Edvinsson, T. (2014) óOptical Quantum Confinement in Low Dimensional Hematiteö, *Journal of Material Chemistry A,* Vol. 2, pp. 3352-3363

[56]. Bora, D. K., Braun, A and Constable, E. C. (2013) ôIn rust we trust. Hematite ï the prospective inorganic backbone for artificial photosynthesisö, *Energy Environmental Science***,** Vol. 6, pp. 407-425

[57]. Samira, B., Chandrappa, K. G and Sharifah, B. A. H. (2013) óGeneration of Hematite Nanoparticles via Sol-Gel Methodô, *Research Journal of Chemical Science,* Vol. 3 No.7, pp. 62-68

[58]. Hu, Y. S., Kleiman-Shwarsctein, A., Forman, A. J., Hazen, D and Park, J. N. (2008) óPt-doped α-Fe_2O_3 thin films active for photoelectrochemical water splittingô, *Chemistry of Materials,* Vol. 20, pp. 3803-3805

[59]. Zhang, F., Yang, H., Xie, X., Li, L., Zhang, L., Yu, J., Zhao, H and Liu, B. (2009) óControlled synthesis and gas-sensing properties of hollow sea urchin-like α-Fe_2O_3 nanostructures and α-Fe_2O_3 nanocubesô, *Sensor and Actuators B,* Vol. 141, pp. 381ï389

[60]. Wu, C., Yin, P., Zhu, X., OuYang, C. and Xie, Y. (2006) óSynthesis of Hematite (Ŭ-Fe_2O_3) Nanorods: ¡Diameter-Size and Shape Effects on Their Applications in Magnetism, Lithium Ion Battery, and Gas Sensorsô, *Journal Physical Chemistry B,* Vol. 110, pp. 17806ï17812

[61]. Liao, P., Keith, J. A and Carter, E. A. (2012) õWater Oxidation on Pure and Doped Hematite (0001) Surfaces: Prediction of Co and Ni as Effective Dopants for Electrocatalysisô, *Journal of American Chemical Society,* Vol. 134, pp. 13296−13309

[62]. Komp, R. J. (1995) *Practical photovoltaics: electricity from solar cells,* 3rd ed., Ann Arbor, Michigan: Aatec Publications.

[63]. Grimes, C. A., Varghese, O. K. and Ranjan, S. (2008) *Light water hydrogen, the solar hydrogen generation of water photoelectrolysis,* New York: Springer Science and Business media, LLC 546.

[64]. Momirlan, M. and Veroglu, T. N. (2002) óCurrent status of hydrogen energyô, *Renewable and Sustainable Energy Reviews,* Vol. 6 No.1-2 pp. 141-179

[65]. Warren, S. C., Voïtchovsky, K., Dotan, H., Leroy, C. M., Cornuz, M., Stellacci, F., Hébert, C., Rothschild, A. and Grätzel, M. (2013) óIdentifying champion nanostructures for solar water-splittingô, *Nature Materials,* Vol. 12 No.9, pp. 842-849

[66]. Itoh, K and Bockris, J. O. M. (1984) óStacked thin-film photoelectrode using iron oxideô, *Journal of Applied Physics,* Vol. 56 No. 3, pp. 874-876

[67]. Vayssieres, L. (Eds.), (2006) *Solar Hydrogen & Nanotechnology*, SPIE Proceedings 6340, pp. 63400 N1- 63400 N12

[68]. Vayssieres, L., Rabenberg, L and Manthiram, A. (2002) óAqueous chemical route to ferromagnetic 3-D arrays of iron nanorodsô, *Nano letters,* Vol. 2 No. 12, pp 1393-1395

[69] Yang, Y., Ma, H. X., Zhuang, J and Wang, X. (2011) óMorphology controlled synthesis of hematite nanocrystals and their facet effects on gas-sensing propertiesô, *Inorganic Chemistry,* Vol. 50, pp. 10143ï 10151

[70] Ling, Y. C., Wang, G. M., Wheeler, D. A., Zhang, J. Z and Li, Y. (2011) óSn-Doped hematite nanostructures for photoelectrochemical water splittingô, *Nano Letters,* Vol. 11, pp. 2119ï 2125

[71] Mao, A., Shin, K., Kim, J. K., Wang, D. H., Han G. Y. and Park, J. H. (2011) óControlled synthesis of vertically aligned hematite on conducting substrate for photoelectrochemical cells: nanorods versus nanotubesô, *ACS Applied Materials and Interfaces,* Vol. 3, pp. 1852ï 1858

[72]. Wu, W., Xiao, X., Zhang, S., Zhou, J., Fan, L., Ren, F and Jiang, C. (2010) óLarge-scale and controlled synthesis of iron oxide magnetic short nanotubes: shape evolution, growth mechanism, and magnetic propertiesô, *Journal of Physical Chemistry C,* Vol. 114, pp. 16092ï 16103

[73]. Zhang, Z., Hossain M. F. and Takahashi, T. (2010) "Environmental selfassembled hematite (α-Fe_2O_3) nanotube arrays for photoelectrocatalytic degradation of azo dye under simulated solar light irradiation", *Applied Catalyst B,* Vol. 95, pp. 423–429

[74]. Wu, K., Zhang, S. and Xie, Y. (2008) "Hematite hollow spheres with a mesoporous shell: controlled synthesis and applications in gas sensor and lithium ion batteries", *Journal of Physical Chemistry C,* Vol. 112, pp. 11307–11313

[75]. Fan, H. M., You, G. J., Li, Y., Zheng, Z., Tan, H. R., Shen, Z. X., Tang, S. H. and Feng, Y. P. (2009) "Shape-controlled synthesis of single crystalline Fe_2O_3 hollow nanocrystals and their tunable optical properties", *Journal of Physical Chemistry C,* Vol. 113, pp. 9928–9935

[76]. Gardner, J. M., Kim, S., Searson, P. C. and Meyer, G. J. (2011) "Electrodeposition of Nanometer Sized Ferric Oxide Materials in Colloidal Templates for Conversion of Light to Chemical Energy", *Journal of Nanomaterials,* Article ID 737812, 8 pages.

[77]. Zeng, S., Tang, K., Li, T., Liang, Z., Wang, D., Wang, Y., Qi, Y. and Zhou, W. (2008) "Facile route for the fabrication of porous hematite nanoflowers: its synthesis, growth mechanism, application in the lithium ion battery, and magnetic and photocatalytic properties", *Journal Physical Chemistry C,* Vol. 112, pp 4836–4843

[78]. Ramchandra, S. K., Min-Seung, C., Kwi-Sub, Y., Tae-Sin, K. and Chan-Jin, P. (2011) "Catalytic characteristics of MnO_2 nanostructures for the O_2 reduction process", *Nanotechnology,* Vol. 22, pp. 395402

[79]. Zhenmin, L., Xiaoyong, L., Hong, W., Dan, M., Chaojian, X and Dan, W. (2009) "Direct hydrothermal synthesis of single-crystalline hematite nanorods assisted by 1,2-propanediamine", *Nanotechnology,* Vol. 20, 245603 (9pp) doi:10.1088/0957-4484/20/24/245603

[80]. Kim, H. J., Choi, K. I., Pan, A., Kim, I. D., Kim, H. R., Kim, K. M., Na, C. W., Cao G. and Lee, J. H. (2011) ó Template-free solvothermal synthesis of hollow hematite spheres and their applications in gas sensors and Li-ion batteriesô, *Journal of Material Chemistry,* Vol. 21, pp. 6549ï 6555

[81]. Li, J. Lai, X., Xing, C. and Wang, D. (2010) ó One-pot synthesis of porous hematite hollow microspheres and their application in water treatmentô, *Journal of Nanoscience and Nanotechnology,* Vol. 10, pp 7707ï 7710

[82] Armelao, L., Granozzi, G., Tondello, E., Colombo, P., Principi, G., Lottici, P. P. and Antonioli, G. (1995) ó Nanocrystalline α-Fe_2O_3 solï gel thin films: a microstructural studyô, *Journal of Non-Crystalline Solids,* Vol. 192ï 193, pp 435ï 438

[83]. Zhong, L. S., Hu, J. S., Liang, H. P., Cao, A. M., Song, W. G. and Wan, L. J. (2006) ó Self-assembled 3D flowerlike iron oxide nanostructures and their application in water treatmentô, *Advanced Materials,* Vol. 18 No.18, pp. 2426-2431

[84]. Vayssieres, L., Beermann, N., Lindquist, S. E. and Hagfeldt, A. (2001) ó Controlled aqueous chemical growth of oriented three-dimensional crystalline nanorod arrays: application to iron(III) oxidesô, *Chemistry Materials,* Vol. 13 No.2, pp 233ï 235

[85] Watanabe, A. and Kozuka, H. (2003) ó Photoanodic properties of solï gel derived Fe_2O_3 thin films containing dispersed gold and silver particlesô, *Journal Physical Chemistry B,* Vol. 107, pp. 12713ï 12720

[86]. Woo, K., Lee, H. J., Ahn, J. P. and Park, Y. S. (2003) ó Solï gel mediated synthesis of Fe_2O_3 nanorodsô, *Advanced Materials,* Vol. 15 No. 20, pp. 1761- 1764

[87]. Glasscock, J. A., Barnes, P. R. F., Plumb, I. C. and Savvides, N. (2007) ôEnhancement of photoelectrochemical hydrogen production from hematite thin films by the introduction of Ti and Siö, *Journal of Physical Chemistry C,* Vol. 111 No.44, pp. 16477ï 16488

[88]. Lin, Y., Zhou, S., Sheehan, S. W. and Wang, D. (2011) ôNanonet-based hematite heteronanostructures for efficient solar water splittingö, *Journal of American Chemical Society,* Vol. 133, pp. 2398ï 2401

[89]. Cesar, I., Sivula, K., Kay, A., Zboril, R. and Graetzel, M. (2009) ôInfluence of feature size, film thickness, and silicon doping on the performance of nanostructured hematite photoanodes for solar water splittingö, *Journal of Physical Chemistry C,* Vol. 113, pp. 772ï 782

[90]. Tilley, S. D., Cornuz, M., Sivula K. and Gratzel, M. (2010) ôLight-Induced water splitting with hematite: improved nanostructure and iridium oxide catalysisö, *Angewandte Chemie International Edition,* Vol. 49 No.36, pp 6405ï 6408

[91]. Kohli, S., McCurdy, P. R., Johnson, D. C., Das, J., Prieto, A. L., Rithner, C. D. and Fisher, E. R. (2010) ôTemplate-Assisted Chemical Vapor Deposited Spinel Ferrite Nanotubesö, *Journal of Physical Chemistry C,* Vol. 114, pp. 19557ï 19561

[92]. Bachmatiuk, A., Kalenczuk, R. J., Rummeli, M. H., Gemming, T. and Borwlak-Palen, E. (2008) ôPreparation of ultra-large-scale catalysts for catalytic vapour deposition of carbon nanotubesö, *Materials Science-Poland,* Vol. 26 No. 1, pp. 105-111

[93]. Li, Y., Xiang, J., Qian, F., Gradecak, S., Wu, Y., Yan, H., Yan, H., Blom D. A. and Lieber, C. M. (2006) ôDopant-free GaN/AlN/AlGaN radial nanowire heterostructures as high electron mobility transistorsö, *Nano Letters,* Vol. 6, pp 1468ï 1473

[94]. Wu, J. J., Lee, Y. L., Chiang, H. H. and Wong, D. K. P. (2006) "Growth and magnetic properties of oriented α-Fe_2O_3 nanorods", *Journal of Physical Chemistry B,* Vol. 110, pp. 18108–18111

[95]. Kay, A., Cesar, I. and Gratzel, M. (2006) "New benchmark for water photooxidation by nanostructured α-Fe_2O_3 films", *Journal of American Chemical Society,* Vol. 128, pp. 15714–15721

[96]. Hahn, N. T., Ye, H. C., Flaherty, D. W., Bard, A. J. and Mullins, C. B. (2010) "Reactive ballistic deposition of alpha-Fe_2O_3 thin films for photoelectrochemical water oxidation", *ACS Nano,* Vol. 4, pp. 1977–1986

[97]. Liang, Y., Wang, C. C., Kei, C. C., Hsueh, Y. C., Cho, W. H. and Perng, T. P. (2011) "Photocatalysis of Ag-loaded TiO_2 nanotube arrays formed by atomic layer deposition", *Journal Physical Chemistry C,* Vol. 115, pp. 9498–9502

[98]. Rao, P. M. and Zheng, X. (2009) "Rapid catalyst-free flame synthesis of dense, aligned α-Fe_2O_3 nanoflake and CuO nanoneedle arrays", *Nano Letter,* Vol. 9 No. 8, pp. 3001–3006

[99]. Dong, Z., Kashkarov, P., and Zhang, H., (2010) "Monte Carlo study for the growth of α-Fe_2O_3 nanowires synthesized by thermal oxidation of iron", *Nanoscale,* Vol. 2, pp. 524–528

[100]. Ingler, W. B. and Khan, S. U. M. (2005) "Photoresponse of spray pyrolytically synthesized copper-doped p-Fe_2O_3 thin film electrodes in water splitting", *International Journal of Hydrogen Energy,* Vol. 30, pp 821–827

[101]. Wang, H. L. and Turner, J. A. (2010) "Characterization of hematite thin films for photoelectrochemical water splitting in a dual photoelectrode device", *Journal of the Electrochemical Society,* Vol. 157, pp. F173–F178

[102]. Nasibulin, A. G., Rackauskas, S., Jiang, H., Tian, Y., Mudimela, P. R., Shandakov, S. D., Nasibulina, L. I., Sainio, J. and Kauppinen, E. I. (2009) "Simple and rapid synthesis of α-Fe_2O_3 nanowires under ambient conditions", *Nano Research,* Vol. 2, pp. 373–379

[103]. Pingali, K. C., Deng, S. and Rockstraw, D. A. (2009) "Synthesis of Nanowires by Spray Pyrolysis", *Hindawi Publishing Corporation Journal of Sensors,* Article ID 683280, 6 pages doi:10.1155/2009/683280.

[104]. Goyal, R. N., Kaur, D., Pandey, A. K. (2009) "Growth and characterization of iron oxide nanocrystalline thin films via low-cost ultrasonic spray pyrolysis", *Materials Chemistry and Physics,* Vol. 116, pp. 638–644

[105]. Mooney, J. B. and Radding, S. B. (1982) "Spray pyrolysis Processing", *Annual Review of Material Science,* Vol.12, pp. 81–101

[106]. Duret, A. and Gratzel, M. (2005) "Visible light-induced water oxidation on mesoscopic α-Fe_2O_3 films made by ultrasonic spray pyrolysis", *Journal of Physical Chemistry B,* Vol. 109, pp. 17184–17191

[107]. Wang, G. M., Ling, Y. C., Wheeler, D. A., George, K. E. N., Horsley, K., Heske, C., Zhang, J. Z. and Li, (2011) "Facile synthesis of highly photoactive α-Fe_2O_3-based films for water oxidation", *Nano Letters,* Vol. 11, pp. 3503–3509

[108]. Vayssieres, L., Keis, K., Lindquist, S., Hagfeldt, A. (2001) "Purpose-built anisotropic metal oxide material: 3D highly oriented microrod-array of ZnO", *Journal of Physical Chemistry B,* Vol. 105, pp. 3350 – 3352

[109]. Nalwa, H. S. (2004) ó*Encyclopedia of Nanoscience and Nanotechnology', American Scientific publishers,* Vol. 8, pp. 147-166

[110]. Vayssieres, L. (2004) ó On the design of advanced metal oxide nanomaterialsô, *International Journal of Nanotechnology,* Vol. 1-2, pp. 1-41

[111]. Vayssieres, L., Hagfeldt, A. and Lindquist S. E. (2000) ó Purpose-built metal oxide nanomaterials. The emergence of a new generation of smart materialsô, *Pure Applied Chemistry,* Vol. 72, No. 1/2, pp. 47-52

[112]. Ezema, F. I. And Osuji, R. U. (2007) ó Band gap shift and optical characterization of chemical bath deposition CdSSe thin films on annealingô, *Chalcogenide Letters,* Vol. 4 No. 6, pp. 69-75

[113]. Singh, J. et al (Eds.), (2006) *Optical Properties of Condensed Matter and Applications,* John Wiley& Sons, Ltd.

[114]. Goodnew, P. J., Humphreys, J. and Branland, R. (2001) *Scanning Electron Microscopy and analyses,* 3rd ed., Teylor and Frecis Group, pp. 122-166.

[115]. Johansson, S. A. E., Campbell, J. L. and K. G. Malmqvist, (1995) *Particle Induced X-ray Emission Spectrometry*, Wiley, New York.

[116]. Callister, W. D. (2003) *Materials science and engineering and introduction,* 6th ed., John Wiley & Sons, Inc., Department of Metallurgical engineering, University of Utah.

[117]. Askeland, D. R. (1994) *The science and engineering of materials*, Alternate edition, PWS-KENT publishing company, University of Missouri-Rolla.

[118]. Fultz, B. and Howe, J. (2008) *Transmission Electron Microscopy and Diffractometry of Materials*, 3rd ed., Springer Berlin Heidelberg.

[119]. Marburger, W. G. and Hoffman, C. W. (1958) *Physics for our times,* New York: McGraw-Hill Book company.

[120]. Yang, X., Zhang, X., Liu, Z., Ma, Y., Huang, Y. and Chen, Y. (2008) "High-efficiency loading and controlled release of doxorubicin hydrochloride on graphene oxide", *Journal of Physical Chemistry C,* Vol. 112, pp. 17554– 17558

[121]. Dresselhaus, M. S., Dresselhaus, G., Saito, R., Jorio, A., (2005) "Raman spectroscopy of carbon nanotubes", *Physics Report,* Vol. 409, pp. 47-99,

[122]. Thibeau, R. J., Brown, C. W. and Heidersbach, R. H. (1978) "Raman spectra of possible corrosion products of iron", *Applied Spectroscopy,* Vol. 32, No. 6, pp. 532-535

[123]. de Faria, D. L. A., Silva, S. V., de Oliveira, M. T. (1997) "Raman microspectroscopy of some iron oxides and oxyhydroxides", *Journal of Raman Spectroscopy*, Vol. 28, pp. 873– 878

[124]. Balasubramaniam, R., Ramesh Kumar A. V., and Dillmann, P. (2003) "Phosphoric irons for concrete reinforcement applications", *Current Science,* Vol. 85, pp. 1546- 1555

[125]. Dyar, M. D. (2012) "Mössbauer Spectroscopy", Department of Astronomy, Mount HolyokeCollege,[online]http://serc.carleton.edu/research_education/geochemsheets/techniques/mossbauer.html (accessed 24 July 2012)

[126]. Varghese, O. K., Gong, D. W., Paulose, M., Ong, K. G., and Grimes, C. A. (2003) "Hydrogen sensing using titania nanotubes", *Sensors Actuators B,* Vol. 93, pp. 338-344

[127]. Elizabeth, P. (1992) ó*Nanotechnology yields transparent magnet-tiny iron oxide particles become more transparent than in bulk form– brief article', Science News* (accessed 11 July 1992)

[128]. Wang, J., White, W. B., Adair, J. H. (2005) óOptical properties of hydrothermally synthesized hematite particulate pigmentsô, *Journal of American Ceramic Society,* Vol. 88, pp. 3449ï 3454

[129]. Tahir, A. A., Upul Wijayantha, K. G., Saremi-Yarahmadi, S., Mazhar, M. and McKee, V. (2009) óNanostructured γ-Fe_2O_3 Thin Films for Photoelectrochemical Hydrogen Generationô, *Chemistry of Materials,* Vol. 21, pp. 3763ï 3772

[130]. Guo, J. (2007) óHematite nanoarrays promise water photo-oxidation by solar irradiationô, *SPIE Newsroom*, DOI: 10.1117/2.1200708.0827

[131]. Lifshitz, I. M. and Slyozov, V. V. (1961) óThe kinetics of precipitation from supersaturated solid solutionsô, *Journal of Physical Chemistry of Solids,* Vol. 19, pp. 35-50

[132]. Wagner, C. (1961) óTheory of Precipitate Change by Redissolution (Ostwald Ripening)ô, *Z. Elektrochem,* Vol. 65, pp. 581- 591

[133]. León, C. P., Kador, L., Zhang, M., Müller, A. H. E. (2004) óIn situ laser-induced formation of Ŭ-Fe_2O_3 from Fe^{3+} ions in a cylindrical core-shell polymer brushô, *Journal of Raman Spectroscopy,* Vol. 35, pp. 165ï 169

[134]. Saremi-Yarahmadi, S., Wijayantha, K. G. U., Tahir, A. A. and Vaidhyanathan, B. (2009) óNanostructured α-Fe_2O_3 electrodes for solar driven water splitting: effect of doping agents on preparation and performanceô, *Journal of Physical Chemistry C,* Vol. 113, pp.4768ï 4778

[135]. Bersani, D., Lottici, P. P. and Montenero, A. (1999) ôMicro-Raman investigation of iron oxide films and micro-powders produced by sol-gel syntheses*ö*, *Journal of Raman Spectroscopy,* Vol. 30, 355ï 360

[136]. Sartoretti, C. J., Alexer, B. D., Solarska, R., Rutkowska, I. A., Augustynski, J. and Cerny, R. (2005) ôPhotoelectrochemical oxidation of water at transparent ferric oxide film electrodes*ö*, *Journal of Physical Chemistry B,* Vol. 109 No. 28, pp.13685-13692

[137]. Beattie, I. R. and Gilson, T. R. (1970) 'The single-crystal Raman spectra of nearly opaque materials. Iron (III) oxide and chromium oxide*ö*, *Journal of the Chemistry Society A,* Vol.5, pp 980ï 986

[138]. Massey, M. J., Baier, U., Merlin, R. and Weber, W. H. (1990) ôEffects of pressure and isotopic substitution on the Raman spectrum of a-Fe_2O_3: identification of two-magnon scattering*ö*, *Physical Review B: Condensed Matter,* Vol. 41, pp. 7822ï 7827

[139]. Shim, S. H. and Duffy, T. S. (2001) ôRaman spectroscopy of Fe_2O_3 to 62 GPa*ö*, *American Mineralogist,* Vol. 87, pp. 318ï 326

[140]. Martin, T. P., Merlin, R., Huffman, D. R. and Cardona, M. (1977) ôResonant two-magnon Raman scattering in α-Fe_2O_3*ö*, *Solid State Communications,* Vol. 22. pp. 565-567

[141]. McCarty, K. F. (1988) ôA Raman study of the systems $Fe_{3-x}Cr_xO_4$ and $Fe_{2-x}Cr_xO_3$*ö*, *Solid State Communications,* Vol. 68, pp. 799-802

[142]. Sahoo, S. K., Agarwal, K., Singh, A. K., Polke, B. G. and Raha, K. C. (2010) ôCharacterization of gamma- and alpha-Fe_2O_3 nanopowders synthesized by emulsion precipitation-calcination route and rheological behaviour of alpha-Fe_2O_3*ö*, *International Journal of engineering, Science and Technology,* Vol. 2 No. 8, pp. 118-126

[143]. Zhao, B., Wang, Y., Guo, H., Wang, J., He, Y., Jiao, Z. and Wu, M. (2007) ‘Iron oxide (III) nanoparticles fabricated by electron beam irradiation method’, *Materials Science Poland,* Vol. 25 No. 4, pp. 1143-1148

[144]. Vempati, R. K., Loeppert, R. H., Sittertz-Bhatkar, H. and Burghardt, R. C. (1990) ‘Infrared Vibrations of Hematite Formed From Aqueous- and Dry-Thermal Incubation of Si-Containing Ferrihydrite’, *Clays and Clay Minerals,* Vol. 38, No. 3, pp. 294-298

[145]. Sidhu, P. S. (1988) ‘Transformation of trace-element substituted maghemite to hematite’, *Clays and Clay Minerals,* Vol. 36 No.1, pp. 31-38

[146]. Fischer, W. R. and Schwertmann, U. (1975) ‘The formation of hematite from amorphous iron (III) hydroxides’, *Clays and Clay Minerals*, Vol. 23 No.1, pp. 33-37

[147]. Rendon, J. L. and Serna, C. J. (1981) ‘IR spectra of powder hematite: Effect of particle size and shape’, *Clay Minerals*, Vol. 16, pp. 375-381

[148]. Serna, C. J., Ocana, M., and Iglesias, J. E. (1987) ‘Optical properties of α-Fe_20_3 microcrystals in the infrared’, *Journal of Physics C: Solid State Physics,* Vol. 20, pp. 473-484

[149]. Kim, J. G., Han, K. H., Lee, C. H., Jeong, J. Y. and Shin, K. H. (2001) ‘Crystallographic and Magnetic Properties of Nanostructured Hematite Synthesized by the Sol-Gel Process’, *Journal of the Korean Physical Society,* Vol. 38 No. 6, pp. 798-802

[150]. Pottier, A., Cassaignon, S., Chane´ac, C., Villain, F., Tronc E. and Jolivet, J. P. (2003) ‘Size tailoring of TiO2 anatase nanoparticles in aqueous medium and synthesis of nanocomposites. Characterization by Raman spectroscopy’, *Journal of Material Chemistry,* Vol. 13, pp. 877ï 882

[151]. Akl, A. A. (2004) óOptical properties of crystalline and non-crystalline iron oxide thin films deposited by spray pyrolysisô, *Applied Surface Science,* Vol. 233 No. 1-4, pp. 307ï 319

[152]. Ozer, N., Tepehan, F. and Tepehan, G. (1997) óPreperation and Optical Properties of Sol-Gel Deposited Electrochromic Iron Oxide Filmsô, *Proceedings SPIE,* Vol. 3138, pp. 31-39

[153]. Vayssieres, L. (2003) óGrowth of arrayed nanorods and nanowires of ZnO from aqueous solutionsô, *Advanced Materials,* Vol. 15, pp. 464 ï 466

[154]. Jo, H. C., Kim, K. M., Cheong, H., Lee S. H. and Debb, S. K. (2005) óIn Situ Raman Spectroscopy of RuO_2ÃxH$_2$Oô, *Electrochemical and Solid-State Letters,* Vol. 8 No. 4, pp. E39-E41

[155]. Helgason, Ö., Ayub, I., Berry, F.and Crabb, E. (2002) óPhase transitions of Ru doped iron oxide studied by ^{57}Fe Mössbauer spectroscopic at elevated temperatureô, *Hyperfine Interactions,* Vol. 141/142: pp. 291-295

[156]. Korotcenkov, G. (2007) óMetal Oxides for Solid-State Gas Sensors: What Determines Our Choice?ô, *Materials Science and Engineering B,* Vol. 139, pp. 1-23

[157]. Vanheusden, K., Warren, W. L., Seager, C. H., Tallant, D. R., Voigt, J. A. and Gnade, B. E. (1996) óMechanisms behind green photoluminescence in ZnO phosphor powdersô, *Journal of Applied Physics,* Vol. 79, 7983ï 7990

[158]. Chen, Z. G., Ni, A., Li, F., Cong, H. T., Cheng, H. M. and Lu, G. Q. (2007) óSynthesis and photoluminescence of tetrapod ZnO nanostructuresô, *Chemical Physics Letters,* Vol. 434, pp. 301ï 305

[159]. Barsan, N., Koziej, D. and Weimar, U. (2007) óMetal oxide-based gas sensor research: How to?ô, *Sensors and Actuators B,* Vol. 121, pp. 18ï35

[160]. Walton, R. M., Dwyer, D. J., Schwank J. W. and Gland, J. L. (1998) óGas Sensing Based on Surface Oxidation/Reduction of Thin Discontinuous Platinum-Titanium Films, Part 1. Activation and Characterizationô, *Applied Surface Science,* Vol. 124, pp. 187ï98

[161]. Kanai, H., Mizutani, H., Tanaka, T., Funabiki, T., Yoshida, S. and Takano, M. (1992) óX-Ray absorption study on the local structures of fine particles of Ŭ-Fe_2O_3ï SnO_2 gas sensorsô, *Journal of Materials Chemistry,* Vol. 2 No.7, pp. 703-707

[162]. Neri, G., Bonavita, A., Galvagno, S., Siciliano, P. and S. Capone, (2002) óCO and NO_2 sensing properties of doped-Fe_2O_3 thin films prepared by LPDô, *Sensor and Actuators B: Chemical,* Vol. 82 No. 1, pp. 40-47

[163]. Reddy, C. V. G., Cao, W., Tan, O. K. and Zhu, W. (2002) óPreparation of $Fe_2O_{3(0.9)}$ï $SnO2_{(0.1)}$ by hydrazine method: application as an alcohol sensorô, *Sensor Actuators B:Chemical,* Vol. 81 No. 2-3, pp. 170-175

[164]. Vasiliev, A. A. and Polykarpov, M. A. (1992) óChange of ferric oxide (Fe_2O_3) semiconductor conductivity type in the interaction with reducing gasesô, *Sensor and Actuators B:Chemical,* Vol. 7 No. 1-3, pp. 626-629

[165]. Tan, O. K., Cao, W., Zhu, W., Chai, J. W. and Pan, J. S. (2003) óEthanol Sensors Based on Nano-Sized α-Fe_2O_3 with SnO_2, ZrO_2, TiO_2 Solid Solutionsô, *Sensor and Actuators B: Chemical,* Vol. 93 No.1-3, pp. 396-401

[166]. Mohapatra, M. and Anand, S. (2010) óSynthesis and applications of nano-structured iron oxides/hydroxides ï a reviewô, *International Journal of Engineering Science and Technology,* Vol. 2 No. 8, pp. 127-146

[167]. Navale, S. C., Ravi, V. and Mulla, I. S. (2009) ‘Investigations on Ru doped ZnO: Strain calculations and gas sensing study’, *Sensors and Actuators B*, Vol. 139, pp. 466–470

[168]. Souza, F. L., Lopes, K. P., Longo E. and Leite, E. R. (2009) ‘The influence of the film thickness of nanostructured alpha-Fe_2O_3 on water photooxidation’, *Physical Chemistry Chemical Physics,* Vol. 11 No.8, pp. 1215–1219

[169]. Bora, D. K. (2012) *Hematite and its Hybrid Nanostructures for Photoelectrochemical Water Splitting: How Do Properties Affect Functionality?* Unpublished PhD Thesis, University of Basel, Switzerland